5-1-2018

Biomineralization and bioinspired synthesis of ceria and transition metal-oxide solid solution nanocrystals

Christopher David Curran
Lehigh University, cdcurran90@yahoo.com

Biomineralization and bioinspired synthesis of ceria and transition metal-oxide solid solution nanocrystals

by

Christopher Curran

Presented to the Graduate and Research Committee

of Lehigh University

in Candidacy for the Degree of

Doctor of Philosophy

in

Chemical Engineering

Lehigh University

May 2018

Dissertation is accepted and approved in partial fulfillment of the requirements for the Doctor of Philosophy in Chemical Engineering.

_____

Date

_____

Dissertation Director

_____

Accepted Date

Committee Members:

_____

Steven McIntosh

_____

Bryan Berger

_____

Christopher Kiely

_____

Mark Snyder

_____

Nicholas Strandwitz

Acknowledgements

This dissertation work would not have been possible without the help and support of my advisors Bryan Berger and Steve McIntosh. Their wisdom, support and encouragement were vital in my journey towards completion of my PhD. I also wish to thank my committee members Mark Snyder, Nick Strandwitz and especially Chris Kiely for all their helpful guidance.

In addition to all those who helped me academically, I must also thank those friends who have helped me to maintain my sanity. My lab mates Zhou Yang, Leah Spangler, Li Lu, Hamid Sadeghnejad, Caterina Sarno, John Sakizadeh, and office mate Evan Koufus were often my first choice for sharing a laugh or venting frustration. In addition, the HRH/EPI/D110 lunch group provided a much-needed break to often stressful days/nights in Iacocca Hall. Also without Wed/Fri pick-up soccer and Thursday night bar trivia with DJ Teez, the week would have gone by much slower. A special thanks goes out to all those who joined me on trivia team "Chris' Cool Crew".

Most importantly I must thank my family, without whom I would not be who I am today. My mother, who always nudged me towards making good choices and pushed me to reach academically even when it didn't seem like I had it in me. My father, who taught me how to work hard and how to put up with a difficult supervisor. My sister, who is achieving so much that I've had to work extra hard to keep up (at least I'll have a year where I'm the only Dr. Curran in the family). My brother, who has blazed the trail for both my sister and me, and who has a wonderful family in Kelsey and my beautiful niece Rory. You have all shaped my life in such positive ways, and for that I am truly thankful.

Table of Contents

List of Tables

Table of Figures

Abstract

Biomineralization is an intriguing approach to the synthesis of functional inorganic materials for energy applications whereby biological systems are engineered to mineralize inorganic materials and control their structure over multiple length scales under mild reaction conditions. Herein we demonstrate a single enzyme mediated biomineralization route to synthesize crystalline, catalytically active, quantum confined ceria (CeO_{2-x}) and ceria-zirconia ($Ce_{1-y}Zr_yO_{2-x}$) nanocrystals and a bio-inspired ligand mediated method for the synthesis of copper doped ceria ($Ce_{1-y}Cu_yO_{2-x}$) and gallium oxide. In contrast to typical synthesis routes, the crystalline oxide nanoparticles are formed at room temperature from an otherwise inert aqueous solution. An engineered form of silicatein, rCeSi, as a single enzyme not only catalyzes the direct biomineralization of the nanocrystalline oxides, but also serves as a templating agent to control their morphological structure. The biomineralized nanocrystals of less than 3 nm in diameter are catalytically active towards carbon monoxide oxidation following an oxidative annealing step to remove carbonaceous residue. The introduction of zirconia into the nanocrystals leads to an increase in Ce(III) concentration, associated catalytic activity, and the thermal stability of the nanocrystals.

Our ligand mediated synthesis of crystalline oxide is enabled through ligand exchange prior to pH adjustment to prevent the precipitation of the hydroxide phase. By producing particles at room temperature, dopant exsolution and particle growth by sintering can be minimized and/or controlled. Using our methodology, copper dopant concentrations of up to 35 mol % could be produced in 1.7 nm diameter ceria nanocrystals. The resulting materials showed high catalytic activity towards both the water gas shift reaction (WGS) and CO oxidation, with improved performance following the trend of increasing copper

content. In comparison to pure ceria nanocrystals, the WGS activation energy decreased from 89.0 to 49.2 kJ mol^{-1} and the CO oxidation light-off temperature decreased from 262 to 159°C at a space velocity of 25,000 h^{-1} upon doping with 35 mol % copper. Using this ligand mediated synthesis gallium oxide nanocrystals can also be produced with crystal sizes of 2.7 ± 0.5 nm. These gallium oxide crystals when used with an Al_2O_3 support show activity towards the ethane dehydrogenation reaction and show reduced deactivation due to coke when compared to a TiO_2 supported catalyst. Reaction with platinum and gallium oxide nanocrystals supported on alumina reached 26% and maintained 11% conversion after 48 hours (at 500°C and WHSV = 0.5 h^{-1}). Our results show the complementary effect of gallium oxide nanoparticles on alumina when utilized in platinum dehydrogenation system. This effect is due to the ability of gallium oxide on alumina to limit coke build-up.

1. Introduction

1.1 Background and Motivation

Transition metal oxide and solid solution metal oxide nanoparticles are of functional interest due to their current widespread commercial application in environmental catalysis[1], their use in fuel cells[2], as pharmacological agents[3], and chemical mechanical planarization abrasives[4]. In particular, ceria and doped ceria mixed oxides are widely utilized in automotive exhaust catalysis as oxygen storage materials due to the facile redox behavior that exists between Ce(III) and Ce(IV). This facile redox couple also makes ceria-based materials active oxidation catalysts and catalyst supports for a wide range of oxidation reactions[5-7] and the industrially important water gas shift reaction(WGS)[8-10]. Doping ceria can promote catalytic properties depending on the cation and the extent of cation replacement. The introduction of zirconium into ceria enhances the formation of oxygen defects within the nanocrystals to promote catalytic activity and also increases the thermal stability of the materials[11,12]. While copper-cerium mixed oxide catalysts show high activity for oxidation and WGS reactions due to the active site created by the incorporated copper and the favorable redox properties of ceria[10,13-18]. Ceria and doped ceria materials are most commonly synthesized through flame aerosol pyrolysis[19], co-precipitation[20], or hydrothermal routes[21]. These synthesis methods require high temperatures to generate crystalline products; however, exposure to high temperatures during synthesis can lessen the catalytic potential of the materials in two ways. Firstly, phase separation and migration of dopants out of the ceria lattice can occur at high temperature, which limits the degree of interaction between dopant and ceria. Secondly,

high temperature processing can lead to increased crystallite size in the final doped ceria product which in turn decreases the oxygen mobility, an important factor for reactions involving the Mars-van-Krevelen mechanism, as oxygen vacancy concentration tends to be highest in small ceria crystallites[22,23].

This paper will describe two low temperature aqueous synthesis methods for transition metal oxide materials, in particular doped ceria materials and gallium oxide. The first method, biomineralization, depends on the silicatein enzyme which has been long used by marine sea sponges to produce solid oxide spicules for defense. The second method, a ligand mediated precipitation, makes use of over 30 years of transition metal sol-gel research to develop a ambient temperature base precipitation technique which directly deposits transition metal oxides.

Biomineralization seeks to utilize biological systems as potentially green and scalable alternatives to typical material synthesis routes. Our work demonstrates that biomineralization is a feasible, green, pathway to the formation of ceria and ceria-zirconia nanoparticles and that these biomineralized materials are functionally equivalent to their chemically synthesized counterparts. Templated biomineralization of ceria has previously been reported by Okuda *et al* who utilized an apoferritin cage to template CeO_2 nanoparticles upon inducing mineralization with HEPES-NaOH in aqueous solution[24]. This process yields nanoparticles ~ 5 nm in size but requires multiple separation steps to remove larger 'bulk' ceria particles formed through reaction of the precipitant with free ceria; that is, ceria precursor in solution that is not associated with a templating ferritin

cage. In contrast, the combined enzymatic mineralization and templating approach described herein exclusively produces ceria nanocrystals and no subsequent particle size selection is required.

Our ligand assisted synthesis of transition metal oxides seeks to utilize the bidentate ligand lactic acid to stabilize the soluble metal complex until oxide precipitation. As described in a classic paper by Livage *et al*[25], direct precipitation of the metal oxide from an aqueous phase metal nitrate or metal chloride precursor would require an elevated pH. As the pH of the reaction mixture increases, the interaction of the metal with the aqueous solution transitions from "*aquo*" (M-OH_2) to "*hydroxo*" (M-OH) and finally to "*oxo*" (M-O). Addition of typical precipitants, such as sodium hydroxide or ammonium hydroxide, raises the pH into the *"hydroxo"* region, leading to dissociation of any weakly bound NO_3^- or Cl^- ligands and precipitation of metal hydroxide particles. These then require a high temperature calcination step to form metal oxide particles. Ligands utilized in sol-gel processing, such as ethylenediaminetetraacetic acid (EDTA), can prevent hydroxide precipitation, however their strong binding also prevents oxide precipitation[26], once again requiring a calcination step to remove the ligand and transform to the metal oxide. In this work we demonstrate a facile method for direct formation of copper cerium oxide nanocrystals at room temperature in aqueous solution. This approach exchanges the nitrate ligands present in a mixed cerium nitrate and copper nitrate precursor solution for the intermediate strength lactate ligand, to shift the precipitation pH from the "*hydroxo*" to the "*oxo*" regime.

1.2 Biomineralization

Biomineralization is process in which living organisms produce inorganic materials. In nature, biomineralized materials commonly take the form of bones, teeth, shells, and cell walls in some unicellular organisms. Biomineralization is thought to have begun more than 750 million years ago, and has been shown to have evolved independently in organisms[27,28]. Although primarily used for structural purposes biomineralized materials are also used for a variety of specialty purposes. For example, in magnetotactic bacteria mineralized iron oxide is used to help the organism orient itself with the earth's magnetic field and sea sponges mineralize silicon oxide for both structural purposes as well as for defense in the form of silica spicules[29].

1.3 Sol-gel chemistry

Sol-gel chemistry is a field in chemistry and materials science studying the interactions and formation of colloidal materials in solution. Understanding the interactions of dissolved transition metals with solvent is critical in the development of strategies for the formation of inorganic colloidal materials such as ceria nanocrystals. The work of Livage et al. has been particularly insightful in this field and has been greatly influential in the work described in this dissertation[25]. Livage et al.'s work qualitatively describes the nature of the interaction of aqueous solvent with dissolved transition metals at different pH's and with different metal oxidation states. As the pH of a solution increases, the favored interaction of the metal with the aqueous solution transitions from "*aquo*" (M-OH_2) to "*hydroxo*" (M-OH) and finally to "*oxo*" (M-O), with the precise pH required for a

'transition' being a function of the identity of the transition metal itself and the associated ligands in solution.

1.4 Materials characterization

1.4.1 X-Ray Diffraction

X-ray diffraction (XRD) can be used to demonstrate the shift in lattice parameter which will accompany the incorporation of other cations in the ceria lattice. Lattice parameter shift along with Raman spectra shift are among the best measurements to prove the incorporation of dopants into the lattice. XRD can also be used to show phase purity and it is important to know that dopant precursors are not forming secondary crystalline oxide phases. XRD is also a useful tool for calculating the crystallite size of nanocrystalline particles. Crystallite size is calculated using the Scherrer equation, and can be used to predict the particle size in well dispersed colloid systems[30]. Another application of XRD is to explore the thermal stability of as synthesized materials. Using non-ambient XRD, the temperature of phase separation can be determined. This is important for determining the maximum concentration which is stable at a certain temperature. Many possible applications for doped ceria require elevated temperatures (e.g. fuel cell electrolyte, catalyst), so knowing the temperature limits of a material is critical to the determination of the optimal working conditions. Non-ambient XRD can also determine thermal stability in terms of crystallite growth. Growth of nanocrystalline particles can greatly affect the surface area of the catalyst which in turn effects the catalytic performance of the material.

1.4.2 Raman Spectroscopy

Raman Spectroscopy is used to examine how dopants change the crystal bonds in a material. In fluorite crystal structured ceria materials there is only one Raman active symmetry T_{2g}, corresponding to the Ce-O bond breathing mode. The bond distance of the Ce-O bonds is effected by incorporation of a dopant, and thus a shift in the frequency of vibration of these bonds is induced. Depending on the dopant element, the Raman peak will shift to higher or lower wave number[31]. Raman spectroscopy is useful in demonstrating that dopant metals are incorporated in the lattice because the peak shift and broadening effects on the Raman peak are dependent on the dopant being integrated in the lattice.

1.4.3 Electron Microscopy

High-resolution transmission electron microscopy (HR-TEM) provides direct evidence of oxide particle size, crystallinity, and dispersion. Size distribution measured from TEM images can be used to prove the size of synthesized particles. Crystallinity of particles and dispersion is visually apparent in HR-TEM. Individual lattice planes can be seen and measured to assist in crystal phase detection. In addition to collecting images, electron microscopy detector attachments also allow us to collect x-ray energy-dispersive spectra (XEDS). XEDS allows for the determination of the elements in our sample qualitatively and quantitatively. Small area XEDS has the sensitivity to determine elemental composition of a single particle. This is important for understanding the distribution of compositions in our sample.

1.5 Cerium oxide and size dependent properties

The properties of cerium oxide change substantially between bulk crystals and nanocrystals. The most drastic changes in properties occur under 10nm. It has been long accepted that the surface layer of cerium oxide is readily reduced, depending on the environment[32]. Naturally, as the size of cerium oxide nanoparticles reduce, this surface effect becomes more substantial. Deshpande et al. have reported that the Ce(III) concentration reached up to 44% in 3nm ceria particles[33]. Higher Ce(III) concentrations also lead to an expansion of the crystal lattice due to the size difference in the Ce(III) and Ce(IV) atomic radii, 1.01 and 0.87 respectively[34]. When ceria is in a reduced state and maintains a cubic fluorite crystal structure there are vacancies where oxygen should be in the lattice. Oxygen mobility is strongly positively correlated with the number of oxygen vacancies[35]. In reactions which follow the Mars-Van Krevelen mechanism oxygen mobility is extremely important for the replacement of reacted oxygen[36,37]. Nanoscale ceria catalysts are therefore not only highly sought after for their high surface area but are also desired for their high oxygen mobility and redox properties.

1.6 Catalysis

CO oxidation catalysts are used commonly as an important component in three-way catalyst systems for both mobile and fixed engines. Reduction of CO is important for environmental reasons because CO has a Global Warming Potential (GWP) 19 times larger than CO_2 and CO is a significant component in the exhaust of petrol engines[38,39]. In addition to being an industrially important reaction, CO oxidation is also use as a common benchmark for a catalysts as an indicator of its performance in other oxidation reactions.

Nanoscale ceria structures are often used as active supports in oxidation catalysts due to their high availability of oxygen in Mars-Van Krevelen type reactions.

WGS is an industrially important reaction and is only growing in importance in the last few years with the increase in natural gas supplies. The WGS reaction is important in steam methane reforming, the Haber process and the Fischer-Tropsch process two of the most important chemical processes in the modern age. Low temperature WGS catalysts are also increasingly important in proto-exchange membrane fuel cell systems where CO is a poison to the fuel cell catalyst. Catalysts that conduct the WGS reaction at low temperature can reach compete conversion where high temperature catalysts are limited due to the shift in equilibrium at high temperatures. Materials like Cu-Ceria are able to completely remove CO from the fuel cell feed to save the precious metal catalyst.

In this paper we will discuss two primary metrics for the performance of a catalyst, light-off temperature and activation energy. Light off curves plot the change in conversion with change in temperature. These plots follow a characteristic S-curve shape. The "light-off temperature" is commonly reported is the temperature at which the reaction conversion reaches 50%. The lower a catalyst's light off temperature the higher its catalytic activity, when all other variables are held constant. This metric is useful when comparing like samples and for directly determining temperature vs. conversion for specific conditions.

Activation energy is an effective measure to compare catalysts when the conditions of the catalysis are not identical. Activation energy is calculated using data collected at low

conversion and where diffusion effects are minimized. In this "kinetic regime" equilibrium and diffusion effects have negligible effect on the reaction rate and the rate equation reduced to the Arrhenius equation (Equ. 1).

$$\boldsymbol{k = Ae^{-E_a/(RT)}} \quad \textbf{(1)}$$

$$\boldsymbol{ln(k) = \frac{-E_a}{R}\left(\frac{1}{T}\right) + ln(A)} \quad \textbf{(2)}$$

Where:

$\boldsymbol{k}$ is the rate constant

$\boldsymbol{T}$ is the absolute temperature

$\boldsymbol{A}$ is the pre-exponential factor

$\boldsymbol{E_a}$ is the activation energy for the reaction

$\boldsymbol{R}$ is the universal gas constant

Measuring a reaction at a few temperatures allows for the determination of the activation energy of the rate limiting step for the reaction with a specific catalyst. By re-arranging the equation (Equ. 2) we can see that a plot of ln(k) vs. T^{-1} would have a linear slope of $-E_a\ R^{-1}$. Using linear regression an activation energy (E_a) can be obtained using experimental values of k and T.

2. Direct Single-Enzyme Biomineralization of Catalytically Active Ceria and Ceria–Zirconia Nanocrystals

2.1 Introduction

Natural biomineralization pathways[40,41] most commonly form amorphous structural materials; for example, calcium carbonate-biopolymer composite mollusk shells[42], iron oxides in the teeth of limpets[43], or structural spicules of silica in sea sponges[44]. Mann, in his classic textbook, categorized biomineralization into either *biologically induced mineralization*, whereby mineralization occurs through a metabolic reaction of precursors in solution, or *biologically controlled mineralization*, whereby the biological system controls the structure of the mineral, but the mineralization process occurs through supersaturation rather than a metabolic turnover of precursors[45]. Without structural control, biologically induced mineralization leads to materials with irregular size, shape, structure and composition, making such an approach generally unfavorable for the formation of well-defined functional nanomaterials. In contrast, a reliance only on precipitation from a supersaturated solution limits the materials palette available to thermodynamically favorable products unless, as in a *biotemplating* approach, an additional reactive chemical species is introduced; *e.g.* in functional material production, the use of Na_2S as a reactive sulfur source in CdS biomineralization[46] and H_2O_2 as an oxidizing agent in Co_3O_4 biomineralization for battery applications[47]. The challenge to producing 'green' functional materials by biomineralization is thus to develop approaches that *combine* metabolic, or more generally active enzymatic precursor turnover, with biotemplating in a single biological system; we term this combination *direct* biomineralization. Herein, we

demonstrate a single enzyme active for the direct biomineralization of cerium oxide and cerium-zirconium oxide solid solution nanoparticles. To the best of our knowledge, there are no prior reports of direct biomineralization of these widely utilized catalytic materials, nor are there prior reports of biomineralized oxide materials being used as active heterogeneous catalysts for gas phase reactions.

The motivation for the current direct biomineralization work comes from our group's previous work developing a single enzyme for direct sulfide biomineralization[48] and the fascinating reports regarding silicateins, silica proteins, first identified by Shimizu *et al* as responsible for biomineralization of silica spicules in the marine sponge *Tethya aurantia*[49]. These silicateins assemble into axial filaments and actively turnover a precursor, most likely silicic acid, in the ocean to form largely amorphous hydrated silica spicules in sea sponges. The amino acid sequences of the most abundant silicateins isolated from *Tethya aurantia* (α- and β-forms) are very similar (50% by sequence, up to 75% by function) to the well-studied cathepsin-L family of hydrolytic enzymes, suggesting a mechanistic pathway to silica from the tetraethylorthosilicate precursor via hydrolysis of ligands surrounding the precursor[50]. For a full discussion of the use of silicatein in inorganic material synthesis we refer the reader to the excellent review by Andre *et al*[51].

Native or recombinant forms of silicatein have previously been successfully applied to biomineralization of silicon dioxide[50], titanium dioxide[52], gallium(III) oxide[53], tin dioxide[54], and barium titanate oxyfluoride[55] particles. This body of work is complemented by that of the Tremel group who have sought to utilize surface immobilized silicatein to

mineralize thin films of multiple materials onto inorganic supports materials[54,56-58]. Of particular relevance to the current work is the pursuit of biomineralized functional materials. One particular challenge in this area is the balance of crystalline *versus* amorphous structure formed during mineralization, as typically the crystalline phase is the desirable component for functional activity. For example, silicatein biomineralization of both titanium dioxide and zirconium dioxide is reported to lead to the formation of relatively sparse nanocrystalline domains within largely amorphous matrices[56,57], and crystalline γ-Ga_2O_3 is only formed at very low precursor concentration[53]. In the pursuit of highly crystalline materials, Bawazer *et al* developed an engineered recombinant form of silicatein that is active in the formation of ~5 nm partially crystalline titania, demonstrating a critical link between enzyme sequence and nanoparticle crystallinity[59]. In contrast, $BaTiOF_4$ was successfully biomineralized in crystalline form although unfortunately without any corresponding functional property measurements, most likely due to the relatively low material yield of many biomineralization strategies; the authors in that work note that insufficient material was obtained for X-ray diffraction (XRD) analysis[55].

While the pursuit of functional materials is ongoing, there are, to the best of our knowledge, no prior reports of the functional properties of directly biomineralized catalytic oxides, although there are some reports regarding the function of other directly biomineralized materials; for example, the use of directly biomineralized metal chalcogenide quantum dots in photovoltaic applications[60], the magnetic properties of fungi mediated biomineralized magnetite[61], the ferroelectric properties of fungi mediated barium titanate[62], and reports of

fungi mediated manganese containing materials[63], or bacterial mediated γ-FeOOH to form α-Fe_2O_3 base Li-ion battery electrodes upon a brief heat treatment[64].

2.2 Results and Discussion

Herein we describe the single enzyme direct biomineralization of ceria and ceria zirconia solid solution nanocrystals of less than 3 nm diameter from aqueous solution of cerium(IV) ammonium nitrate and zirconium(IV) dinitrate oxide. Nanocrystal biomineralization of the oxides occurs without the addition of any reducing agent or additional templating species or any post-mineralization heating. The resulting nanocrystals are demonstrated as active catalysts for carbon monoxide oxidation, one of a large number of potential energy and environmental catalysis applications ranging from water gas shift catalysts, to promoters in automotive three-way catalysts, to oxidation catalysts for direct hydrocarbon solid oxide fuel cells. To the best of our knowledge, this work is the first demonstration of single enzyme mediated direct biomineralization of an oxide, the first demonstration of directly biomineralized solid solution crystalline nanoparticles, and the first demonstration that directly biomineralized oxide materials are functionally active catalysts.

We have engineered a form of recombinant ceria-mineralizing silicatein from *S. domuncula* (NCBI accession number Q6YD92.1) denoted hereafter as rCeSi, by taking the wild-type sequence and generating serial truncations of the N- and C-terminal to improve expression yield from *E. coli*. We identified a truncated sequence containing amino acids 124-217 as well as a C-terminal hexahistidine tag that exhibited consistently high expression from *E. coli* (rCeSi). Previous studies to engineer silicatein have used DNA

shuffling to diversify silicatein sequences as well as including C-terminal hexahistidine tags[59].

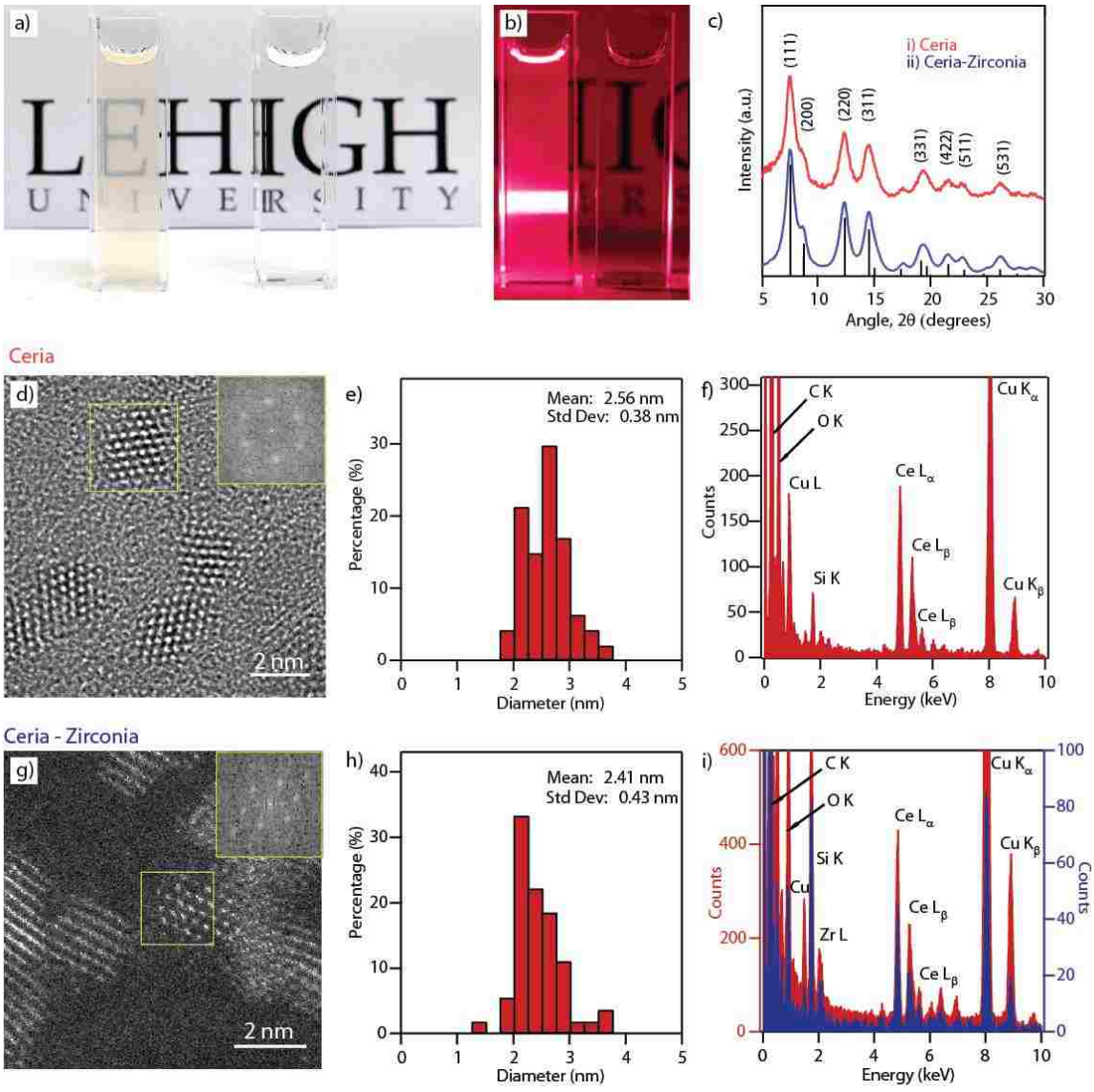

Figure 1: *Ceria and Ceria-Zirconia Nanocrystal Biomineralization. a) Photograph under natural light and b) photograph with red laser illumination of cerium(IV) ammonium nitrate precursor incubated with rCeSi (left) and without rCeSi (right). An opaque pale-yellow sol is formed in the presence of rCeSi enzyme but not in the control sample which shows no precipitation or color change. The laser light scattering demonstrates the presence of colloidal particles in the sample with rCeSi enzyme and no particles in the sample without rCeSi. The laser beam is coming from the right and is passing through*

both sample vials. c) Synchrotron powder X-ray diffraction spectra of the dried as-synthesized product of incubation of (i) rCeSi with the cerium(IV) ammonium nitrate and (ii) rCeSi with a 1:1 molar mixture of cerium(IV) ammonium nitrate and zirconium(IV) dinitrate oxide (ICSD collection code 156250, substantial peaks identified). d) Representative HRTEM image of as-synthesized ceria nanocrystals; the inset fast Fourier transform (FFT) from the particle in the yellow box is consistent with the [1$\bar{1}$0] projection of the CeO_2 (fluorite) structure; e) corresponding spherical equivalent particle size distribution – with no particles larger than 4 nm being observed; and f) XEDS spectrum confirming the presence of Ce and O in the particles. The Cu and C signals originate from the TEM grid and the Si signal is an artefact from the Si drift detector; g) HAADF-STEM image of the as-synthesized ceria-zirconia particles; the inset FFT obtained from the particle in the yellow box is consistent with the [1$\bar{1}$0] *projection of the fluorite structure; h) corresponding spherical equivalent particle size distribution for the ceria-zirconia sample; i) the XEDS spectrum from a single nanoparticle (blue) and the summation of ten spectra from extended area nanocrystal groupings (red) confirming the presence of both Ce and Zr in the nanocrystals.*

Incubation of the rCeSi enzyme with an aqueous cerium(IV) ammonium nitrate (CAN) precursor solution for 24 h led to the formation of an opaque, yellow solution, showing laser light scattering properties consistent with the formation of a colloid, Figure 1a and 1b. No corresponding color change or colloid formation was observed for the control samples which were identical in composition and synthesis conditions to the primary samples except that no rCeSi was added, Figure 1a and 1b. Aqueous CAN solutions are shelf-stable and do not undergo spontaneous oxidation to form nanocrystals within this time period at this temperature and *p*H. XRD patterns collected in our laboratory can be indexed to the fluorite structure of ceria, and are consistent between batches, Figure 2.

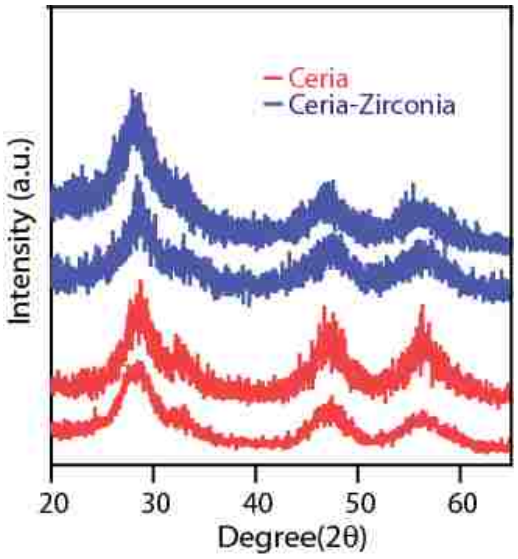

Figure 2: *Laboratory XRD patterns of two batches each of the dried as-synthesized product of incubation of a) (red) rCeSi with the cerium(IV) ammonium nitrate and b) (blue) rCeSi with a 1:1 molar mixture of cerium(IV) ammonium nitrate and zirconium(IV) dinitrate oxide.*

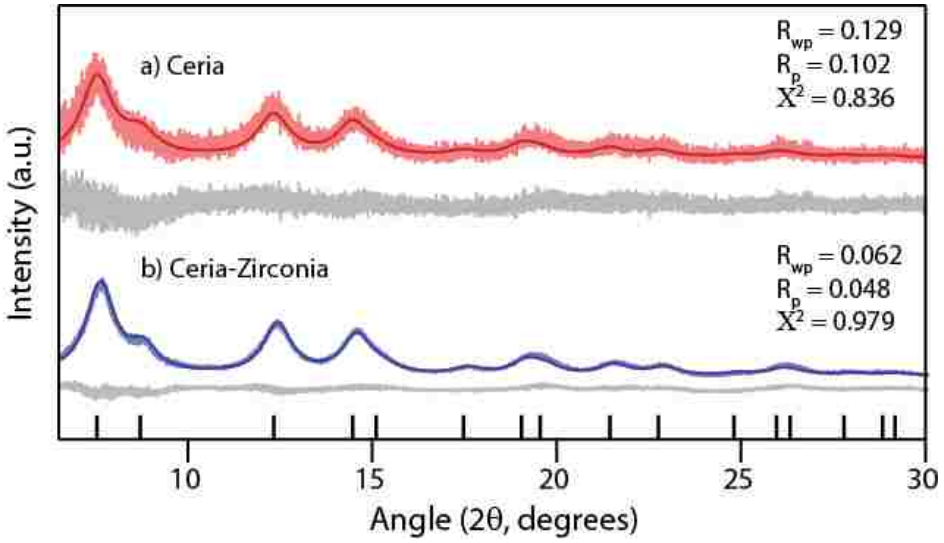

Figure 3: *Synchrotron powder X-ray diffraction spectra and Rietveld refinement of the dried as-synthesized product of incubation of a) (red) rCeSi with the cerium(IV) ammonium nitrate and b) (blue) rCeSi with a 1:1 molar mixture of cerium(IV) ammonium nitrate and zirconium(IV) dinitrate oxide. Observed (light line), calculated (dark line), and difference (grey) patterns are shown. Expected peak positions for the fitted ceria structure, space group $Fm\bar{3}m$, are also shown.*

The synchrotron XRD pattern, shown in Figure 1c, of the solid pellet centrifuged from this opaque solution shows peak positions and peak broadening consistent with the formation

of CeO_2 nanoparticles having the fluorite structure (ICSD collection code 156250). Rietveld refinement, Figure 3, of the XRD pattern confirms the fluorite structure, space group $Fm\bar{3}m$, with a lattice parameter of 5.449(1) Å and mean crystallite size, estimated from the Lorentzian crystallite size broadening parameter as implemented in GSAS[65], of 22.1 ±0.2 Å.

Figure 1d shows a high resolution transmission electron microscopy (HR-TEM) image of the centrifuged and dried pure ceria sample, demonstrating that the ceria has been mineralized as highly facetted individual crystalline nanoparticles. The interplanar spacings and angles present in these phase contrast images are in good agreement with those expected for the fluorite structure of CeO_2, Figure 4. The ceria nanoparticles have a tight size distribution with mean particle diameter (based on area equivalent spherical particles) of 2.56±0.38 nm, Figure 1e, which is consistent with the crystallite size estimated from XRD. No large crystallites or amorphous regions were observed during imaging of multiple samples. Furthermore, X-ray energy dispersive spectroscopy (XEDS) analysis confirms the presence of only cerium and oxygen within the particles, Figure 1f. While there is likely residual carbonaceous material, including the enzyme, in the as-prepared sample, the particles do not appear to be bound within any carbonaceous matrix and are stable as a colloid upon re-suspending in dilute nitric acid without any additional processing.

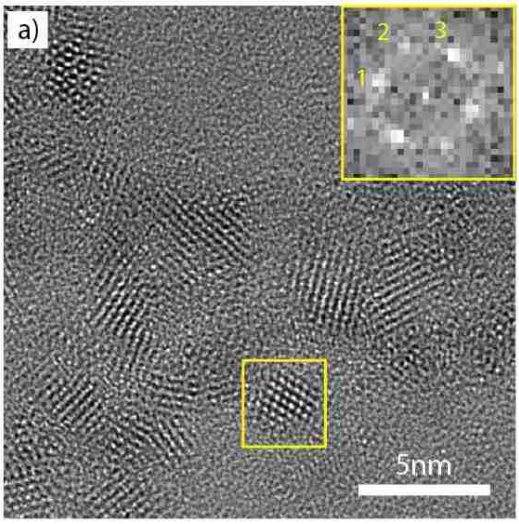

b) Nanocrystal identification as fluorite-type CeO_2

	Measurement	Matching
Plane 1	d=3.08 Å	3.12 Å (111)
Plane 2	d=2.80 Å	2.71 Å (002)
Plane 3	d=3.10 Å	3.12 Å ($11\bar{1}$)
<1, 2>	49.8°	54.7°
<1, 3>	73.5°	70.5°
<2, 3>	56.7°	54.7°

Figure 4: *HR-TEM analysis of dispersed ceria nanoparticles prepared via biomineralization. a) HR-TEM image of some representative pure ceria nanoparticles. Inset is a Fast Fourier Transform obtained from the individual nanoparticle contained in the yellow box. b) The interplanar spacings and angles of the lattice fringes in this particle are in good agreement with the [$1\bar{1}0$] projection of ceria having the fluorite structure.*

To the best of our knowledge, this is the first report of a protein biologically inducing the mineralization of ceria, as opposed to biologically templating mineralization[24]. It is especially important to note that unlike other preparation methods, ceria nanocrystal formation occurs in aqueous solution without the addition of a base or elevation of temperature and in the absence of an explicit chemical structure directing agent. Furthermore, these ceria nanoparticles are amongst the smallest reported in the literature[66,67]. The ability to form such small particles is a consequence of the direct biomineralization of the material. The majority of chemical approaches to ceria nanoparticle synthesis utilize elevated temperatures during synthesis or during a post annealing step to form the crystalline oxide[6]. While we utilize an annealing step to remove any carbonaceous material prior to catalytic testing, elevated temperature is not required to form the crystalline oxide.

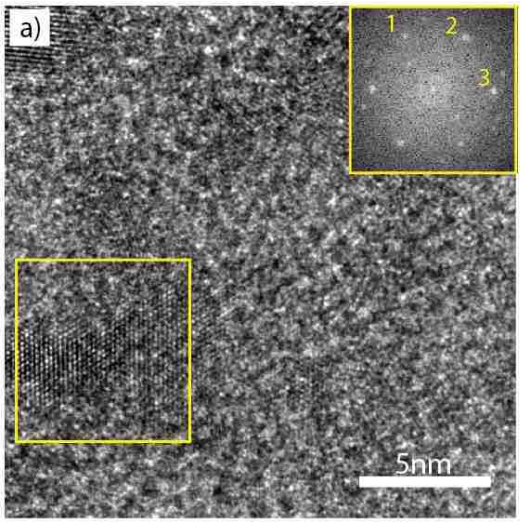

b) Nanocrystal identification as tetragonal ZrO_2

	Measurement	Matching
Plane 1	d=1.81 Å	1.81 Å $(1\bar{1}2)$
Plane 2	d=1.79 Å	1.79 Å (200)
Plane 3	d=1.80 Å	1.81 Å $(11\bar{2})$
<1, 2>	59.1°	59.6°
<1, 3>	61.9°	60.8°
<2, 3>	59.0°	59.6°

Figure 5: *HR-TEM analysis of pure zirconia nanoparticles prepared via biomineralization. a) HR-TEM image of some representative pure zirconia nanoparticles. Most of the nanoparticles in the sample have a low degree of crystallinity; highly crystalline zirconia nanoparticles were only encountered very sporadically. Inset is a Fourier Transform of one such highly crystalline area boxed in yellow. b) Interplanar spacing and angle measurements of this particle are in good agreement with the [021] projection of zirconia having the tetragonal structure.*

Attempts to biomineralize pure zirconia from zirconium(IV) dinitrate oxide (ZDO) via rCeSi leads to the formation of a solid zirconia phase; however, the product consists primarily of slightly larger (5-10 nm) highly disordered particles with only a relatively few highly crystalline tetragonal zirconia nanoparticles present, Figure 5. This is similar to prior reports of amorphous silicon dioxide[50], titanium dioxide[52], and gallium(III) oxide[53]. In contrast, incubation of rCeSi with a 1:1 mixture of CAN and ZDO leads to the formation of an opaque sol after 24 h.

As with the pure ceria sample, XRD patterns of the centrifuged material obtained from this mixed CAN and ZDO solution can be indexed to the fluorite structure of ceria and are consistent between batches, Figure 2. The higher resolution synchrotron XRD pattern of

the centrifuged solid material, Figure 1c, is also consistent with the formation of single phase fluorite structured nanoparticles, space group $Fm\bar{3}m$. Rietveld refinement, Figure 3, provides lattice parameter of 5.437(2)Å and average crystallite size, again from the Lorentzian isotropic size broadening, of 24.53± 0.1 Å. When compared with the values obtained for the pure ceria sample, the measured contraction in lattice parameter is consistent with formation of a ceria-zirconia solid solutions[11,68,69].

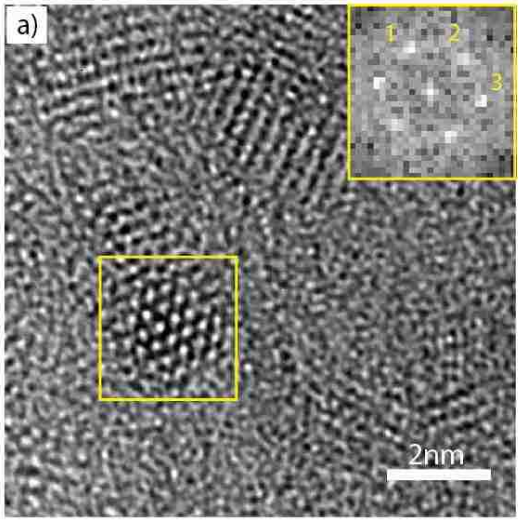

b) Nanocrystal identification as fluorite-type CeO_2-ZrO_2 solid solution

	Measurement	Matching
Plane 1	d=3.05Å	3.12 Å (111)
Plane 2	d=2.99 Å	3.12 Å (11$\bar{1}$)
Plane 3	d=2.75 Å	2.71 Å (002)
<1, 2>	71.8°	70.5°
<1, 3>	56.1°	54.7°
<2, 3>	52.2°	54.7°

Figure 6: *HR-TEM analysis of ceria-zirconia mixed oxide nanoparticles prepared via biomineralization. a) HR-TEM image of some representative ceria-zirconia mixed oxide nanoparticle. Inset is the Fast Fourier Transform obtained from the individual nanoparticle contained in the yellow box. b) The interplanar spacings and angles of the lattice fringes in this particle are in good agreement with the* [1$\bar{1}$0] *projection of ceria-zirconia having the fluorite structure.*

HAADF-STEM analysis, Figure 1g, again confirms the formation of individual crystalline nanoparticles and the absence of any larger particles or amorphous material (see also Figure 6). The particles have a narrow size distribution, Figure 1h, with a mean size of 2.41 ± 0.43 nm, which is in good agreement with that deduced from XRD.

Compositional analysis of individual nanoparticles by XEDS was attempted, but in many cases we were unable to collect a statistically significant number of X-rays before the nanoparticle was irretrievably damaged by the electron beam. Instead XEDS spectra could be more reliably collected from groups of two or three particles and analyses on many such NP groupings provided similar XEDS spectra. Figure 1i shows an XEDS spectrum derived from the summation of ten such 'extended area' spectra and one example from an individual nanoparticle. This semi-averaging analysis method supports the conclusion that ceria-zirconia solid solution nanoparticles are formed by incubation of rCeSi in the presence of both Ce and Zr containing precursors. The relative atomic concentration of Ce : Zr, calculated using a Cliff-Lorimer type analysis, was determined to be approximately 82% : 18%. As with the case of pure ceria, this is the first report of biologically induced mineralization of mixed cerium oxide-zirconium oxide nanoparticles, and their size are amongst the smallest reported to date for ceria-zirconia nanocrystals[70].

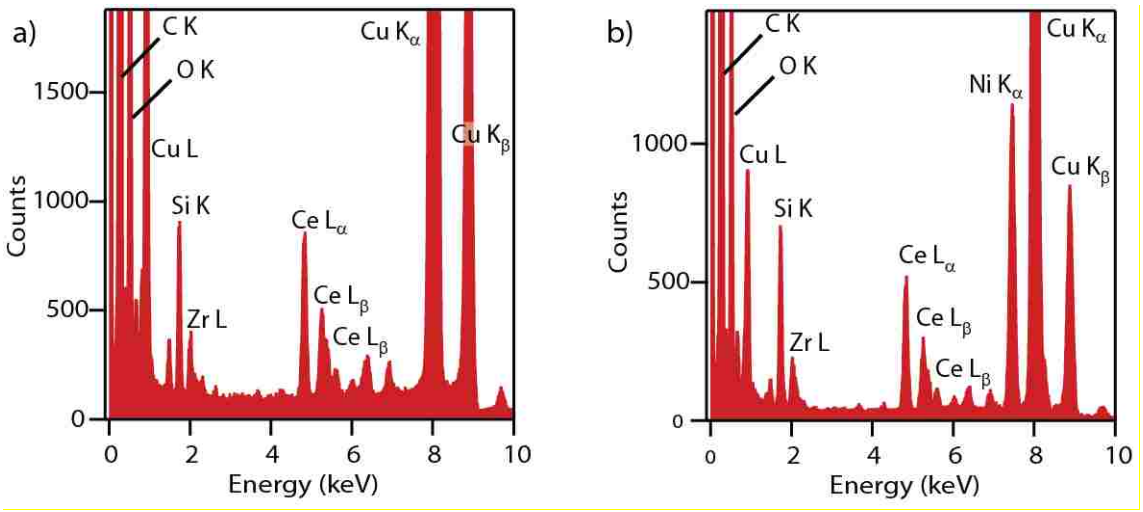

Figure 7: *XEDS spectra of ceria zirconia nanoparticles prepared with different nominal Ce:Zr precursor ratios. The XEDS spectra shown are summed from data acquired from several extended area nanocrystal groupings for samples prepared with a) 1:2 ratio and b) 1:4 ratio of cerium and zirconium precursors. Atomic ratios determined from XEDS are 83:17, and 81:19 respectively.*

Interestingly, when the nominal ratio of zirconium to cerium was increased in the synthesis procedure by adjusting the precursor concentrations, their relative atomic concentration of the nanoparticles remained unchanged. Samples synthesized with nominal Ce:Zr ratios, 1:2 and 1:4 in solution, at the same total precursor concentration as the other materials in this study, yield particles with atomic ratios of 83:17, and 81:19, respectively, as determined by XEDS analysis, Figure 7. This lack of sensitivity to increased Zr content in the solution may be due to the intrinsic enzymatic biomineralization turnover kinetics of cerium versus zirconium that is not substantially influenced within the current range of precursor concentrations explored to date. It should certainly be feasible to increase the zirconium content in fluorite structured nanoparticles as demonstrated for chemically synthesized materials[71,72].

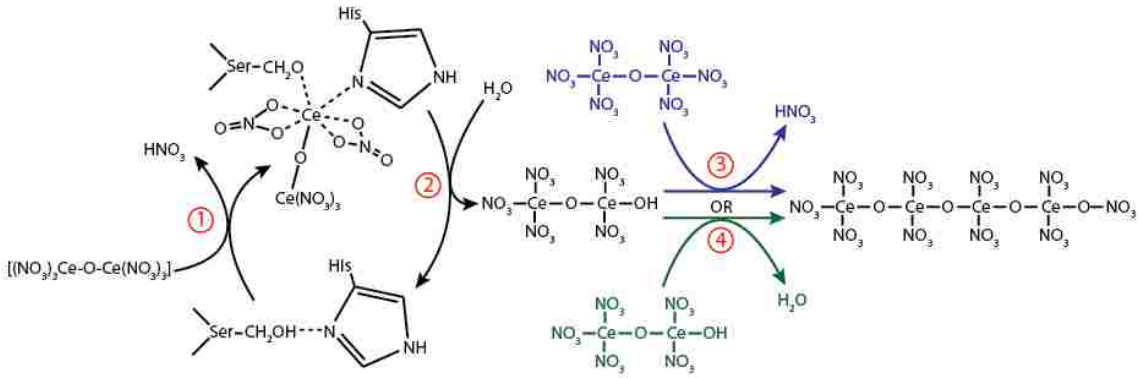

Figure 8: *Proposed Mechanism for the Formation of Cerium Dioxide Nanocrystals from Cerium Ammonium Nitrate. 1) dissociative binding of the precursor to the active site of rCeSi, 2) hydrolysis of the precursor, and either 3) subsequent condensation of a precursor molecule and a hydrolyzed molecule or 4) dehydration of two hydrolyzed precursor species.*

These results unequivocally demonstrate that rCeSi is active to biologically induce *and* control mineralization of crystalline pure ceria, pure zirconia and mixed cerium-zirconium

oxide nanoparticles under ambient conditions. The catalytic mechanism of both ceria and zirconia biomineralization by rCeSi is likely to be similar to that previously proposed for native silicatein, as the proposed catalytic residues of silicatein are preserved in the rCeSi enzyme[44]. The resultant rCeSi from N- and C-terminal truncations is similar to the mature, protease-resistant fragment of *S. domuncula* silicatein isolated directly from spicules[73]. While the exact structure of the CAN precursor in solution is still the topic of some debate, most recent studies conclude that it exists as a dimeric entity with bridging Ce-O-Ce bonds[74,75]. The nature of the six-coordinating species around each cerium atom in this dimeric entity varies between reports, possibly due to the variations in the solvent pH employed, but for simple dissolution of the precursor in water, the coordinating species are likely to be a mixture of $(NO_3)^-$, OH^-, and H_2O[74]. In Figure 8 we suggest a hydrolysis mechanism analogous to that proposed previously for biomineralized silica[50], titania[52] and gallium oxide[53] using silicatein. Variations in the nature or number of the coordinating ligands surrounding the Ce-O-Ce dimeric structure in the solvated precursor will alter the number of hydrolysis steps required to form the oxide. Interestingly, attempts in our laboratory to utilize a Ce(III)-type precursor, Ce(III) nitrate, did not lead any observable mineralization, further indicating that the structural state of the precursor in solution is critical to the mineralization mechanism.

This proposed mechanism, whereby a serine and histidine pair within the enzymatic active site form an acid/base pair to catalyze hydrolysis of the precursor, draws upon the sequence and structural similarities between the α-form of native silicatein and the hydrolytic enzyme cathepsin L[50]. This has been experimentally demonstrated for tetraorthosilicate

hydrolysis by observing a removal of function through site directed mutagenesis to replace either the purported active serine histidine or serine residue with alanine[76], and has been indicated as the mechanism for gallium hydroxide and gallium oxide biomineralization from gallium nitrate[53]. In our case, the hydrolysed precursor subsequently undergoes condensation or nitrate removal to form ceria. The formation of crystalline ceria, rather than crystalline cerium hydroxide or an amorphous phase, we hypothesize is templated by hydrogen bonding interactions between hydroxyls on the rCeSi and the hydrolyzed precursors; again this mineralizing and templating mechanism has been proposed for the native silicatein in the biomineralization of silica[44,50], titania[52] and gallium oxide[53].

Unlike the case of pure zirconia, we find no evidence of particles larger than 4 nm or amorphous regions in the ceria or ceria-zirconia materials further demonstrating an intimate interaction between the two elements rather than independent mineralization of ceria and zirconia. The observed specificity of rCeSi towards templated biomineralization of purely crystalline materials only for ceria-rich compositions is perhaps unsurprising given the previously demonstrated need to engineer material specific variants to selectively biomineralize crystalline silica or titania[59]. This is particularly true given that the commonly observed crystal structures of zirconia are either monoclinic or tetragonal, whereas those for ceria and ceria-rich ceria-zirconia mixed oxides are both cubic.

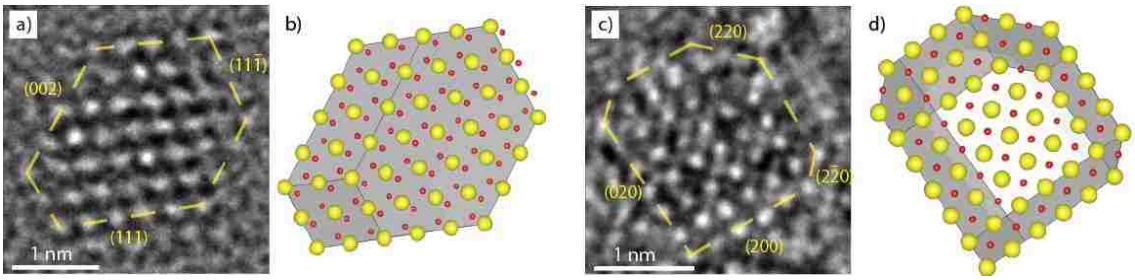

Figure 9: *Faceting of Biomineralized Ceria Nanocrystals. Representative a,c) HR-TEM images of biomineralized ceria having polyhedral and truncated cubic morphology nanocrystals; the schematic diagrams in b) and d) are plausible reconstructions of the NP shown in a) and c) respectively. The polyhedral nanocrystals are the more abundant entities.*

Both polyhedral and cuboid particle shapes were found in the biomineralized ceria nanocrystals (see Figure 9), with the polyhedral being the dominant shape. The exposure of {111} and {200} -type surface facets results in a polyhedral shape, while predominant {200} facet terminations form cuboid-like nanocrystals. These morphologies are consistent with those found in comparable materials synthesized via traditional chemical routes at elevated temperature[77], indicating that while rCeSi clearly both induces and controls ceria biomineralization, it does not template in such a way to produce surface facet distributions that deviate from the typically expected distribution. As with chemically synthesized nanocrystals, the polyhedral shape is more commonly observed in the biomineralized materials due to the comparable surface energies of the {111} and {200} facets[77]. In common with the ceria nanoparticles, polyhedral and cuboid shapes were also found in the biomineralized ceria-zirconia samples, with the polyhedral shape being dominant.

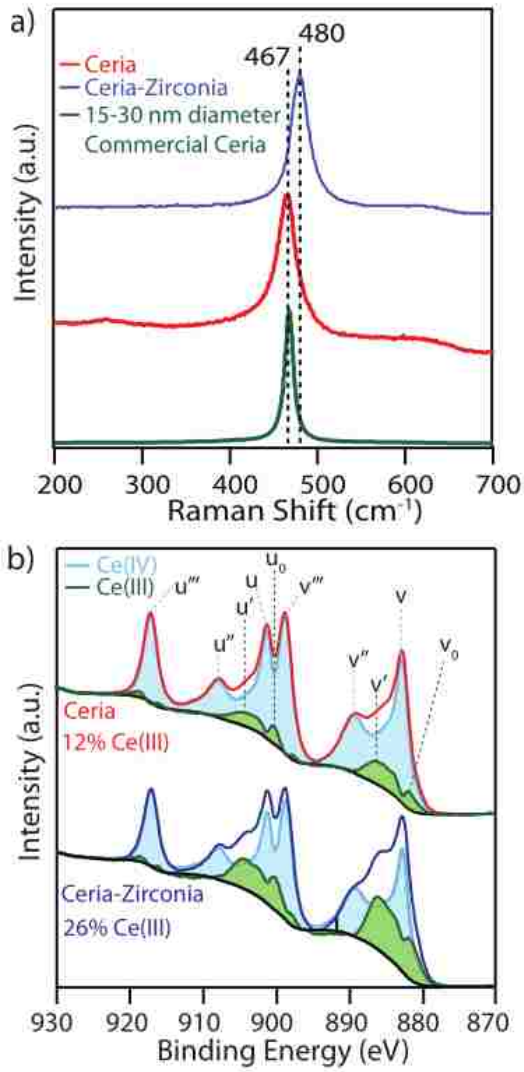

Figure 10: *Raman and X-Ray Photoelectron Spectroscopic Analysis a) Raman spectra collected on as-prepared samples of biomineralized ceria and ceria-zirconia and from the commercially obtained referenced sample of ceria. The increase in measured Raman shift for the ceria-zirconia sample is consistent with the formation of a solid solution. b) X-ray photoelectron spectra of the Ce(3d) region of the biomineralized ceria and ceria-zirconia samples following annealing of both powders in air at 500°C for 20 min demonstrating the increased Ce(III) concentration, and thus higher oxygen defect concentration, upon doping with zirconia.*

The Ce-O bond within the fluorite structure is Raman active with an expected peak position for pure ceria of ~462 cm^{-1} [78,79]. Formation of a ceria-zirconia solid solution shifts this Ce-O bond vibrational frequency to a higher wavenumber[78-80]. Figure 10a) shows the Raman

spectra for the as-synthesized, non-heat-treated, biomineralized ceria and ceria-zirconia, and the purchased commercial pure ceria reference sample. Both the biomineralized and commercial pure ceria show peaks at the expected position of 467 cm^{-1}. In contrast, the peak position of the biomineralized ceria-zirconia is shifted to 480 cm^{-1} providing further confirmation of the formation of ceria-zirconia solid solution nanoparticles by the enzyme in the aqueous phase at ambient temperature.

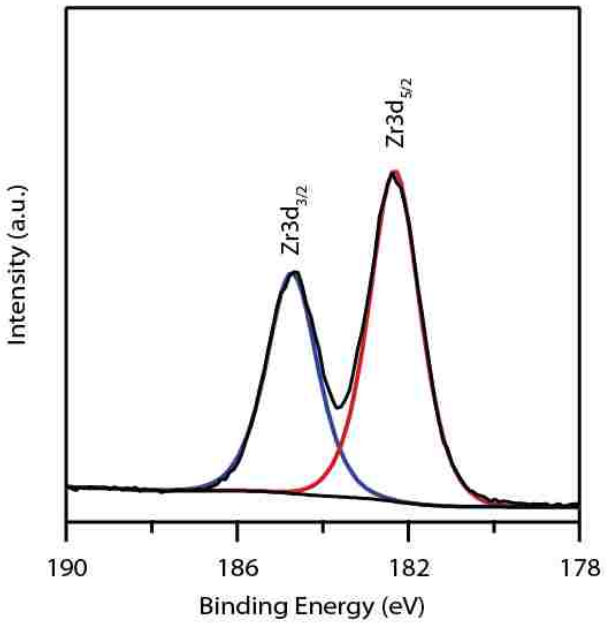

Figure 11: *Zr (3d) XPS analysis of the biomineralized ceria-zirconia sample. High resolution XPS spectrum of the Zr(3d) region from the mixed ceria-zirconia biomineralized sample showing the spin orbital doublet Zr3*$d_{5/2}$*-Zr3*$d_{3/2}$ *with binding energies of 182.4 and 184.8 eV respectively. This demonstrates the presence zirconium in the 4+ oxidation state in the mixed oxide sample. No other peaks corresponding to Zr in lower valence states were detected.*

Cerium is found in both the 3+ and 4+ oxidation state as shown in the XPS spectrum presented in Figure 10b. XPS peaks are labeled U and V, following the naming convention set by Burroughs *et al*, representing the spin orbit doublet $3d_{5/2}$ and $3d_{3/2}$ respectively[81]. The peaks u, v, u'', v'', u''', and v''' correspond to cerium in the 4+

oxidation state, where the u''' and v''' result from the Ce3d^9 O2p^6 Ce4f^0 final state and u, v, u'', and v'' result from a mixing of the Ce3d^9 O2p^5 Ce4f^1 and Ce3d^9 O2p^4 Ce4f^2 final states[82]. The peaks designated u^0, v^0, u', and v' correspond to cerium in the 3+ oxidation state, whereas u^0, v^0, u', and v' peaks result from a mixing of the Ce3d^9 O2p^5 Ce4f^2 and Ce3d^9 O2p^6 Ce4f^1 final states[82]. Annealing the samples in air leads to an increased Ce(III) content (26%) in the ceria-zirconia sample as compared to pure ceria material (12%). This increased Ce(III) concentration is consistent with previous reports[11,83]. Incorporation of zirconium into the ceria lattice, has been shown to reduce the oxygen vacancy formation energy and stabilize oxygen vacancies leading to a shift in the ceria redox equilibrium and an associated increase in Ce(III) concentration[84]. The determined Ce(III) concentration is within the range of previous reports[85-87]. XPS analysis of the Zr(3d) region, see Figure 11, further confirms the presence of the zirconium in the mixed sample and suggests it exists solely in the 4+ oxidation state.

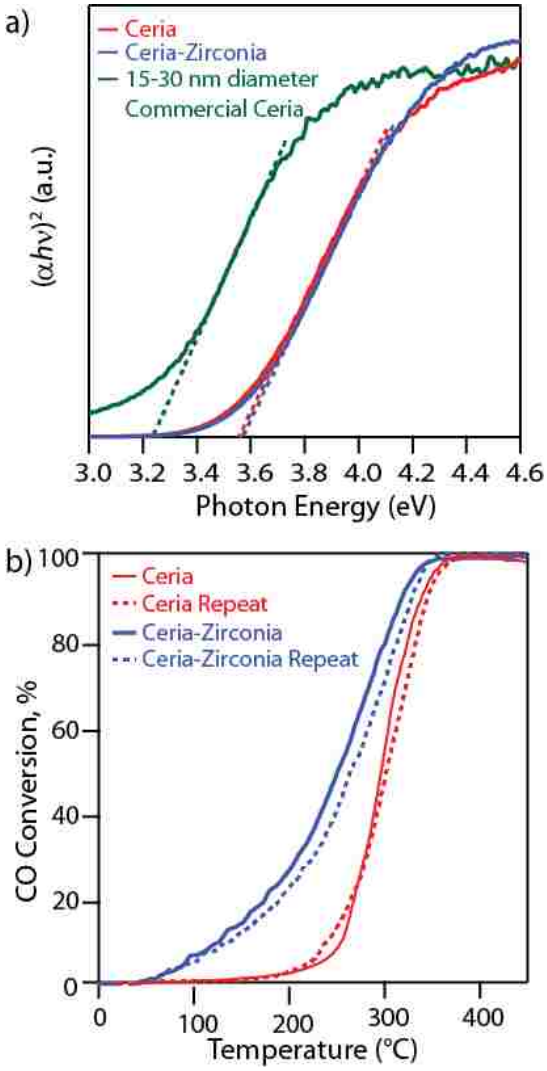

Figure 12: *Optical Properties and Catalytic Activity towards CO Oxidation: a) Optical band gap determination for the as-synthesized biomineralized ceria and ceria-zirconia nanocrystals compared to larger grained (15-30 nm) commercially purchased ceria. The increase in band gap is indicative of the quantum confinement of the < 3 nm diameter biomineralized nanocrystals. b) CO conversion as a function of temperature for comparing the catalytic activity of biomineralized ceria and ceria-zirconia nanoparticles. The temperature required to achieve 50% conversion for the ceria sample is 304 °C, whereas that for the ceria-zirconia material is 252 °C. This reduction in temperature is a consequence of the enhanced reducibility and increased thermal stability of the ceria material upon incorporation of zirconium atoms within the structure. Data for a second repeat of the light-off measurement on the same sample is included.*

The direct optical band gap for our biomineralized ceria and ceria-zirconia materials and a commercial sample containing 15-30 nm ceria nanoparticles were determined to be

3.55(3), 3.57(3), and 3.22(3) eV, respectively, Figure 12a. The significant increase in band gap for the biomineralized ceria compared with the commercial ceria material is consistent with expectations and prior reports of quantum confinement in similarly sized chemically synthesized ceria nanocrystals[88]. An simplistic type of Vegard's law relationship has been shown to apply to the band gap of some alloy semiconductors[89]. All other things being equal, increasing the zirconium content in ceria should have the effect of increasing the band gap, due to the -band gap of bulk cubic zirconia being 6-7eV[90]. However, prior literature has shown that an increase in Ce(III) concentration in $Ce_{1-y}Zr_yO_{2-x}$, along with the associated increase in oxygen vacancy concentration, leads to the formation of a partially occupied $4f^1$ band that reduces the band gap of oxygen deficient ceria[91,92]. As shown in Figure 4b, there is a significant increase in Ce(III) concentration upon zirconia incorporation. Therefore, the lack of measured band gap increase upon Zr doping that may be predicted from a simple Vegard's law approach is most likely due to the opposing influence of increased oxygen vacancy concentration. In addition, numerous subtle factors including influence of chemical environment and capping ligands can potentially influence the measured band gap.

The underlying motivation for introducing zirconium atoms into ceria is to enhance the thermal stability, oxygen storage capacity, and associated catalytic activity of the material relative to that of pure ceria. Hence, CO oxidation was chosen as a simple test reaction to characterize the catalytic performance of our biomineralized materials. CO light-off curves, presented in Figure 12b, demonstrate enhanced activity of the biomineralized ceria-zirconia sample through a 52 ^{o}C reduction in the temperature (from 304 ± 5 ^{o}C down to

252 ± 5 °C) to achieve 50% CO conversion. For comparison, commercial ceria (Alfa Aesar, 15-30 nm), under identical reaction conditions, exhibited a 50% conversion at 293 ± 5 °C, which is in reasonable agreement with the light-off data for our biomineralized pure ceria nanoparticles. Repetition of the experiment utilizing the same sample showed very little shift in the light-off curve, indicating the stability of our biomineralized materials.

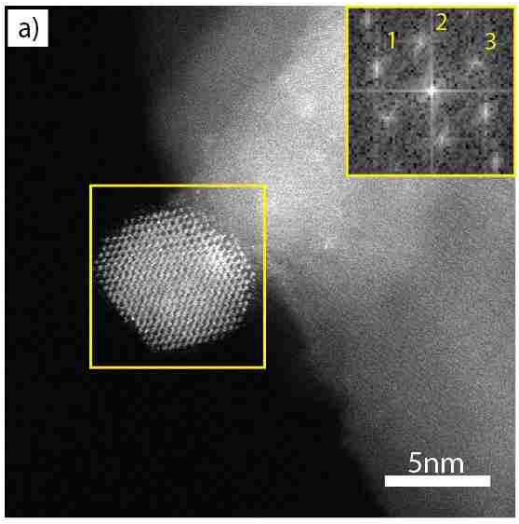

b) Nanocrystal identification as fluorite-type CeO_2

	Measurement	Matching
Plane 1	d=2.82Å	2.71 Å (002)
Plane 2	d=3.28Å	3.12 Å (111)
Plane 3	d=3.16Å	3.12 Å ($11\bar{1}$)
<1, 2>	56.9°	54.7°
<1, 3>	54.0°	54.7°
<2, 3>	69.1°	70.5°

Figure 13: *HAADF-STEM analysis of biomineralized ceria nanoparticles after catalysis. a) Micrograph of a representative ceria nanoparticle after use as a CO oxidation catalysis. Inset is a Fast Fourier Transform from the nanoparticle. b) The interplanar spacings and angles of the lattice fringes in this nanoparticle are in good agreement with the* $[1\bar{1}0]$ *projection of ceria having the fluorite structure.*

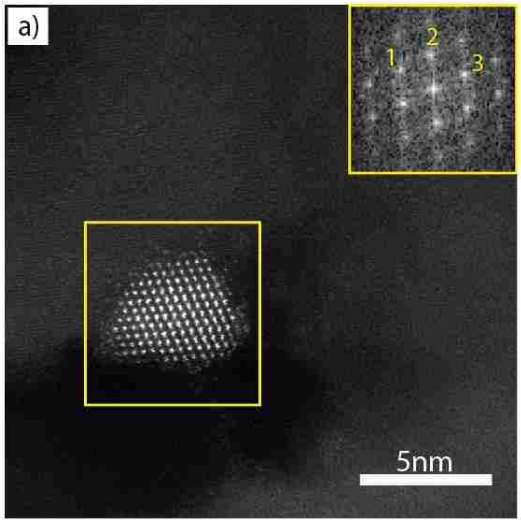

b) Nanocrystal identification as fluorite-type CeO_2-ZrO_2 solid solution

	Measurement	Matching
Plane 1	d=2.82 Å	2.71 Å (002)
Plane 2	d=3.23 Å	3.12 Å (111)
Plane 3	d=3.25 Å	3.12 Å ($11\bar{1}$)
<1, 2>	55.1°	54.7°
<1, 3>	55.1°	54.7°
<2, 3>	69.8°	70.5°

Figure 14: *HAADF-STEM analysis of biomineralized ceria-zirconia mixed oxide nanoparticles after catalysis. a) Micrograph of a representative ceria-zirconia nanoparticle after use as a CO oxidation catalyst. Inset is a Fast Fourier Transform from the individual nanoparticle. b) The interplanar spacings and angles of this particle are in good agreement with the* $[1\bar{1}0]$ *projection of ceria-zirconia having the fluorite structure.*

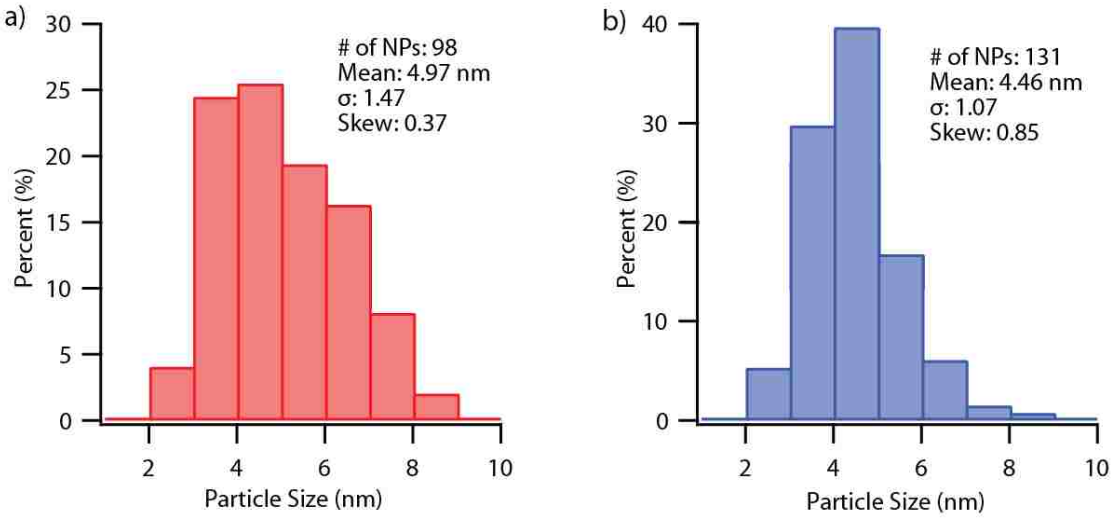

Figure 15: *Particle size distribution analysis of biomineralized ceria and ceria-zirconia nanoparticles after catalysis. Particle size distribution for (a) ceria and (b) ceria-zirconia nanoparticles (NPs) after use as a CO oxidation catalyst. A narrower distribution and smaller mean particle size is found for ceria-zirconia particles when compared with the pure ceria nanoparticles.*

Subsequent HAADF-STEM analysis of the biomineralized materials after use as a CO oxidation catalyst, Figure 13 and 14, demonstrates that both ceria and ceria-zirconia

particles maintain their fluorite crystal structure. Particle size distribution analysis (Figure 15) demonstrates some limited particle size growth after use as a catalyst. However, it is worth noting that a smaller increase in average particle size was found for the ceria-zirconia nanocrystals, confirming the expected increased thermal stability of ceria upon doping with zirconium[11]. This increase in average particle size is likely due to the relatively high temperature (500 ^{o}C) oxidative pre-treatment conducted prior to the catalytic function tests.

While this high temperature treatment removes some of the particle size advantage gained from low temperature synthesis, it is necessary to fully clean the catalyst surface in this laboratory scale catalysis demonstration. In application however, this higher temperature step can be performed *in-situ* during start-up of, for example, an automotive exhaust system where the catalyst will operate above 400^{o}C and be exposed to the varying pO_2 environment existing in the exhaust stream. This does not negate the green production advantages of direct biomineralization in terms of removing the need for corrosive precipitants or the multi-step processing typically necessary to generate such small ceria-zirconia particles. Finally, the biomineralized materials described here can be utilized without the need for this high temperature step in other applications, for instance as a biological antioxidant[93] or in chemical mechanical planarization[94], that do not operate at high temperatures. Further process development is required to be able to controllably tune the Ce:Zr ratio in the final mixed oxide product and to recycle or reuse the enzyme to enable nanoparticle production at commercially viable levels. One possible option is to explore surface immobilization of the engineered silicatein as previously demonstrated by Tremel *et al* for titania and zirconia mineralization[57].

2.3 Conclusion

In summary, the demonstrated retention of crystallinity, enhanced reducibility, better CO oxidation activity and enhanced thermal stability noted after zirconium incorporation into ceria, all serve as confirmation that *functional* mixed oxide ceria-zirconia nanocrystals can be successfully prepared by our direct biomineralization route. Both the pure ceria and ceria-zirconia nanoparticles produced via our rCeSi enzymatic route exhibit catalytic performance characteristics which make them competitive with counterpart materials made by more conventional chemical methods. In addition, the much smaller particle sizes that are readily accessible via direct biomineralization can already potentially offer surface area advantages for catalysis applications, and also allow fine tuning of the band gap by quantum confinement for optical applications. Most importantly, we have conclusively demonstrated that enzymatic direct biomineralization is a viable environmentally benign route for the controlled, low temperature, aqueous synthesis of catalytically active functional oxide nanomaterials.

2.4 Experimental

An *E. coli* codon-optimized, truncated form of silicatein from *S. domuncula* (NCBI accession number Q6YD92.1) containing amino acids 124-217 with mutation T10L and added C-terminal hexahistidine tag was sub-cloned into plasmid pET28a as a *BamHI-XhoI* fragment; this adds an N-terminal hexahistidine sequence present in pET28a. Unless otherwise stated, standard molecular biology techniques were used for sub-cloning and

sequences confirmed using standard DNA sequencing (Genscript). The resultant protein sequence is given below:-

```
        10         20         30         40         50         60
HHHHHHSSGL VPRGSHMASM TGGQQMGRGS GASYAFSAMG ALEGANALAK GNAVSLSEQN

        70         80         90        100        110        120
IIDCSIPYGN HGCHGGNMYD AFLYVIANEG VDQDSAYPFV GKQSSCNYNS KYKGTSMSGM

       130        140        150        160        170        180
VSIKSGSESD LQAAVSNVGP VSVAIDGANS AFRFYYSGVY DSSRCSSSSL NHAMVVTGYG

       190        200        210        220
SYNGKKYWLA KNSWGTNWGN SGYVMMARNK YNQLEHHHHH H
```

The modified silicatein was expressed from *E. coli* BL21(DE3) pLysS cells using isopropyl β-D-1-thiogalactopyranoside (IPTG) induction and the recombinant enzyme purified using immobilized metal affinity chromatography (IMAC) according to previously described methods[95,96]. A series of 3 x 3 h dialysis steps (Thermo Scientific Snakeskin™ 3.5kDa MWCO) against DI water was used to remove residual salts from IMAC purification before use.

Particle synthesis was induced by adding either (i) 2mM of cerium ammonium nitrate (Alfa Aesar), (ii) 2mM zirconium dinitrate oxide hydrate (Alfa Aesar), or (iii) a mixture of 1mM cerium ammonium nitrate and 1mM zirconium dinitrate oxide hydrate, to the purified protein solution (4μM silicatein). Samples were then incubated on an orbital shaker at room temperature. After 24 h the samples were centrifuged (18000 G) for 10 minutes and

the pellet re-suspended in 2mM nitric acid solution (Fisher Scientific). This washing process was repeated five times. As reported by Patil *et al.* the zeta potential of ceria nanoparticles increases at lower pH, enabling the formation of a stable nanoparticle sol in dilute nitric acid without the need for an additional capping agent[97]. The samples were centrifuged and dried under vacuum prior to catalytic testing and structural characterization, as necessary. Control samples, with only the rCeSi enzyme absent, underwent exactly the same synthesis procedure as the primary samples. No indication of any particle formation or change in color occurred within 48 hours.

Crystal structure and crystallite size were determined by X-ray diffraction measurements carried out at beamline 11-BM at the Advanced Photon Source, Argonne National Labs, USA. The diffraction spectra were collected at room temperature using incident X-rays having a wavelength of 0.41417 Å. Rietveld refinement was conducted on as-synthesized samples utilizing GSAS[65] with the EXPGUI interface[98]. Both structures were fit to the fluorite phase, space group $Fm\bar{3}m$, with lattice parameter and Lorentzian isotropic strain parameter, L_X, refined in GSAS profile 3 to determine the mean crystallite size.

High resolution X-ray Photoelectron Spectroscopy (XPS) analysis (Rutgers University, Thermo Scientific K-Alpha+ XPS) of the Ce(3d), 875-925eV, and Zr(3d), 176-196eV spectral windows were recorded using monochromatic Al K_α radiation at pass energies of 50 and 100 eV, respectively. A Ce^{4+} reference spectra, matching previously reported Ce^{4+} doublet and satellite peaks[99], was obtained from 15-30 nm ceria particles (Alfa Aesar). The reference Ce^{4+} spectra was fitted to the measured spectra for the biomineralized materials

and subtracted leaving only the peaks contributed by Ce^{3+}. The integrated areas of the $Ce^{3+}$and Ce^{4+} peaks were used to calculate the relative Ce^{3+} : Ce^{4+} ratios, using a method similar to that described in a previous report[87]. The spectra were calibrated to the C(1s) line of adventitious C at 284.8 eV. Prior to XPS analysis samples were annealed at 450°C in air.

The samples were analyzed in an aberration corrected JEOL ARM 200CF analytical electron microscope equipped with a JEOL Centurio SDD XEDS system operating at 200kV. Images were collected in both the high angle annular dark field scanning transmission electron microscopy (HAADF-STEM) mode and high resolution transmission electron microscopy (HR-TEM) modes. Samples were prepared by drop casting the aqueous sol onto carbon coated copper mesh TEM grids. Particle size distributions from more than 50 particles captured in HAADF-STEM images. The crystallography of individual nanoparticles were analyzed by measuring the interplanar spacings and angles from the Fast Fourier Transforms (FFTs) derived from the corresponding atomic resolution HAADF-STEM and HR-TEM lattice images. The lattice fringe spacings and inter-planar angles were also analyzed to determine the particle orientation and identity of the exposed profile view surface facets with the most likely 3D particle shapes proposed by comparison with literature reports[100].

X-ray energy-dispersive spectroscopy (XEDS) was conducted on the TEM specimens in STEM mode. When analyzing nanoparticles in the mixed oxide samples, the electron beam (*probe current:* 100pA) was rastered over small rectangular regions (*area:* 10-75 nm^2)

which enclosed groups of 3 or fewer particles. Collecting X-rays from small groups of particles rather than from single particles increases the signal-to-noise ratio and alleviates the amorphization and shrinkage of nanocrystals (each consisting of only a few hundred atoms) via knock-on damage during acquisition. Quantification of the XEDS spectra were carried out via the Thermo NORAN System SIX (NSS) software using the Cliff-Lorimer method[101].

The direct optical band gap of the nanoparticles in our sols was determined from ultraviolet-visible (UV-vis) absorbance spectra measured on a Shimadzu UV-2600 spectrometer operating at room temperature over the 200-550nm wavelength range[102]. Raman spectra were collected using a Witec alpha300RA (Knoxville, TN, USA) confocal Raman microscope with laser excitation of 532 nm. Measurements were performed with a spot size of ~5 um using a 20x objective. Spectra were collected using a UHTS 400NIR spectrometer with a grating of 2400 lines/mm.

The biomineralized ceria and ceria-zirconia materials were used as catalysts for carbon monoxide oxidation. Their performance was compared to that of a conventionally prepared commercial CeO_2 material (Alfa Aesar) comprised of 15-30 nm particles. In order to isolate the biomineralized ceria and ceria-zirconia particles from residual enzyme, the samples were heated in air at 500°C for 20 min (ramp rate 10°C/min). For catalytic testing purposes, the ceria and ceria-zirconia materials were dispersed (10 wt-%) onto 110 μm γ-phase alumina particles (Alfa Aesar) by mixing in ethanol. 70 mg of supported catalyst was packed into a 4 mm diameter quartz reactor tube and held in place with quartz wool plugs.

Prior to commencing catalysis measurements, pure oxygen was flowed through the reactor and the temperature was ramped at 10°C/min from 30 to 500°C. Gas analysis during catalytic reactions was performed using a Cirrus 2 benchtop atmospheric pressure gas analysis system (MKS instruments). Signals for m/z = 28, 32 and 44 were monitored and assigned to CO, O_2 and CO_2 respectively. The reaction gas consisted of 2% CO, 8% O_2 and 90% Ar and the total flow rate used was 37.5mL/min. The reactor temperature was ramped up at 10 °C min from 30 to 500°C. The procedure was repeated for each sample by cooling in pure oxygen from 500°C to room temperature and repeating the temperature ramp in the CO containing gas mixture.

3. Ambient Temperature Aqueous Synthesis of Ultrasmall Copper Doped Ceria Nanocrystals for the Water Gas Shift and Carbon Monoxide Oxidation Reactions

3.1 Introduction

Copper-cerium mixed oxide materials are of considerable interest in a variety of catalytic applications such as the water gas shift (WGS) and CO oxidation reactions[10,13-18]. Both of these reactions have important significance in the industrial and automotive sectors. WGS catalysts are used for hydrogen and ammonia production at the industrial scale, and are an important component in fuel processors for proton-exchange membrane fuel cells, preventing CO poisoning at the anode[8-10]. In automobiles and stationary combustion sources, CO oxidation catalysts are widely used to mitigate the environmental impact of CO emissions and are an essential part of three-way catalyst systems[103-105]. Copper-cerium mixed oxide catalysts show high activity for these reactions due to the favorable redox properties of ceria and the active site created by incorporating copper. Additionally, the relatively low cost and earth-abundance of the constituent elements makes synthesis of these materials economical and scalable. While high copper dopant concentration and small particle size are desirable for enhancing this catalytic activity, the elevated temperatures associated with most synthesis procedures leads to exsolution of the dopant as well as particle growth. These two factors limit the accessible copper doping concentration and as-synthesized particle size. In this work, we describe a new synthesis protocol for the direct aqueous phase synthesis of ultrasmall highly doped copper-ceria

nanocrystals and demonstrate their high activity towards the water gas shift and CO oxidation reactions.

There is general agreement in the literature that both copper and ceria play important roles in catalysis. While researchers agree on the importance of the redox capability of ceria through the Mars-van-Krevelen mechanism [36,37], which has been demonstrated in ceria doped with other transition metals[106-108], the precise nature of the Cu active site for both CO oxidation and the water gas shift reaction over $Cu_xCe_{1-x}O_{2-\delta}$ catalysts is still a matter for ongoing debate [13,14]. For example, Wang *et al* and Gammara *et al* propose that CuO_x clusters on the catalyst surface are critical for the selective oxidation of CO[13,15,16]. However, Liu and Flytzani-Stephanopoulos have presented contradictory evidence showing that Cu(I) ions incorporated within the ceria lattice are the active sites[17,109]. The oxidation state of the Cu species will be a strong function of reaction conditions, depending on whether one is dealing with total CO oxidation in excess O_2 or selective CO oxidation in the presence of H_2. Elias *et al* proposed that Cu can exist at a higher oxidation state under reaction conditions of high oxygen partial pressure and that the active sites are oxygen vacancies formed adjacent to Cu-substituted surface sites in the mixed oxide nanoparticles[14].

Despite this debate, there is some consensus that surface and near-surface enrichment of copper occurs under reaction conditions as the copper content in $Cu_xCe_{1-x}O_{2-\delta}$ increases, most likely leading to the formation of some CuO_x phase. However, there seems to be some clear advantages of fabricating these samples initially as intimately mixed solid solutions

rather than depositing Cu directly onto pre-formed CeO_2. For example, Gammara *et al* specifically compared the CO selective oxidation activity of co-precipitated $Cu_xCe_{1-x}O_{2-\delta}$ catalysts to the activity of supported CuO_x on CeO_2[16]. They noted that the high copper dispersion and initial presence of Cu in the co-precipitated catalyst leads to higher activity in the CO oxidation reaction.

In this study, we demonstrate a facile method for direct formation of copper cerium oxide nanocrystals at room temperature in aqueous solution. This approach exchanges the nitrate ligands present in a mixed cerium nitrate and copper nitrate precursor solution for the intermediate strength lactate ligand, to shift the precipitation pH from the "*hydroxo*" to the "*oxo*" regime. Inducing precipitation via addition of ammonium hydroxide then leads to direct formation of < 4 nm diameter $Cu_xCe_{1-x}O_{2-\delta}$ nanocrystals in the aqueous phase at room temperature. The Cu content can be tuned through the Cu nitrate/Ce nitrate ratios in the initial precursor solution to achieve as-synthesized Cu contents up to $x = 35$ in $Cu_xCe_{1-x}O_{2-\delta}$. We demonstrate that these two factors make our nanoparticles excellent candidate materials for CO oxidation and water gas shift reaction catalysts.

3.2 Experimental Methods:

3.2.1 Particle synthesis

We synthesized ceria based nanoparticles using a modified base precipitation method as shown schematically in Figure 16. 100mL of aqueous solution was prepared with 100mM $Ce(NO_3)_3$, 0-200mM $Cu(NO_3)_2$ and a DL-lactic acid concentration equal to the total solution nitrate concentration ($[CH_3CHCOOH] = [NO_3]$). While stirring (500 rpm),

nanoparticle growth was initiated by raising the pH to between 8.5 and 9 through the dropwise addition of 6% ammonium hydroxide solution. This pH was maintained for 2 h and the solution was allowed to stir overnight. After particle synthesis, excess lactic acid, nitric acid and ammonia were removed by dialysis using Thermo Snakeskin 3,500 kDa tubing against deionized water, which caused aggregation of the mixed oxide particles. The solid product was washed three times by centrifugation (10,000 RCF) and subsequent re-suspension in deionized water. The nanoparticles were finally re-dispersed and stored in dilute citric acid buffer (20mM, pH 5.5) until required for use.

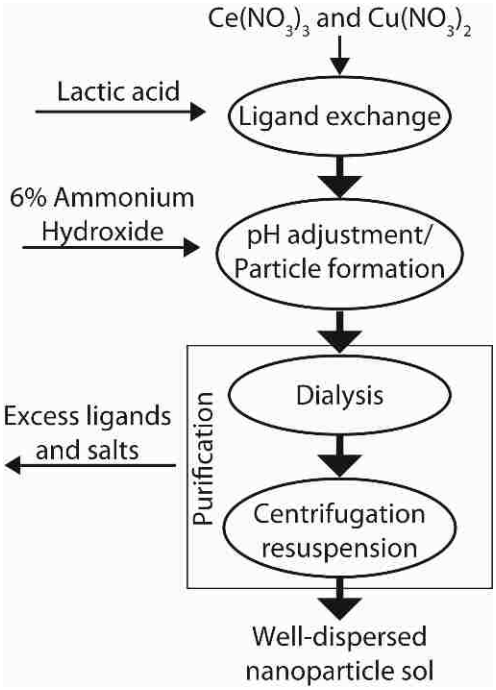

Figure 16: *Synthesis flow diagram for the synthesis of our $Cu_xCe_{1-x}O_{2-\delta}$ nanoparticle sols.*

3.2.2 Materials Characterization

Samples for scanning electron microscopy (SEM) and energy dispersive X-ray (XEDS) analysis were prepared by drying the nanoparticle sols at room temperature, under vacuum overnight and attaching the dried film to an Al sample stub using adhesive carbon tape.

The samples were examined in a Hitachi 4300SE SEM operating at an accelerating voltage of 20keV, which was equipped with an EDAX silicon drift detector. XEDS spectrum quantification was conducted using EDAX Genesis software employing appropriate atomic number (Z), absorption (A) and fluorescence (F) corrections[110].

Synchrotron X-ray powder diffraction patterns obtained at beamline 11-BM of the Advanced Photon Source at Argonne National Labs, were utilized to determine the crystal structure and mean crystallite size of the as synthesized material. Rietveld refinement of this data was performed using the GSAS package[65] with EXPGUI interface[98] and the peak shapes were fitted to the Lorentzian isotropic crystallite size, LX, strain broadening, LY, and Lorentzian anisotropic crystallite size broadening, ptec, parameters in GSAS Profile 3. The mean crystallite size was then derived from the calculated LX parameter.

The phase stability of the crystallites at elevated temperature was determined using an Anton Paar DHS1100 domed hot stage attachment to a PANalytical Empyrean X-ray diffractometer. The sample holder was heated from 50-750°C collecting spectra at 100°C intervals with a 15 min dwell time at each temperature. Spectra were collected over a 30-100° 2θ angular range.

Raman spectra were collected at room temperature using a Witec alpha300RA (Knoxville, TN, USA) confocal Raman microscope equipped with a 532 nm laser. The laser was focused to a ~5μm^2 spot on the dried $Cu_xCe_{1-x}O_{2-\delta}$ sample using a 20x objective lens.

Spectra were collected using a UHTS 400NIR spectrometer with a diffraction grating having 2400 lines/mm.

Samples for analysis by scanning transmission electron microscopy (STEM) were prepared by drop casting some diluted aqueous sol onto a carbon coated molybdenum mesh TEM grid (Electron Microscopy Sciences). The samples were analyzed in an aberration corrected JEOL ARM 200CF analytical electron microscope equipped with a JEOL Centurio XEDS system operating at 200kV. Images were collected in high angle annular dark field (HAADF)-STEM and high-resolution HR-TEM modes. Fast Fourier Transforms (FFTs) derived from the HAADF-STEM and HR-TEM images were used to measure interplanar spacing and angles.

As-synthesized and dried $Cu_xCe_{1-x}O_{2-\delta}$ samples and those annealed at 300^{o}C for 15 min in air were analyzed by X-ray photoelectron spectroscopy (XPS). The samples were attached to the sample holder with conductive carbon tape. XPS spectra were collected using a Scienta ESCA-300 system with an excitation energy of 1486.6eV (Al K_α). The operating pressure of the sample chamber is in the range of 10^{-8} Torr which may lead to a slight reduction of the sample materials. High resolution scans were collected from the Ce(3d), Cu(2p), O(1s) and C(1s) spectral regions, along with a lower resolution wide survey scan of the entire spectrum. All spectra were calibrated to the C(1s) line of adventitious carbon (284.8eV). The relative concentrations of Ce(III) and Ce(IV) were calculated semi-quantitatively by integrating the area under the peaks associated with Ce(III) (u^0, v^0, u', and v') and Ce(IV) (u, v, u'', v'', u''', and v''') following the method proposed by Zhang

et al [85], in which, peak centers were set and only peak intensity and width were left as free parameters for peak fitting. The peak width and integrated area values obtained were found to be in good agreement with those reported in prior literature[85,111-113].

3.2.3 Catalytic Testing

$CeO_{2-\delta}$ or $Ce_{1-x}Cu_xO_{2-\delta}$ nanoparticles were loaded onto 105-150 μm silica support particles (Sigma Aldrich) through incipient wetness impregnation from a washed solution of nanoparticles buffered in 20mM citric acid at pH 5.5. The vacuum dried supported catalyst was packed into a 4 mm inner diameter quartz reactor tube and held in place with quartz wool plugs. Prior to any catalytic tests being performed, the reactor temperature was ramped at 10 °C/min from 30 to 450 °C in flowing air to remove residual water and citrate capping ligands from the catalyst particles. TGA analysis showed removal of water and citrate capping ligands to occur at 100°C and 150-300°C respectively (Figure 17).

CO oxidation light-off curves were measured utilizing 500mg of the supported catalyst (1% $^{w}/_{w}$) in a gas mixture of 2% CO, 8% O_2 and 90% Ar at a total flow rate of 37.5mL/min. The reactor temperature was raised at 10°C/min from 30-450 °C. Gas analysis was performed using a Cirrus 2 benchtop quadrupole mass spectrometer (MKS instruments) at the reactor outlet monitoring for m/z = 28, 32 and 44 signals which were assigned to CO, O_2 and CO_2 respectively.

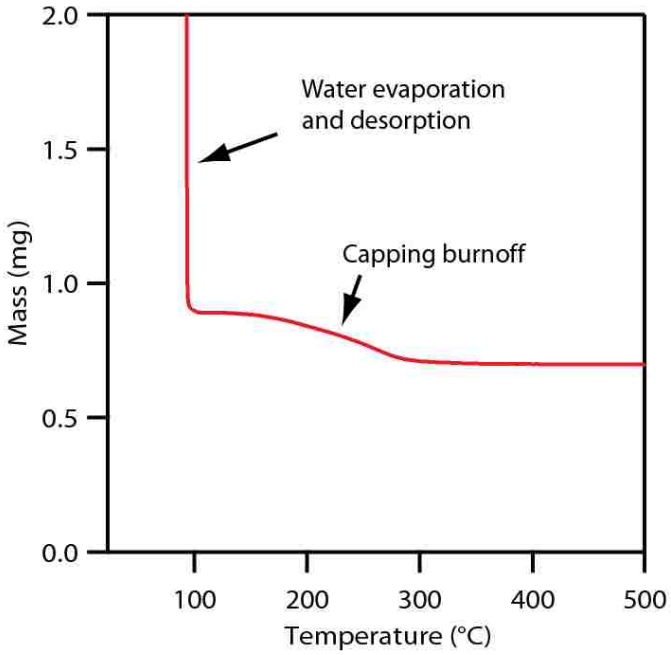

Figure 17: *Thermogravimetric analysis (TGA) of an aqueous sol of* $Cu_{0.15}Ce_{0.85}O_{2-\delta}$ *nanoparticles. TGA was used to determine the total solids content of a 40μL volume of nanoparticle sol. Moisture vaporization occur at temperatures around 100°C whereas citrate capping ligand decomposition occurs between 150°C and 300°C.*

Water gas shift reaction rate measurements were performed utilizing 500mg of supported catalyst (7.5% $^{w}/_{w}$) in a gas mixture of 1.5% CO, 1.5% H_2O, and 97% N_2 at various flow rates chosen to be between 25 and 100 mL/min. The inlet gas composition and flow rate were controlled by mass flow controllers and H_2O was added to the stream by flowing a portion of the N_2 gas through a sparger containing DI water at 25°C. The gas composition at the reactor outlet was analyzed by an in-line model 8610C gas chromatograph (SRI Instruments) equipped with thermal conductivity and flame ionization detector. Samples were heated to 450 °C and the conversion measured stepwise at decreasing temperature intervals of 25 °C. Calculations for activation energy used only data collected where conversion level was less than 15%. The measured rates were normalized to the BET

surface area of the catalysts as determined by N_2 adsorption measurements at -196 °C using a homemade instrument.

3.3 Results

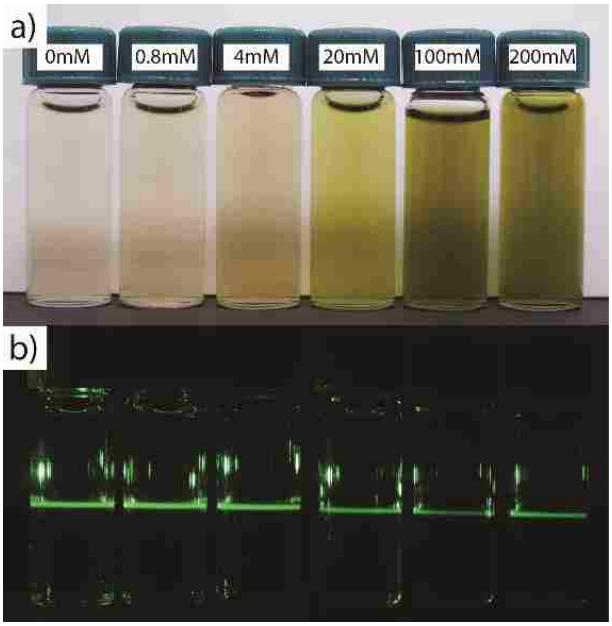

Figure 18: *Photograph of copper-doped ceria sols taken under a) natural light and b) green laser illumination. The copper nitrate content used during synthesis increases from 0mM to 200mM from left to right while the cerium nitrate concentration for each sample remained constant at 100mM. The color of the washed sol changes from clear to pale yellow to green with increasing copper content. The laser scattering demonstrates the presence of colloidal nanocrystals.*

Direct formation of the oxide is possible due to the intermediate bond strength of the lactic acid ligand with the cerium ion. Lactic acid bonds to cerium with a binding constant ($\log(K_1)$) of 2.756 allowing the pH to be adjusted to 8.5-9.0 before solid formation[114]. During particle synthesis, clear sols were formed after pH adjustment as shown in Figure 18a). Laser light scattering, which is indicative of colloidal sol formation, became visible within minutes accompanied by a change in color, which was dependent on the copper content. Sols with low nominal copper contents (*i.e.*, $x = 0$ to .01) transition from colorless to pale yellow whereas the samples with higher copper content (*i.e.*, $x = 0.05$ to 0.35)

transition from blue to deep green. Following synthesis, dialysis and washing, the nanoparticles were suspended in a dilute citric acid buffer solution (pH:5.5, <20mM) where they once again become clear with light scattering visible under laser illumination, Figure 18b. A plot quantifying the relative proportions of precipitated-to-unprecipitated metal precursor for each sample composition prepared is shown in Figure 19, as determined by inductively coupled plasma mass spectrometry of the dialysis products.

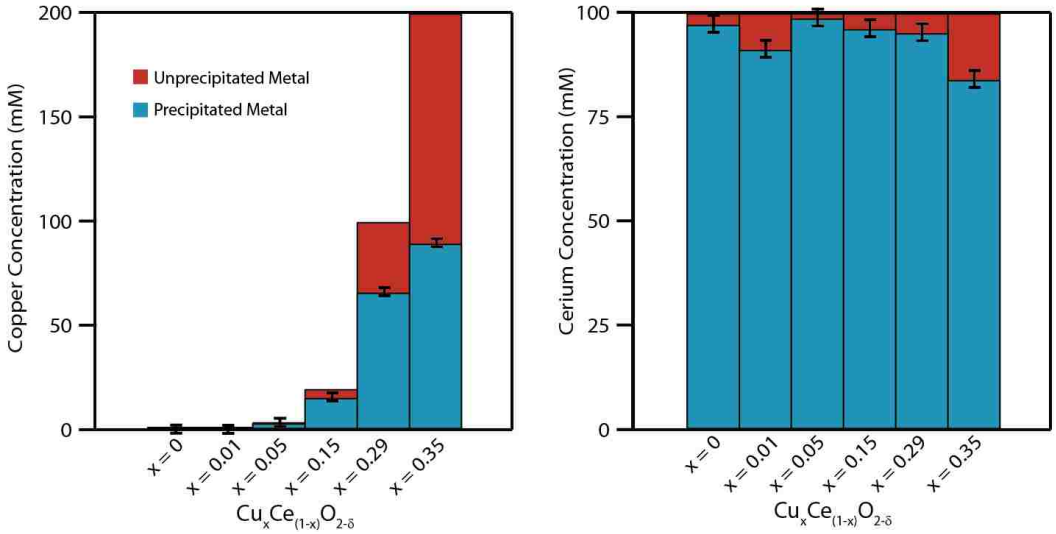

Figure 19: *Histogram showing ICP-MS analysis of the relative amount of Cu and Ce metal precursors ending up in the $Cu_xCe_{1-x}O_{2-\delta}$ precipitate versus the residual solvent. Samples after synthesis underwent dialysis to remove the remaining soluble metal precursors. The dialysis water was subsequently analyzed using ICP-MS to determine the concentration of remaining soluble metal precursors. It was found that as the nominal copper precursor concentrations tend toward x= 0.35 the majority of the copper precursor remains unprecipitated. The fraction of cerium precursor that gets incorporated into the precipitate remains above 90% for all samples except for $Cu_{0.35}Ce_{0.65}O_{2-\delta}$. The $Cu_{0.35}Ce_{0.65}O_{2-\delta}$ sample has the smallest particle sizes, and it is likely a small portion of precipitated oxide particles diffused across the dialysis membrane leading to higher concentrations of cerium in the dialysis water.*

Figure 20: *Photograph of a 100mM copper nitrate and 200mM lactic acid solution as pH increases. It should be noted that the solution remains clear throughout the transition from lactic acid bound cerium at low pH to ammonia bound cerium at high pH, with no solid cupric hydroxide formation in the intermediate pH range.*

In contrast to ceria precipitation, attempting to form pure cuprous oxide nanoparticles using a similar approach led to the generation of a clear Cu(II) complex when the ammonium hydroxide base was added (Figure 20). While the solution color intensity changed, there was no indication of precipitation or sol formation, suggesting a simple exchange of the complex ligand, from lactate to ammonia. Interestingly, this by-passes the formation of a solid cupric hydroxide precipitate that is expected to occur in the intermediate pH range in the absence of lactic acid[115] which supports the notion that the lactate ligand plays a stabilizing role in our synthesis procedure for $Ce_{1-x}Cu_xO_{2-\delta}$.

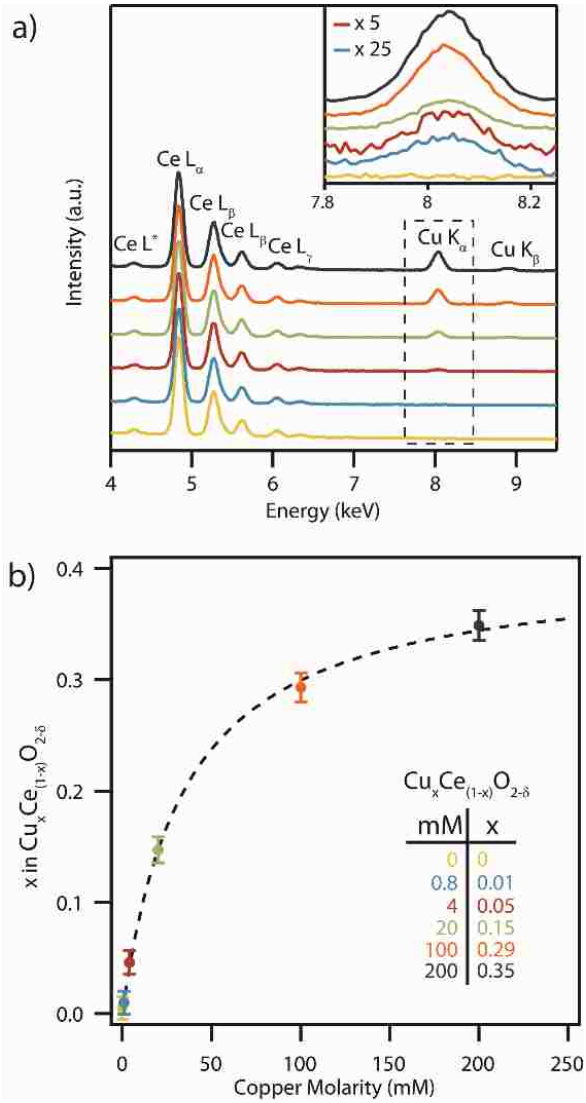

Figure 21: *a) SEM-XEDS spectra collected from copper-doped ceria samples prepared with varying concentrations of copper nitrate in solution during synthesis. The inset in a) shows a magnified view of the spectral range encompassing the Cu Kα peak (0.8mM and 4mM peaks multiplied by 25 and 5 times respectively). The color key for these spectra is inset in (b). b) Measured copper content, x, in $Cu_xCe_{1-x}O_{2-\delta}$ nanoparticles, derived from analysis of the XEDS data presented in a), as a function of Cu nitrate precursor concentration. The Ce nitrate precursor concentration was held constant at 100mM in all samples.*

SEM-XEDS spectra were collected from dialyzed, washed and dried precipitated films of the as-synthesized nanocrystals, Figure 21a. All of the samples showed a strong series of Ce L-series peaks. The intensity of the Cu Kα and Kβ peaks increased with increasing

concentration of Cu nitrate in the synthesis solution. The corresponding copper concentrations in the set of $Cu_xCe_{1-x}O_{2-\delta}$ samples were determined on a metals basis using the standardless ZAF correction method[116], Figure 21b. The highest measured copper concentration corresponded to $x = 0.35$ which is amongst the highest reported to date in $Cu_xCe_{1-x}O_{2-\delta}$ [117-119]. While XEDS and ICP-MS (Figure 19) shows that most of the copper is incorporated into the $Cu_xCe_{1-x}O_{2-\delta}$ precipitate for low concentration samples (*i.e.,* x = 0.01, 0.05), the production of $Cu_xCe_{1-x}O_{2-\delta}$ particles with Cu higher concentrations required the copper precursor to be in excess, and thus much of the precursor remains unprecipitated. It should also be noted that if we calculate the expected composition of the nanocrystals utilizing the ratios of precipitated materials determined from the ICP-MS data, we arrive at Cu contents greater than those experimentally determined by XEDS. This is due to the precipitation of a separate copper hydroxide phase that is removed from the particles after synthesis by a triplicate washing procedure. The apparent saturation of Cu content at $x = 0.35$ in the nanoparticles for higher Cu nitrate precursor concentrations is consistent with prior research that suggested a maximum Cu content of $x = \sim 0.30$ is sustainable within single phase $Ce_{1-x}Cu_xO_{2-\delta}$[120].

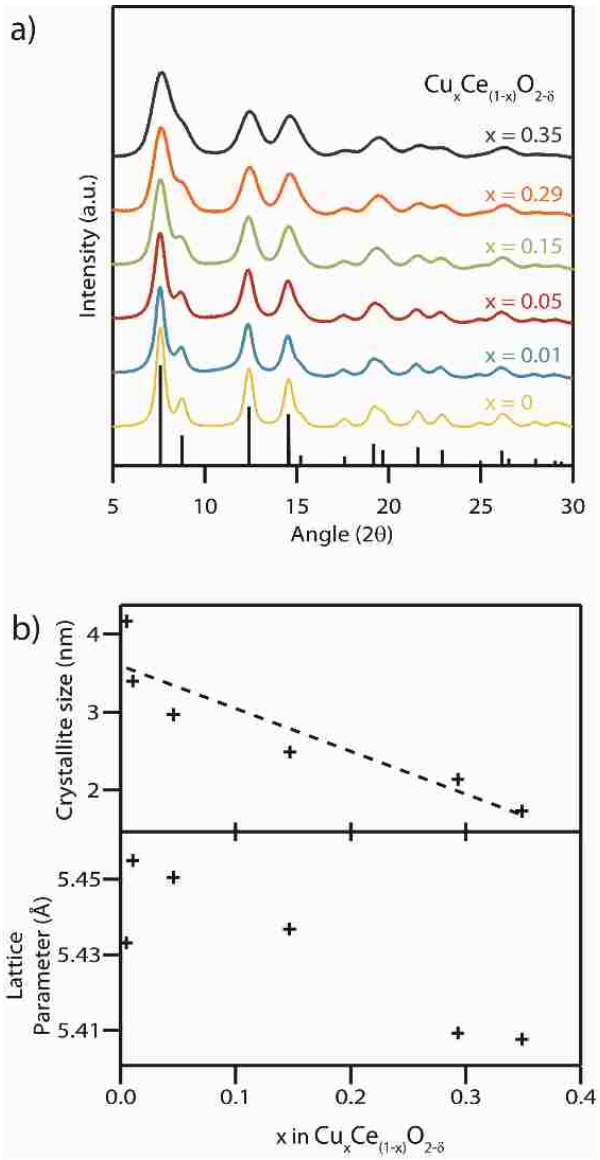

Figure 22: *a) Synchrotron X-ray diffraction patterns of the as-synthesized $Cu_xCe_{1-x}O_{2-\delta}$ materials with varying Cu content showing good agreement with the CeO_2 fluorite structure, space group $Fm\bar{3}m$, (ICSD collection code 156250, reference peak positions shown). The progressive broadening of the peaks with increasing copper content is indicative of decreasing crystallite mean size. The trend line is provided as a guide to the eye. b) Lattice parameter and crystallite size measurements derived from Rietveld refinement of the XRD patterns presented in a).*

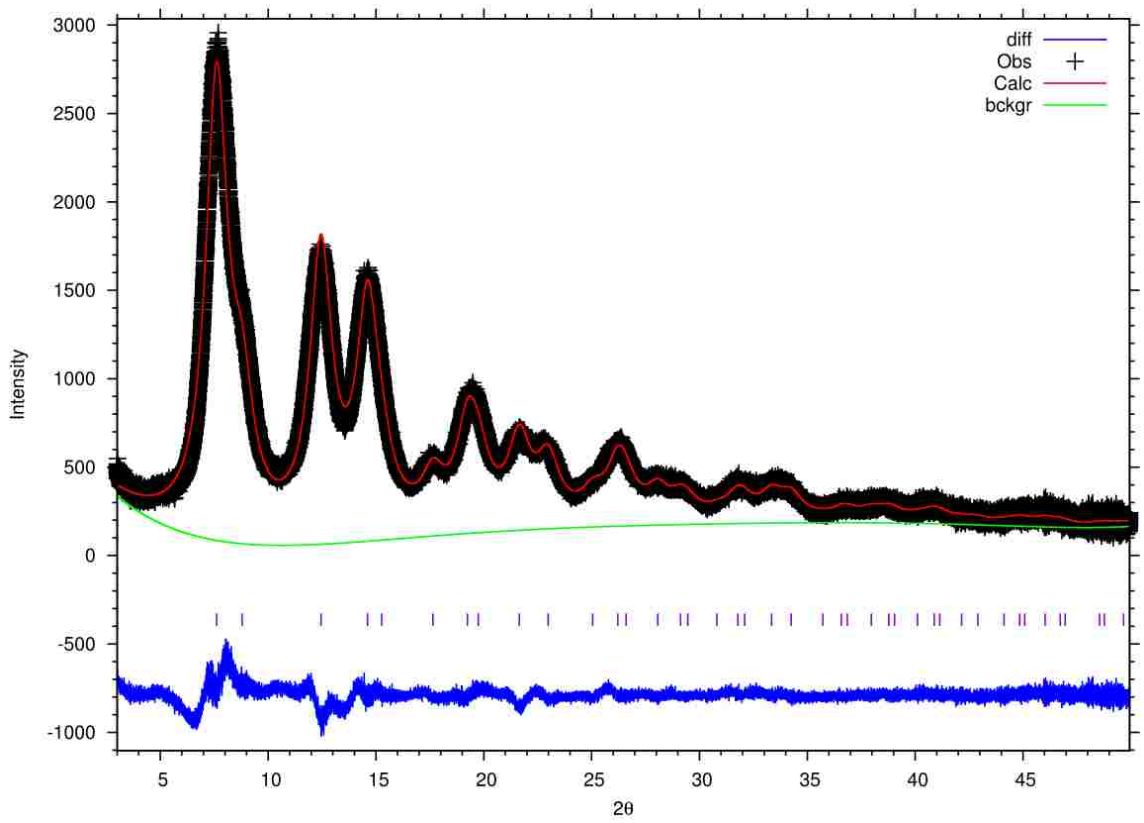

Figure 23: *XRD spectra and GSAS fitting of the $Cu_{0.35}Ce_{0.65}O_{2-d}$ sample showing only fluorite-type structure cerium oxide peaks.*

Rietveld refinement of synchrotron X-ray diffraction (XRD) patterns obtained from the as-synthesized material with varying Cu contents confirmed the presence of a single phase with the fluorite structure, space group $Fm\bar{3}m$, in each sample (Figure 22). There was no evidence of secondary CuO or Cu_2O phases in any of the samples, Figure 23. The average crystallite size was found to decrease with increasing Cu content, with the 1.7 nm mean size measured for the x = 0.35 sample being amongst the smallest ever reported for either pure or doped ceria nanocrystals[10,121,122]. The ability to access such small crystallite sizes is a direct consequence of the absence of any calcination step in our synthesis procedure, which removes the opportunity for sintering and growth processes to occur. Decreasing crystallite size typically leads to an increase in the lattice parameter in pure CeO_2

particles[33]. In the present case, this is counterbalanced by the expected decrease in lattice parameter upon increasing the concentration of the lower radius Cu(II) ions replacing the larger Ce(III) and Ce(IV) ions $Cu_xCe_{1-x}O_{2-\delta}$[123]. The Shannon ionic radii of Cu(II), Ce(III) and Ce(IV) in an octahedral coordination environment are 0.73, 1.01 and 0.87 Å respectively[34]. In our systematic set of materials, the influence of copper concentration on lattice parameter is dominant which leads to a progressive decrease in lattice parameter except for the x = 0-0.01 Cu concentration range where the influence of size dominates and leads to a larger lattice parameter. Note that this result was confirmed by repeating the synthesis procedure and XRD measurements several times.

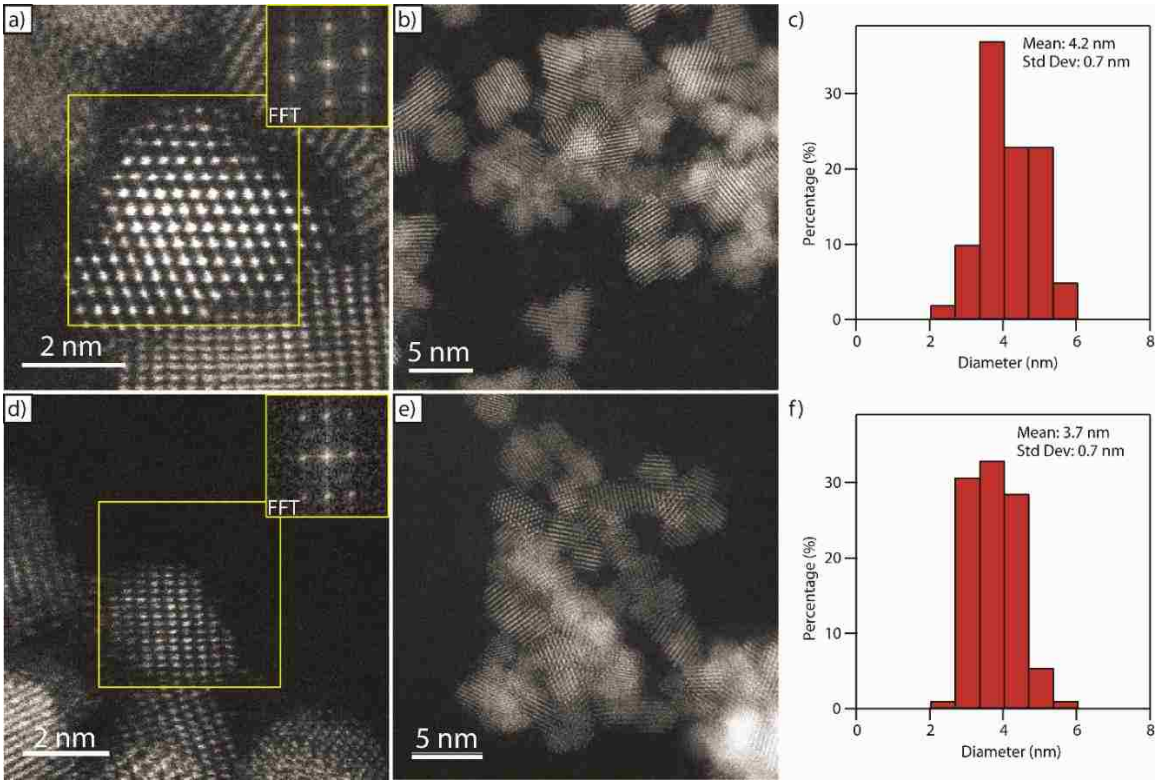

Figure 24: *Representative HAADF-STEM images of a,b)* $CeO_{2-\delta}$ *and d,e)* $Cu_{0.05}Ce_{0.95}O_{2-\delta}$ *nanoparticles showing high crystallinity. The inset FFTs in a) and d), obtained from the areas in the yellow boxes, are consistent with the* $[1\bar{1}0]$ *and the* $[11\bar{2}]$ *projections of fluorite structured ceria respectively. Surface-equivalent spherical diameter particle size distributions of the pure ceria and copper-doped ceria nanoparticles are shown in c) and f) respectively.*

Figure 24(a,b) show representative HAADF-STEM micrographs of the pure ceria material confirming the crystalline and nanoparticulate nature of the as-synthesized material. The measured interplanar spacing and angles derived from the corresponding fast Fourier transform (FFT, inset in Figure 24a) match well with those expected for the $[1\bar{1}0]$ projection on the CeO_2 fluorite structure, Figure 25. The ceria particles have a relatively narrow size distribution with an average particle size of 4.2 ± 0.7nm (measured

as a surface-equivalent spherical diameter (Figure 24c) which matches well with the value derived from the XRD data (Figure 22).

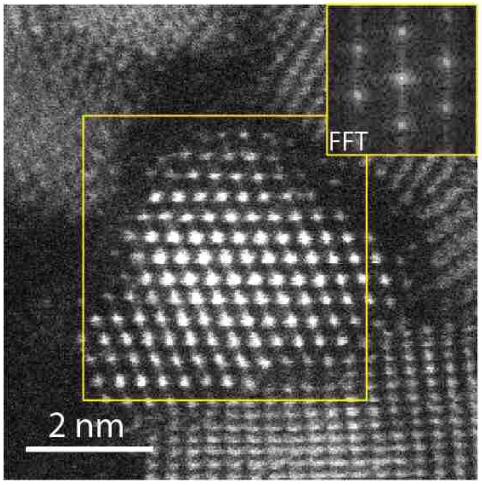

Nanocrystal identification as flourite type $CeO_{2-\delta}$		
	Measurement	Matching
Plane 1	d=2.84 Å	2.71 (002)
Plane 2	d=3.23 Å	3.12 (111)
Plane 3	d=3.20 Å	3.12 ($1\bar{1}1$)
<1, 2>	56.8°	54.74°
<1, 3>	54.8°	54.74°
<2, 3>	68.4°	70.53°

Figure 25: *HAADF-STEM image of pure ceria and corresponding interplanar spacing and angles. Inset is an FFT obtained from the particle in the yellow box. Interplanar spacings and angles match those expected of the [$\bar{1}$10] projection of fluorite structured ceria.*

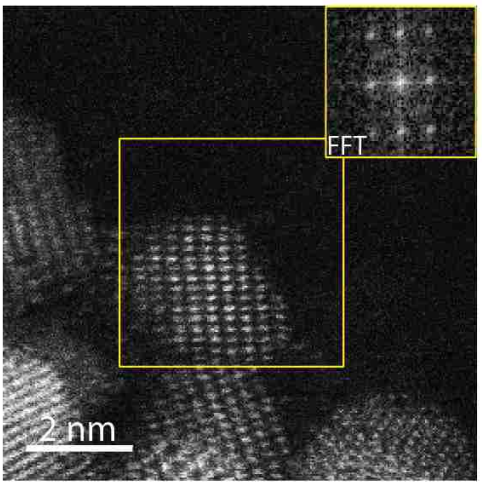

Nanocrystal identification as flourite type $Cu_{0.05}Ce_{0.95}O_{2-\delta}$		
	Measurement	Matching
Plane 1	d=1.69 Å	1.6$\bar{3}$ (311)
Plane 2	d=1.92 Å	1.9$\bar{1}$ (220)
Plane 3	d=3.23 Å	3.12 (111)
<1, 2>	29.3°	31.48°
<1, 3>	63.3°	58.52°
<2, 3>	87.5°	90°

Figure 26: *HAADF-STEM image of $Cu_{0.05}Ce_{0.95}O_{2-\delta}$ and corresponding interplanar spacing and angles. Inset is an FFT obtained from the particle in the yellow box. Interplanar spacings and angles match that expected of the* [1$\bar{1}$2] *projection of fluorite structured ceria.*

Figure 24(d,e,f) show the corresponding HAADF-STEM micrographs and particle size distribution of the nanocrystals in the $Cu_{0.05}Ce_{0.95}O_{2-\delta}$ sample. As with the pure ceria material, the interplanar spacing and angles derived from the FFT inset in Figure 24d match well with the fluorite structure; this time viewed along the $[11\bar{2}]$ projection, Figure 26. The particle size distribution is narrow (Figure 24f), with a mean particle size of 3.7 ± 0.7 nm, which again matches well with the corresponding value derived from XRD analysis (Figure 22).

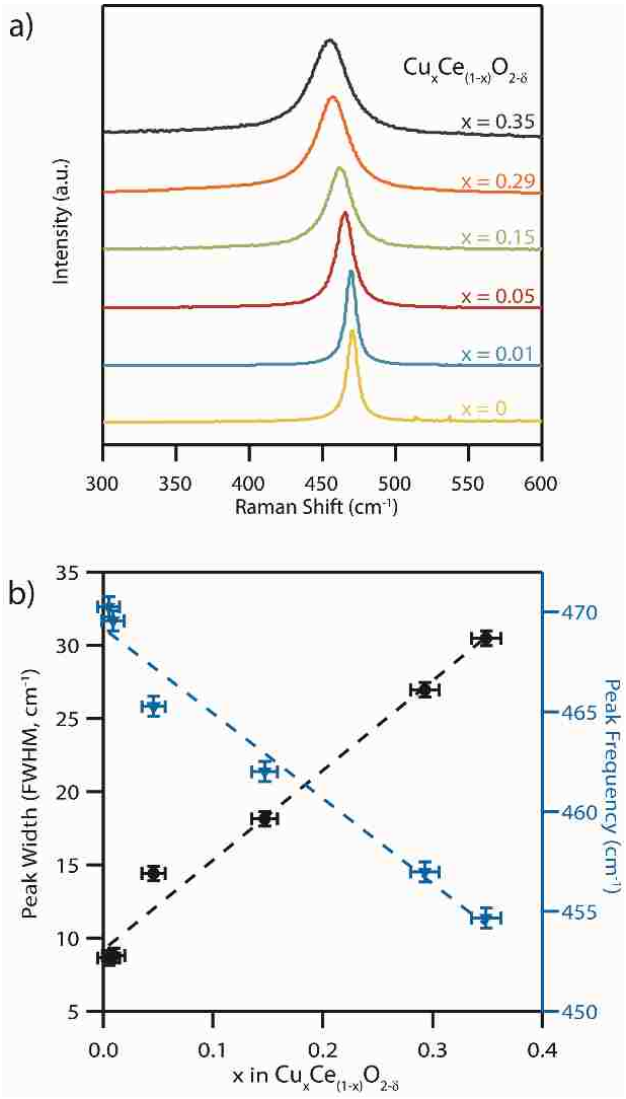

Figure 27: *a) Raman spectra of the as-synthesized CeO_2 and copper-doped ceria samples showing peak broadening and a progressive shift to lower frequencies in the Ce-O band peak position as the copper content increases, which is consistent with the formation of a solid solution. b) Corresponding Ce-O Raman peak full-width-at-half-maximum (FWHM) and peak frequency as a function of copper content extracted from the data in a).*

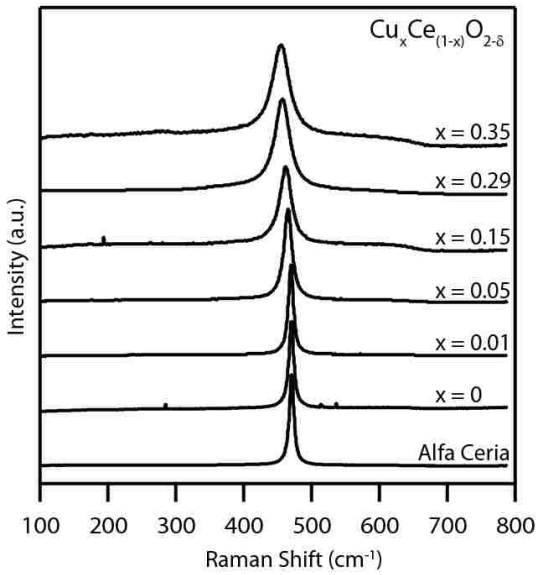

Figure 28: *Raman spectra of the set copper-doped ceria samples and a pure (Alfa Aesar) ceria reference material showing a wide Raman shift range. Only the F_{2g} bands of cerium oxide are present. There are no copper oxide peaks indicating the absence of any secondary phase [CuO(295, 345, 630 cm^{-1}); Cu_2O(150, 230, 640 cm^{-1})]. A wide band centered at ~600 cm^{-1} is present is all samples and can be attributed to the presence of oxygen vacancies*[13].

Raman spectra acquired from the pure $CeO_{2-\delta}$ material exhibit a single peak centered at 470 nm^{-1}, Figure 27a, which is consistent with the reported position of the single allowed Raman mode of ceria with the fluorite structure [31,124]. This F_{2g} symmetry peak has previously been assigned to an oxygen anion breathing mode around the central cation[31]. This peak was observed to both broaden and systematically shift to lower wavenumber in an approximately linear fashion as the Cu content in the series of $Cu_xCe_{1-x}O_{2-\delta}$ samples increases, Figure 27b. The F_{2g} peak position decreased to 455 cm^{-1} for the x = 0.35 Cu-doped sample. This is trend is fully consistent with the formation of a solid solution of copper within ceria [13,31]. Peak broadening with increasing Cu content can be attributed to increased disorder due to the random distribution of both copper cations and oxygen vacancies in the material and their effect on neighboring Ce-O bond strength[16]. A portion of this increased peak width can also be attributed to the observed decrease in crystallite

size that typically increases the peak width in nanomaterials[125]. Additionally, from wide-range Raman spectra (Figure 28) no Cu_2O (150, 230, and 640 cm^{-1}) or CuO (290, 340, and 625 cm^{-1}) peaks were detected, further confirming that a single phase solid solution material forms upon doping CeO_2 with Cu. Also visible in the wide range Raman spectra is a wide band peak at ~600 cm^{-1}, which can be attributed to oxygen vacancies in the samples[13].

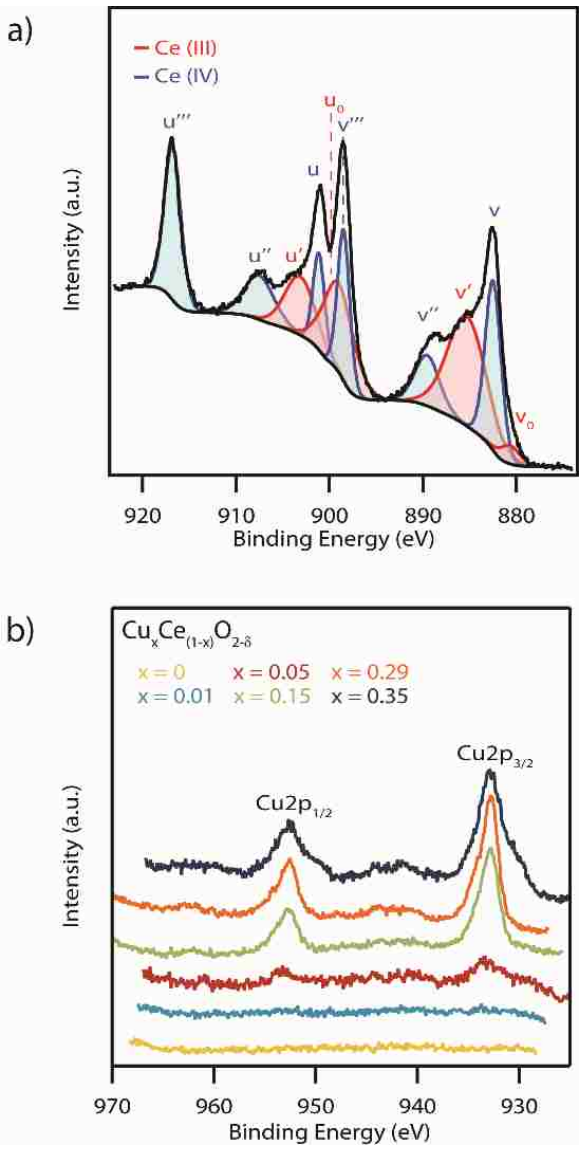

Figure 29: *(a) X-ray photoelectron spectra of the 29 mol % copper doped ceria sample in the Ce(3d) region. Peaks attributed to both Ce(III) (red) and Ce(IV) (blue) can be seen which can only be accommodated if there are also oxygen vacancies present in the crystal lattice. (b) XPS spectra of the Cu(2p) region of the entire set of $Cu_xCe_{1-x}O_{2-\delta}$ samples with x varying from 0 to 0.35. The absence of strong Cu(II) satellites at 942 and 962 eV indicates that copper exists in the Cu(I) oxidation state.*

In order to further confirm the formation of a solid solution and the potential impact on catalytic activity, the influence of Cu doping on the Ce oxidation state and oxygen vacancy concentration in the as-synthesized materials was investigated by XPS. While this is

typically described as a surface characterization technique, we can in this case consider the spectra to be representative of the bulk due to the mean nanoparticle diameter being smaller than the XPS penetration depth. A representative spectrum of the Ce(3d) region for the $Cu_{0.29}Ce_{0.71}O_{2-\delta}$ sample is shown in Figure 29a with the spectra for all of the other materials in the series presented in Figure 30. Cerium was found to exist in both the Ce(III) and Ce(IV) oxidation states which is typical of nanoscale ceria[33]. The concentration of Ce(III) was determined semi-quantitatively by taking a ratio of the area under the curve of fitted Ce(III) peaks over that of the summed areas of the Ce(III) and Ce(IV) peaks, following a method previously described by Zhang *et al* [85]. This analysis indicates a trend of decreasing Ce(III) concentration with increasing copper content, varying from 56% in pure $CeO_{2-\delta}$ to 48% in the highest doped $Cu_{0.35}Ce_{0.65}O_{2-\delta}$ sample, Table 1. The Ce(III) concentration values obtained were found to be in good agreement with those reported in prior literature[33,86].

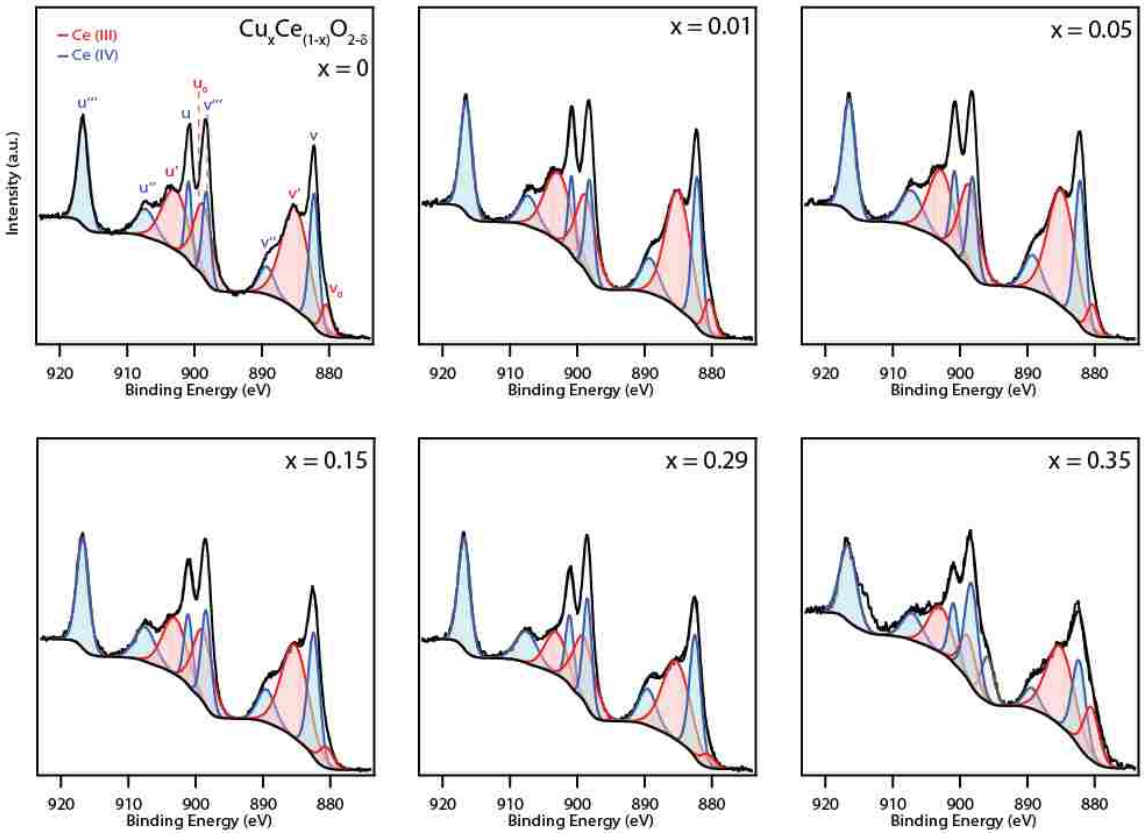

Figure 30: *XPS spectra of as synthesized copper-doped ceria samples. The Ce(III)/Ce(IV) ratio was found to be slightly dependent on the copper concentration. Peaks attributable to Ce(III) and Ce(IV) are represented in red and blue respectively.*

Figure 29b shows the XPS spectra of the Cu(2p) region for the complete set of $Cu_xCe_{1-x}O_{2-\delta}$ samples. The x = 0.05, 0.15, 0.29, and 0.35 samples showed clear $Cu2p_{1/2}$ and $Cu2p_{3/2}$ peaks with only weak satellite peaks at ~945 eV, indicative of primarily a Cu(I) oxidation state with only small quantities of Cu(II)[126]. The minor amount of Cu(II) may be indicative of a small amount of a segregated Cu-containing secondary phase in these highest Cu-content materials[127]. As expected, no Cu(2p) peaks were observed in the x = 0 nanocrystals. Similarly, no Cu(2p) peaks were observed in the x = 0.01 sample due to the detection limit constraints of the XPS instrument.

Table 1: *Physical Characteristics of the various $Cu_xCe_{1-x}O_{2-\delta}$ materials*

Nominal copper concentration[a] (mM)	Actual copper concentration[b] (metals basis)	Mean crystallite size [c] (nm)	Lattice parameter[c] (Å)	Ce(III) concentration[d] (%)	Raman Peak (cm^{-1})
0	-	4.2	5.433	56%	470.3
0.8	0.01	3.4	5.455	56%	469.6
4	0.05	3.0	5.450	54%	465.3
20	0.15	2.5	5.437	50%	462.0
100	0.29	2.1	5.409	46%	457.0
200	0.35	1.7	5.408	48%	454.7

[a] Concentration of $Cu(NO_3)_2$ used during synthesis.
[b] Determined from XEDS measurements.
[c] Calculated from Reitveld refinement of synchrotron powder XRD data. Standard deviations in the lattice parameter, obtained from GSAS, are an order of magnitude lower than the lowest reported digit.
[d] Determined using XPS data from the Ce(3d) energy range, following the method proposed by Zhang *et al* [85].

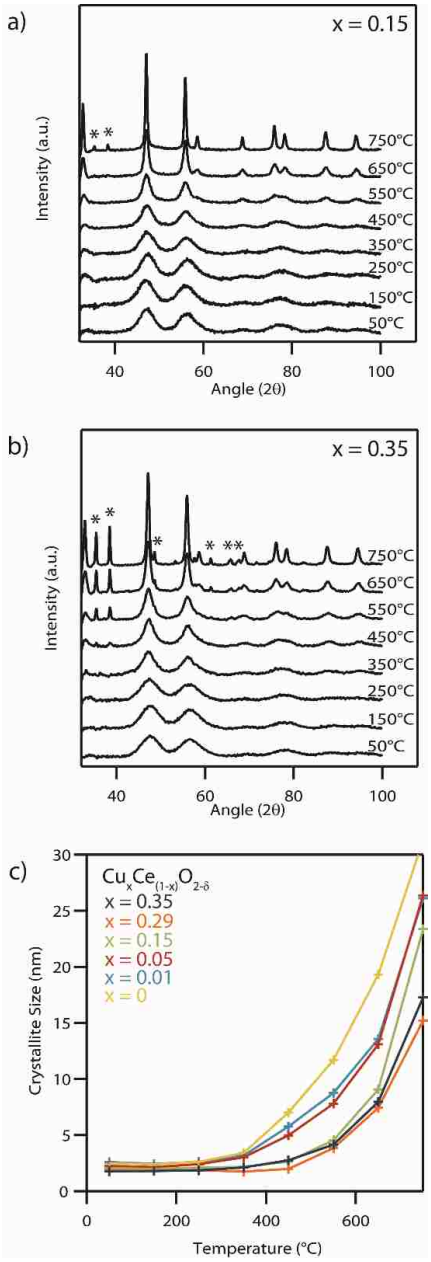

Figure 31: *Series of X-ray diffraction spectra of a) x = 0.15 and b) x = 0.35 copper-doped $Cu_xCe_{1-x}O_{2-\delta}$ samples after being subjected to calcination at increasing temperatures in air for a 15 min dwell time. As the calcination temperature increases, the diffraction peaks get narrower due to crystal growth effects. In the samples with the highest copper-doping levels distinct copper oxide (labelled *) peaks begin to appear after calcination at elevated temperatures. c) Plot showing the mean ceria crystallite size as a function of calcination temperature. High copper concentrations seem to hinder sintering of the fluorite-type $Cu_xCe_{1-x}O_{2-\delta}$ phase.*

A key benefit of the lactic acid mediated synthesis approach employed in this study is the direct formation of the mixed $Cu_xCe_{1-x}O_{2-\delta}$ nanocrystals at room temperature, removing

the need for a high temperature calcination step that can lead to unwanted crystallite growth and possible exsolution of Cu from the solid solution. However, many catalytic applications of these materials will typically require that they be exposed to elevated temperatures. High temperature XRD patterns obtained upon heating the $Cu_xCe_{1-x}O_{2-\delta}$ samples in air were analyzed to determine the extent of crystal growth and the stability of the mixed oxide phase as a function of calcination temperature. The Scherrer equation was used to estimate the average crystallite size from the (220) and (311) reflections of CeO_2 using a shape factor of 0.9[30,128].

Figure 31(a,b) shows XRD of the systematic set of spectra for the $Cu_{0.15}Ce_{0.85}O_{2-\delta}$ and $Cu_{0.35}Ce_{0.65}O_{2-\delta}$ materials at a series of calcination temperatures beginning at 50°C and increasing up to 750°C at 100°C intervals with a 15 min dwell time at temperature before taking any measurements. A distinct narrowing of the peaks characteristic of the fluorite structure was noted for each sample with increasing temperature due to crystallite growth at these elevated temperatures (Figure 31c). The secondary set of XRD peaks at 750°C and 450°C respectively for $Cu_{0.15}Ce_{0.85}O_{2-\delta}$ and $Cu_{0.35}Ce_{0.65}O_{2-\delta}$ can be indexed to CuO, indicating an upper thermal limit of phase stability for these solid solutions. No CuO phase formation was observed for any of the other lower Cu content nanocrystals up to the maximum measurement temperature of 750°C. The source of this CuO phase can be attributed either to the exsolution of Cu from these higher Cu-content $Cu_xCe_{1-x}O_{2-\delta}$ nanocrystals, or the subsequent crystallization of an amorphous Cu phase formed during synthesis. Such an amorphous Cu phase cannot be detected by XRD or by STEM, although

we note the possible indication of the existence of some amorphous material in the as- XPS data acquired from the as-synthesized $Cu_{0.29}Ce_{0.81}O_{2-\delta}$ sample, (Figure 29).

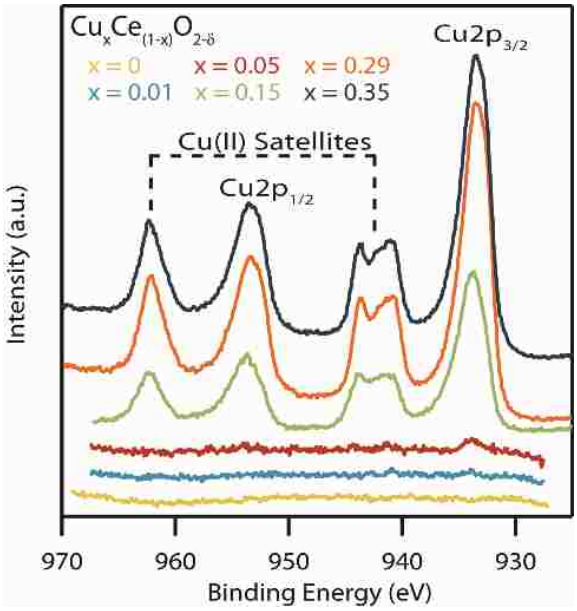

Figure 32: *XPS spectra of the Cu(2p) region of the various copper-doped ceria samples after calcination at 300 °C for 15 mins. The presence of strong satellite peaks indicate a shift in Cu from the Cu(I) to the Cu(II) oxidation state after heat treatment.*

Figure 32 shows the XPS spectra of the Cu(2p) region for the series of copper-doped ceria samples that have been calcined at 300°C for 15 min. Samples with low copper concentrations show no significant Cu(2p) peaks. The heat-treated variants of the more highly doped samples show characteristic $Cu2p_{1/2}$ and $Cu2p_{3/2}$ peaks along with the Cu(II) satellites indicating the copper in the sample has changed oxidation state from Cu(I) to Cu(II). Likewise, there is an average shift in binding energy of +0.6 eV in the $Cu2p_{3/2}$ peaks after heat treatment, further indicating this switch in oxidation state[126]. Such a change in oxidation state has been reported previously by Sciré *et al* in copper-doped ceria

materials that were heated from 200 to 400°C[129]. Taken together with our data this indicates that the transition from Cu(I) to Cu(II) occurs somewhere between 200-300°C.

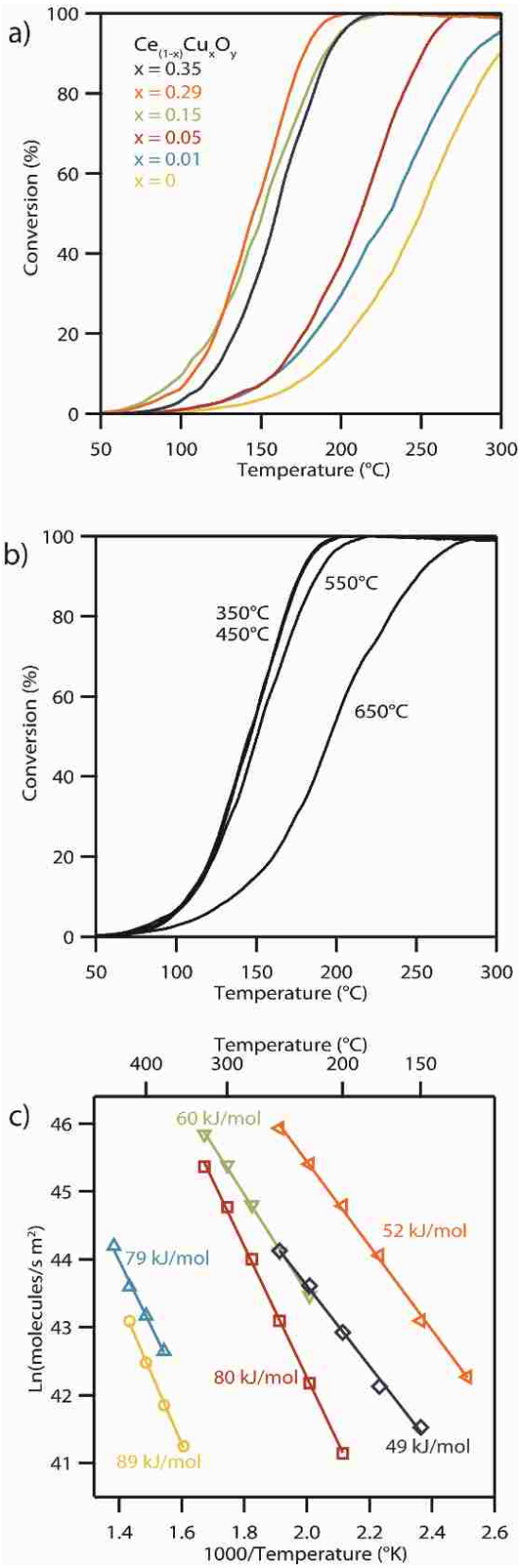
a)
$Ce_{(1-x)}Cu_xO_y$
x = 0.35
x = 0.29
x = 0.15
x = 0.05
x = 0.01
x = 0
Conversion (%)
Temperature (°C)
b)
350°C
450°C
550°C
650°C
Conversion (%)
Temperature (°C)
c)
Temperature (°C)
60 kJ/mol
52 kJ/mol
79 kJ/mol
80 kJ/mol
49 kJ/mol
89 kJ/mol
Ln(molecules/s m²)
1000/Temperature (°K)

Figure 33: *a) CO conversion data as a function of temperature for the set of $Cu_xCe_{1-x}O_{2-\delta}$ materials (with x varying from 0 to 0.35) supported on silica. The temperature required for 50% conversion ranges from 262°C for $CeO_{2-\delta}$ to 145°C for $Cu_{0.29}Ce_{0.71}O_{2-\delta}$. b) The CO conversion curves for $Cu_{0.29}Ce_{0.71}O_{2-\delta}$ materials that had been subjected to calcination at varying temperatures. It should be noted that a significant reduction in catalytic activity is only apparent for samples calcined above 650°C. (Note: the 350°C and 450°C curves strongly overlap). c) Arrhenius plot analyses of water gas shift rates for the set of $Cu_xCe_{1-x}O_{2-\delta}$ materials (with x varying from 0 to 0.35) supported on silica for a $CO:H_2O:N_2$ gas mixture of 1.5:1.5:97 % at 1 atm.*

The CO oxidation reaction is typically used as an important benchmark for the catalytic activity of these Cu-doped ceria materials[130]. The CO oxidation light-off curves shown in Figure 33a exhibit the anticipated trend of lower light-off temperature, indicative of higher catalytic activity, with increasing copper content in the $Cu_xCe_{1-x}O_{2-\delta}$ structure. The exception to this trend occurs for the highest copper content material, *i.e.*, $Cu_{0.35}Ce_{0.65}O_{2-\delta}$, which shows a slight decrease in the copper light-off temperature relative to the $Cu_{0.29}Ce_{0.71}O_{2-\delta}$ sample, most likely due to the formation of some CuO secondary phase as indicated by our high temperature XRD experiments. The $Cu_{0.29}Ce_{0.71}O_{2-\delta}$ catalyst showed 50% conversion at 145°C with a gas hour space velocity of 25,000 h^{-1}. Hence the performance of our $Cu_{0.29}Ce_{0.71}O_{2-\delta}$ material is in-line with other literature reports on copper-doped ceria CO oxidation catalysts[10,131].

CO oxidation light-off experiments were repeated for the $Cu_{0.29}Ce_{0.71}O_{2-\delta}$ sample following calcination at a series of elevated temperatures. The $Cu_{0.29}Ce_{0.71}O_{2-\delta}$ sample was chosen for this experiment because it was the highest performing catalyst of the series and because it had been shown, through high temperature XRD, to develop CuO crystals after calcination at elevated temperatures. The CO oxidation performance of this particular catalyst was unaffected at calcination temperatures below 550°C; however, a significant

decrease in the activity was observed after calcination at 650°C which was attributable to copper exsolution (Figure 33b).

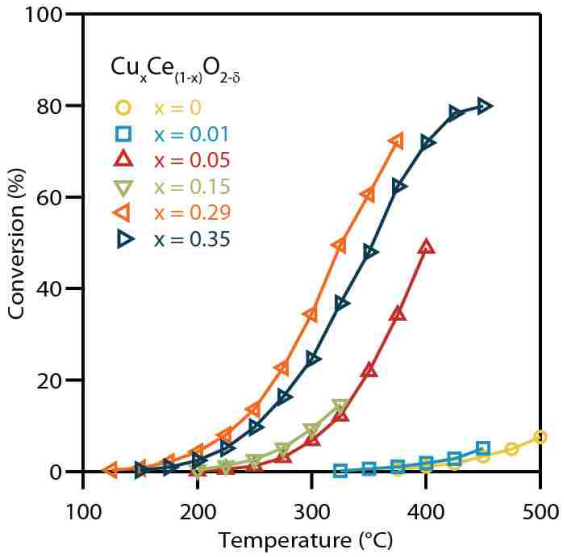

Figure 34: *Water gas shift conversion as a function of reaction temperature for ceria materials with varying copper concentrations. In general, increasing the Cu content gradually improves the catalytic performance with the exception of the* $Cu_{0.35}Ce_{0.65}O_{2-\delta}$ *sample which we believe underwent some phase separation under the reaction environment.*

An Arrhenius plot of the reaction rate for the water gas shift reaction using the set of $Cu_xCe_{1-x}O_{2-\delta}$ samples is shown in Figure 33c. These reaction rates have been normalized using the surface areas determined from BET isotherm analysis (Table 2). As with the CO oxidation light-off data, the catalytic activity generally increases with increasing Cu content in the $Cu_xCe_{1-x}O_{2-\delta}$ material, as shown in Figure 34. The measured decrease in activation energy was accompanied by an increase in overall reaction rate as *x* increased in $Cu_xCe_{1-x}O_{2-\delta}$ up to x=0.29. Again, as with the CO light-off data, the overall rate of the *x* = 0.35 decreases when compared with the *x* = 0.29 sample, however the activation energy slightly decreases. This further indicates a decrease in accessibility of more active solid solution sites caused by exsolution of copper. Representative STEM micrographs of the

$Cu_{0.35}Ce_{0.65}O_{2-\delta}/SiO_2$ materials before and after the WGS oxidation reaction are shown in Figure 35. The images clearly show some evidence of crystallite growth in the post-reaction sample. Although, the presence of any thin amorphous layers of exsoluted copper rich material could not be detected in either sample, >10nm segregated copper phase was detected in the post reaction sample. The measured activation energies and reaction rates for the WGS reaction are also competitive with previous literature reports for copper-doped ceria catalysts[132].

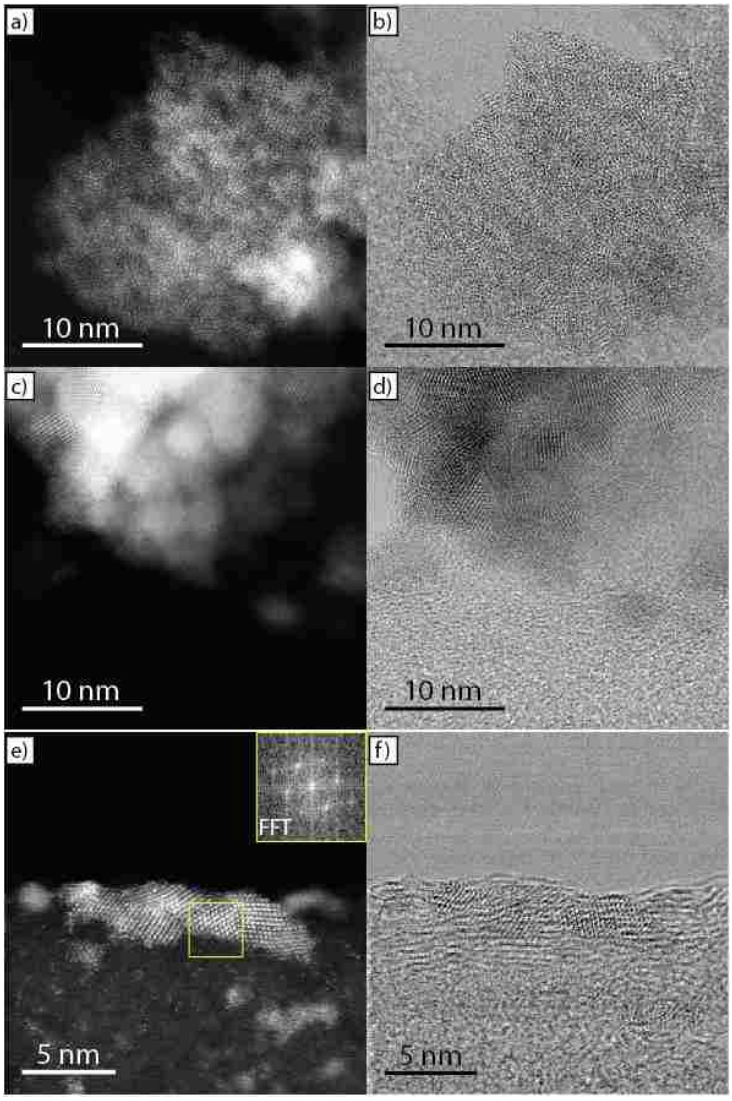

Figure 35: *Representative HAADF-STEM micrographs of supported $Cu_{0.35}Ce_{0.65}O_{2-\delta}$ particles before and after pretreatment and WGS catalysis. Before exposure to*

pretreatment and WGS reaction conditions the a) HAADF and b) bright-field micrographs show a high density of nanocrystalline $Cu_{0.35}Ce_{0.65}O_{2-\delta}$ domains supported on the SiO_2. After exposure to pretreatment and reaction conditions c) HAADF and d) bright-field micrographs showed the used catalyst to have slightly larger $Cu_{0.35}Ce_{0.65}O_{2-\delta}$ crystallite sizes. Also present in the post-reaction sample were some occasional secondary copper-rich phases, as shown in e) HAADF and f) bright field micrographs. The lattice spacing and interplanar angles of these latter phases could not be matched to the fluorite structure and were much more consistent with those expected for the cubic Cu_2O or monoclinic CuO structures.

Table 2: *Catalytic Performance Characteristics of the various $Cu_xCe_{1-x}O_{2-\delta}$ materials supported on SiO_2*

Sample[a]	**Surface area[b] ($m^2\ g^{-1}$)**	**CO light-off temperature[c] (°C)**	**WGS activation energy[d] (kJ mol^{-1})**
$CeO_{2-\delta}$	155	262	89.0 ± 1.2
$Cu_{0.01}Ce_{0.99}O_{2-\delta}$	190	250	78.8 ± 2.4
$Cu_{0.05}Ce_{0.95}O_{2-\delta}$	145	212	80.0 ± 1.1
$Cu_{0.15}Ce_{0.85}O_{2-\delta}$	110	151	59.9 ± 0.6
$Cu_{0.29}Ce_{0.71}O_{2-\delta}$	90	145	51.6 ± 0.5
$Cu_{0.35}Ce_{0.65}O_{2-\delta}$	90	159	49.2 ± 0.9

[a] Copper concentration calculated from XEDS measurements.
[b] Calculated from N_2 adsorption isotherms.
[c] Temperature for 50% CO conversion.
[d] Calculated by Arrhenius equation from data collected at under 15% conversion.

3.4 Discussion

The nature of the precipitate formed upon raising the pH of a metal nitrate solution is qualitatively described in a classic paper by Livage *et al*[25]. As the pH increases, the interaction of the metal with the aqueous solution transitions from "*aquo*" (M-OH_2) to "*hydroxo*" (M-OH) and finally to "*oxo*" (M-O), with the precise pH required for a 'transition' being a function of the identity of the transition metal itself and the associated ligands in solution. In a typical ceria nanoparticle synthesis procedure, the pH of the precursor solution is raised to the point where it induces precipitation of insoluble cerium hydroxide nanocrystals by shifting into the '*hydroxo*' region of Livage's construction. The

hydroxide precipitate can then subsequently be transformed into cerium oxide by a suitable calcination treatment.

Our results demonstrate that the addition of lactic acid into the precursor solution strongly influences the ligand associated with the cerium ion in solution. The binding constants ($\log(K_1)$) of nitrate and lactate ligands to Ce(III) are 0.21 and 2.756[114] respectively, indicating a substantially stronger association of the lactic acid species to the Ce(III) cation[38]. We suggest that the direct formation of the oxide in our lactic acid mediated synthesis route is due to the stronger ligand association that stabilizes the cation in solution as the pH increases upon the addition of ammonium hydroxide. This shifts the point of precipitation out of the '*hydroxo*' region into the '*oxo*' region in the Livage diagram.

The exact nature of the catalytically active site in $Cu_xCe_{1-x}O_{2-\delta}$ is still a matter of debate, however, there is general consensus that formation of a mixed Ce-Cu-O solid solution is critical to creating highly active sites. While it can be challenging to prove the formation of a true solid solution at very low dopant concentrations, all of the experimental evidence collected points to the formation of an intimately mixed $Cu_xCe_{1-x}O_{2-\delta}$ phase for x=0.01 to 0.35 in our as-synthesized materials. The lattice parameter determined from the synchrotron XRD data (Figure 22) shows a progressive decrease in lattice parameter of the fluorite-type with increasing Cu content as would be expected from a Vegard's law type relationship due to the smaller cationic radius of Cu. Furthermore, no secondary phases were observed in the as-synthesized materials prepared via our lactic acid mediated synthesis.

Further evidence for Cu-Ce-O solid solution formation comes from the approximately linear decrease in Ce-O breathing mode Raman frequency with increasing dopant level *x* in the $Cu_xCe_{1-x}O_{2-\delta}$ phase (Figure 27). This is the result of the shift in phonon frequencies due to the decrease in lattice parameter, often referred to as the Grünier shift in Raman frequency[31]. The concurrent broadening of the Raman peaks with increasing doping level is also indicative of solid solution formation, where such broadening is due to substitutional disorder on the cation sublattice upon Cu-doping leading to a distribution of cation-anion breathing frequencies[31]. While the trends in lattice parameter, crystallite size and Raman spectra strongly indicate the formation of mixed oxide solid solution nanocrystals, we cannot fully rule out that some surface segregated amorphous copper-rich material exists in the as-synthesized $Cu_xCe_{1-x}O_{2-\delta}$ materials with x= 0.29 and 0.35.

We also note that the Ce(III) to Ce(IV) ratio in our materials shows a systematic trend of increasing Ce(IV) content with increasing Cu(I) doping level in $Cu_xCe_{1-x}O_{2-\delta,}$ suggesting some charge compensation occurs to stabilize the oxygen within the lattice upon doping. Finally, we found no evidence of secondary Cu-O phases in any of our HAADF-STEM imaging experiments on the as-synthesized materials (Figure 24). When combined with the measured catalytic efficacy of the materials, all of the experimental evidence strongly supports the conclusion that the lactic acid mediated synthesis route forms solid solution $Cu_xCe_{1-x}O_{2-\delta}$ nanoparticles.

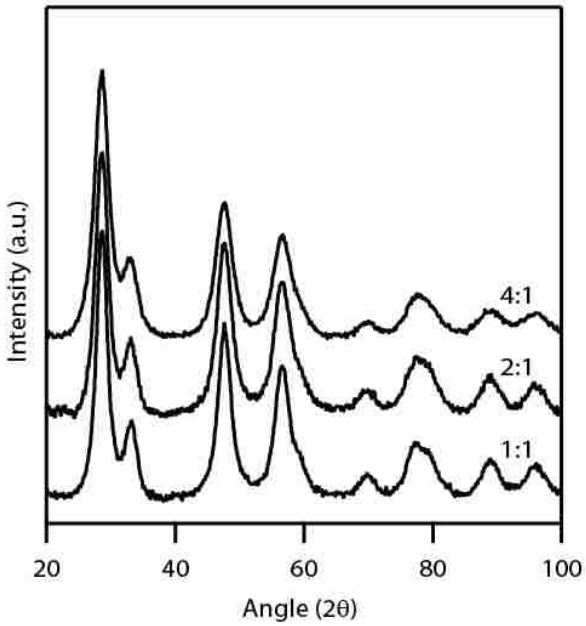

Figure 36: *XRD spectra of pure ceria nanoparticles produced with varying lactic acid concentrations during synthesis. Lactic acid was added to a 100mM $Ce(NO_3)_3$ solution in a 1:1, 2:1, and 4:1 ratio in this sample set. The use of higher concentrations of lactic acid was found to lead to smaller mean crystallite sizes. The mean crystallite sizes measured from XRD spectra using the Scherrer equation were 3.7 nm, 3.4 nm and 2.9 nm for the 1:1, 2:1, and 4:1 lactic acid : cerium nitrate concentrations respectively.*

The nominal Cu content chosen during synthesis also has a strong influence on the resulting nanocrystal size, evidenced, for example, by the 29% decrease in crystallite size upon doping with only 5% Cu into the ceria nanocrystals. The only significant differences during the synthesis of these two materials relative to that of pure CeO_2 is (i) the addition of 4mM copper nitrate and (ii) a 5% increase in lactic acid concentration to maintain the lactic acid : cation ratio. Analysis of mean particle size as a function of lactic acid concentration used (Figure 36) demonstrates that the influence of this process parameter is negligible. The mean crystallite size however shows a near linear relationship with the amount of copper in solid solution (Figure 22) and there are two possible reasons for this effect. As shown in Figure 20, rather than leading to precipitation of a cuprous oxide,

addition of ammonium hydroxide to a precursor solution containing only copper nitrate stimulates the formation of a complex between the Cu(II) and ammonium ion. Such a strong ligand-cation interaction may retard particle growth when Cu is included as the ammonium covers the surface of the growing particle. Alternatively, this Cu-complex may serve to nucleate particle formation, leading to rapid formation of a large number of small nuclei. Further work with alternative cationic dopant species, such as Ni, Fe, or Co, is required to fully understand the effect of dopant identity upon nanocrystal nucleation and growth using our lactic acid mediated synthesis method.

The $Cu_{0.35}Ce_{0.65}O_{2-\delta}$ material is comprised of particles with a mean size of 1.7 nm as determined by XRD, which is amongst the smallest ever reported for Cu doped-ceria material[10,121,122]. The ability to form such small crystallites is most likely due to the direct formation of the oxide during the low temperature precipitation stage, removing the need for a calcination step at an elevated temperature, thus avoiding unnecessary sintering. The materials display high surface areas due to their ultra-small crystallite sizes, up to 190 m^2/g for the $Cu_{0.01}Ce_{0.99}O_{2-\delta}$ sample, Table 2. There is an increase in surface area in the x=0 to 0.01 copper concentration range due to a decrease in crystallite size from 4.2 to 3.4 nm respectively. The subsequent decrease in surface area at higher values of x may be attributed to an increased propensity for sintering of the higher Cu-content nanocrystals upon sample pre-treatment as evidenced by the narrowing of the XRD peak widths in Figure 31.

While our experimental evidence points to the as-synthesized products being Cu-Ce-O solid solutions, these materials, particularly with the higher Cu dopant levels, become unstable at high temperature. XRD indicates phase separation upon calcination at ~750°C for lightly doped $Cu_{0.15}Ce_{0.85}O_{2-\delta}$ formulation, whereas the second phase appeared more readily at ~450°C for the higher doped $Cu_{0.35}Ce_{0.65}O_{2-\delta}$ material (Figure 31). This indicates why high Cu dopant levels may be difficult to achieve using more traditional synthesis routes where an elevated temperature calcination step is required.

The XRD calcination series study also suggests slower ceria crystallite growth in samples containing higher copper concentrations, although this may be partly due to exsolution of the Cu to form secondary CuO_x, leading to a loss of material from the parent $Cu_xCe_{1-x}O_{2-\delta,}$ nanoparticles.

The influence of copper doping level on the catalytic activity of $Cu_xCe_{1-x}O_{2-\delta,}$ is clearly observable for the both water-gas-shift and CO oxidation reactions (Figure 33 and 34). For the water gas shift reaction, the overall reaction rate increases with increasing Cu loading up to x = 0.29 the $Cu_{0.29}Ce_{0.71}O_{2-\delta}$ sample, but then decreases for the $Cu_{0.35}Ce_{0.65}O_{2-\delta}$ composition. However, it should be noted that these materials were calcined at 450°C prior to these catalytic tests, which is the temperature at which phase segregation of CuO_x occurs from $Cu_{0.35}Ce_{0.65}O_{2-\delta}$, implying that the decrease in reaction rate is associated with this bulk phase segregation. This concept is reinforced by analyzing CO oxidation light-off curves for the $Cu_{0.29}Ce_{0.71}O_{2-\delta}$ material with intermediate sintering steps of increasing temperature, Figure 33b. The CO light-off temperature is stable until a calcination temperature of 650°C

is reached, at which point the subsequent light-off temperature then increases. This again corresponds to the temperature at which the formation of a distinct CuO_x second phase is observed in the XRD pattern for $Cu_{0.29}Ce_{0.71}O_{2-\delta}$. This effect has been noted in a previous CO oxidation study using ceria doped with high concentrations of copper[133]. It has also been shown that under certain conditions, copper has a tendency to segregate to the surface of nanoparticles when doped into ceria[14]. Higher concentrations of copper on the particle surface will most likely lessen the accessibility to ceria, which is essential to provide oxygen for the reaction.

3.5 Conclusions

The facile lactic acid mediated approach for synthesizing Cu-doped ceria nanoparticles described here demonstrates the potential of using base precipitation as a synthesis route for controllably preparing nanoscale mixed oxide materials. By utilizing an intermediate binding strength ligand, intimately mixed $Cu_{1-x}Ce_xO_{2-\delta}$ solid solution crystals can be formed directly at room temperature in aqueous solution with high dopant concentrations and crystallite sizes as low as 1.7 nm. The synthesis method outlined uses low cost, easily accessible precursors and can be easily be implemented in any chemistry lab or scaled-up for industrial production. Our synthesized particles also show competitive catalytic activity for the water gas shift and CO oxidation reactions when compared to more conventionally prepared counterpart materials that have been described in the literature.

4. Investigation of Catalyst Deactivation and the Role of Supported Gallium Oxide Nanocrystals in the Ethane Dehydrogenation Reaction.

4.1 Introduction

Dehydrogenation reactions have a significant role in the chemical industry, turning relatively low cost inert alkane molecules into more reactive and valuable olefins. With the recent rise in natural gas reserves, low molecular weight alkane feed stocks are more readily available. In the dehydrogenation reaction, the equilibrium only begins to shift towards olefin formation at high temperatures, at these high temperatures coke readily forms on the catalyst. Coke build up is a significant factor in the deactivation of dehydrogenation catalysts. Recent studies have investigated the use of oxidative dehydrogenation for the formation of olefins[134-137]. Oxidative dehydrogenation has advantages such as coke burnoff and exothermic reactions limiting the need for external heating, however there are many disadvantages such as reduced selectivity, H_2 consumption, and side reactions.

Gallium oxide materials have recently been researched as catalyst materials for dehydrogenation reactions for the formation of olefins and hydrogen[138-141]. As well as being an active catalyst, gallium has also been shown to aid in the suppression of coke in platinum catalyst systems[138,142]. It has been shown that the catalytic properties of gallium oxide materials are often strongly linked to the structure and composition of the support material[138,143-145]. Xu et al has studied the effects of Ga-TiO_2 and Ga-Al_2O_3 on both propane dehydrogenation and oxidative dehydrogenation[144]. Their work found that Al_2O_3 support for Ga leads to higher dehydrogenation reaction rate in the absence of CO_2 in stream however TiO_2 supports lead to higher rates when CO_2 is present as a mild oxidant.

Because the interaction of Ga with the support is important to the overall properties of the catalyst, the maximization of Ga-support interaction is essential. Incipient wetness impregnation of oxide nanoparticles onto oxide support is a great way to maximize oxide-oxide interactions while limiting unfavorable structure formation because the high surface area of the support can be maintained. It has been shown that, coprecipitation methods often lead to large crystals of single oxide phased materials which often do not have the same catalytic properties of an oxide-on-oxide material[146]. Incipient wetness impregnation of a precursor molecule followed by a calcination step can lead to serious reduction of the high surface area of the support through high temperature sintering.

The present study investigates dehydrogenation catalysis using gallium oxide nanoparticles formed through a ligand assisted sol-gel synthesis, which has previously been shown to produce nanocrystalline cerium oxide[147]. Due to the low temperature of synthesis, the oxide particles produced have small crystallites. These particles are ideal for maximizing contact with a support material in a support promoted catalyst system. Gallium oxide nanoparticles are studied as an active catalyst and as a component in a Pt-Ga-Al_2O_3 catalyst system. We demonstrate how gallium oxide nanocrystals are active catalysts, reduce coking when used with an alumina support, and how gallium oxide nanocrystals have a complementary effect when used in conjunction with platinum catalysts.

4.2 Experimental Methods

4.2.1 Particle Synthesis

As shown in Figure 37 gallium based nanoparticles were synthesized in a modified sol-gel procedure, which has previously been shown to produce nanoscale cerium oxide particles[147]. In a typical preparation, 100mL of aqueous solution of 100mM gallium nitrate and 300mM lactic acid is mixed and placed on a stir plate. To the rapidly stirring solution 6% ammonium hydroxide is added dropwise until the solution pH reached 8.5. This pH is maintained for a 2 hour period using ammonium hydroxide as needed. After 2 hours the particle solution is allowed to stir overnight.

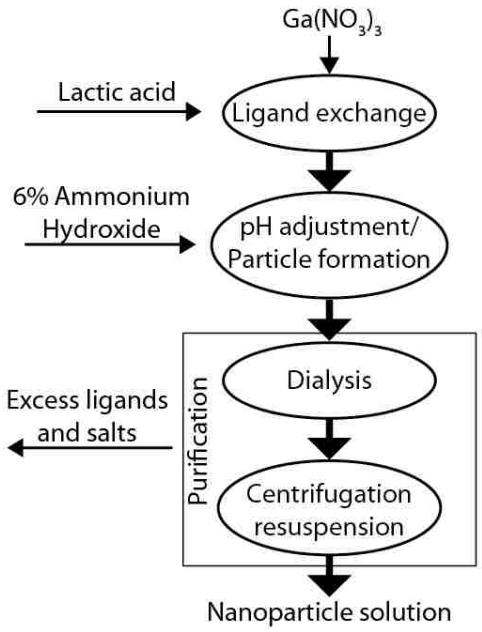

Figure 37: *Synthesis flow diagram for gallium oxide nanocrystals*

The particle solution is then cleaned through 4 dialysis steps using Thermo Snakeskin dialysis tubing (3500kDa) against deionized water for at least 3 hours per step. Dialysis results in the aggregation of the particles. After dialysis, the solution is centrifuged and

the pellet is suspended in deionized water. This centrifuge/resuspension process is repeated a total of 3 times. After the final resuspension the solution may be placed in a sonication bath to aid in dispersion of the particles.

4.2.2 Materials Characterization

Dried powder samples were characterized with Powder X-Ray Diffraction (PXRD) using a PANalytical Empyrean X-ray diffractometer. Spectra were collected over a 10-90° 2θ angular range using Cu Kα radiation. Samples for high angle annular dark field scanning electron microscopy (HAADF-STEM) analysis were prepared by drop casting diluted particle solutions on nickel mesh TEM grids with a holey carbon layer (Electron Microscopy Sciences). Micrographs were collected using a JEOL ARM 200CF analytical microscope equipped with a JEOL Centurio XEDS System operating at 200kV. Interplanar spacing and angles were calculated using Fast Fourier Transforms (FFT) derived from STEM micrographs. Using the 2D area of gallium oxide particles measured from STEM micrographs, a spherical equivalent particle size distribution was calculated.

4.2.3 Catalytic Testing

Supported platinum/gallium oxide samples were prepared through incipient wetness impregnation of the washed nanoparticle solution onto 35-45um alumina (Infrmat, Manchester, CT) and 100-150um titania (Alfa Aesar) supports. Active catalyst was loaded on the support at 1% mass loading, as determined through TGA analysis of the washed particle solution. Catalyst samples were loaded into a 7mm inner diameter quartz tube,

and held in place with quartz wool. The supported catalyst materials was treated at 400°C in flowing N_2 prior to catalytic testing.

Ethane dehydrogenation catalytic testing was completed at 500°C in a gas mixture of 2.5% ethane balance N_2 with a total flow rate of 50 ml min^{-1}. Hydrogen, ethane, ethylene, methane, and CO2 concentrations were measured using a Model 8610C GC (SRI Instruments) equipped with a Thermal Conductivity Detector (TCD) and a Flame Ionization Detector (FID). Gasses were separated using a 6" HayeSep D chromatography column. Ethylene conversion ($X_{Ethylene}$) was determined by Equation 3, where $\boldsymbol{n}$ is the outlet molar concentration

$$\boldsymbol{X_{Ethylene} = \frac{n_{Ethylene}}{(n_{Ethane}+n_{Ethylene}+(\frac{n_{Methane}}{2})} \times 100} \quad \textbf{(3)}$$

Coke deposits produced during dehydrogenation catalysis were analyzed using Temperature Programed Oxidation (TPO). Used catalyst (100mg) was loaded into a quartz tube reactor and held in place with quartz wool. Oxygen (5%) and argon (95%) gas was flowed at 100mL min^{-1} as the temperature was ramped at 10°C min^{-1} to 800°C. The downstream CO_2 concentration was monitored using a Cirrus 2 benchtop quadrupole mass spectrometer (MKS instruments) at the reactor outlet monitoring for m/z = 32, 40 and 44 signals which were assigned to O_2, Ar and CO_2 respectively.

4.3 Results

X-ray diffraction (XRD) of the as synthesized materials shows two primary broad diffraction peaks with small narrow peaks which correspond to GaOOH impurities (Figure 38). The broad peaks are a possible match for nanocrystalline *P1* or *C2/m* structured Ga_2O_3. Both crystal structures have diffraction peaks clustered around the two broad peaks seen in our experimental results. The broadness of the peaks suggest nanocrystalline particles under 4nm.

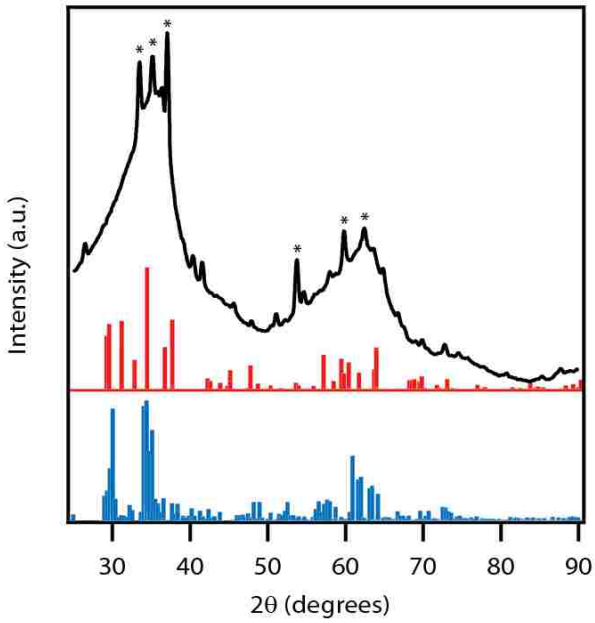

Figure 38: *X-ray diffraction pattern of as-synthesized gallium oxide nanoparticles. Broad peaks are indicative of small crystallite sizes. X-ray diffraction pattern for Ga_2O_3 in the C2/m crystal structure is shown in red (index: mp-886) and the P1 crystal structure shown in blue (index: mp-685090). Primary peaks matching GaOOH impurities (COD entry: 810-0299) are marked by a star (*).*

Figure 39a-c show the HAADF-STEM micrographs and size distribution of the as synthesized gallium oxide nanocrystals. STEM images confirm the presence of sub 4 nm crystallites. Due to the complexity and number of different Ga_2O_3 crystalline polymorphs, lattice spacing and angles derived from the fast Fourier Transform (FFT, inset Figure 39)

could not be tied to one particular structure[139,148]. Crystallites have a rather narrow size distribution of 2.7 ± 0.5 nm measure from surface-equivalent spherical diameter (Figure 39c).

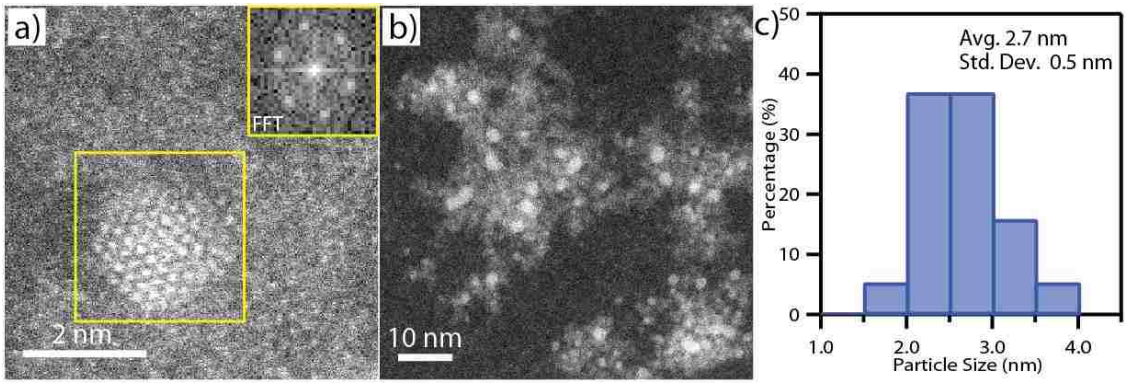

Figure 39: *(a,b) Representative HAADF-STEM images of as synthesized gallium oxide nanoparticles. Crystalline particles are shown mixed with a matrix of amorphous material. The inset FFT in a) is obtained from the area in the yellow box. Crystallite size distributions are shown in (c).*

The effect of the support material on catalysis was investigated in the dehydrogenation of ethane to ethylene. Conversion over time was measured to investigate the deactivation of the catalyst. Figure 40a show the conversion over time for TiO_2 supported gallium (5%) and Al_2O_3 supported gallium (5%). The results show that although the TiO_2 sample has higher conversion initially, after 48 hours the TiO_2 supported catalyst deactivates significantly and the Al_2O_3 supported catalyst retains higher conversion. Temperature Programed Oxidation (TPO) was conducted on Al_2O_3 and TiO_2 supported catalyst to determine the extent of coking (Figure 40b). Outlet CO_2 concentration was monitored as temperature was increases 10°C min^{-1} in flowing O_2 (5%) and Ar (95%) stream. TiO_2 supported gallium show contained 2.0% $^{m}/_{m}$ coke after 48 hours of reaction, 4 times higher

carbon content than gallium supported by Al_2O_3, at 0.5% $^{m}/_{m}$ coke. TiO_2 supported sample showed a lower temperature for carbon burnoff. Figure 41 shows a TPO plot of, bare Al_2O_3, Al_2O_3 supported gallium oxide bulk particles (Alfa Aesar), and Al_2O_3 supported gallium oxide nanocrystals. Both bare Al_2O_3 and Al_2O_3 supported gallium oxide bulk particles show less than 0.1% $^{m}/_{m}$ coke deposits, due to the fact that these materials are largely non-catalytic. These materials showed little catalytic activity with conversions of 0.2% and 0.6% respectively.

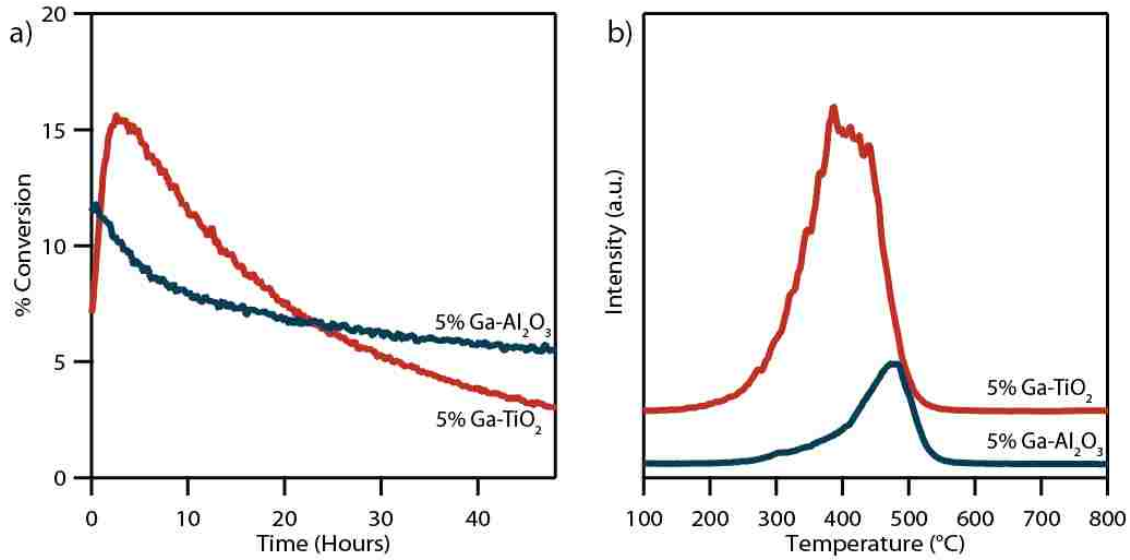

Figure 40: *(a) Conversion over time for 5%Ga/Al_2O_3 and 5%Ga/TiO_2 catalysts. Initially conversion for TiO_2 supported gallium is higher however it drops over 48 hours. Conversion for Al_2O_3 supported gallium is steadier particularly after the first 10 hours. (b) Temperature Programed Oxidation (TPO) plot showing CO_2 evolution with temperature of 48 hour aged samples.*

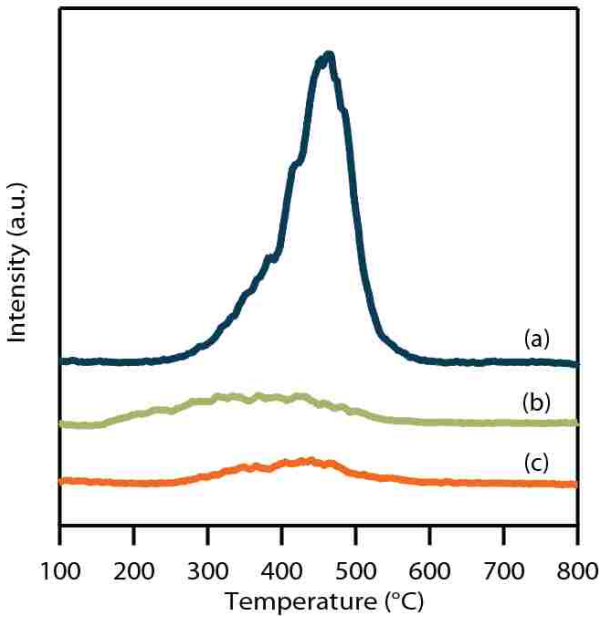

Figure 41: *Temperature Programed Oxidation (TPO) plot showing CO_2 evolution from 48 hour aged (a) Al_2O_3 supported gallium oxide nanocrystals, (b) Al_2O_3 supported Alfa Aesar gallium oxide particles (-325 mesh particles) and (c) bare Al_2O_3.*

Introducing platinum to the catalyst greatly increases the maximum conversion of ethane to ethylene. Conversion over time for 1%Pt-1%Ga(np)/Al_2O_3 catalyst samples reaches a conversion of 26% and maintains a conversion of 11% over a 48 hour period (Figure 42a). In contrast 1% platinum on alumina (1%Pt/Al_2O_3) and 1% platinum and 1% bulk gallium oxide on alumina only reach 17% and 19% conversion and they significantly lose catalytic activity over a 48 hour period reaching 2% and 3% conversion respectively. This reduction in conversion is due to accumulation of coke. The catalyst sample with only 1% gallium oxide nanocrystals on alumina lacks the high initial catalytic activity of platinum containing samples however the sample has significantly less coke accumulation, seen in Figure 42b. This sample has a lower maximum conversion of 10% however the conversion is more consistent with a final conversion of 6% after 48 hours. A summary of the characteristics of the catalyst samples used in this chapter is shown in Table 3.

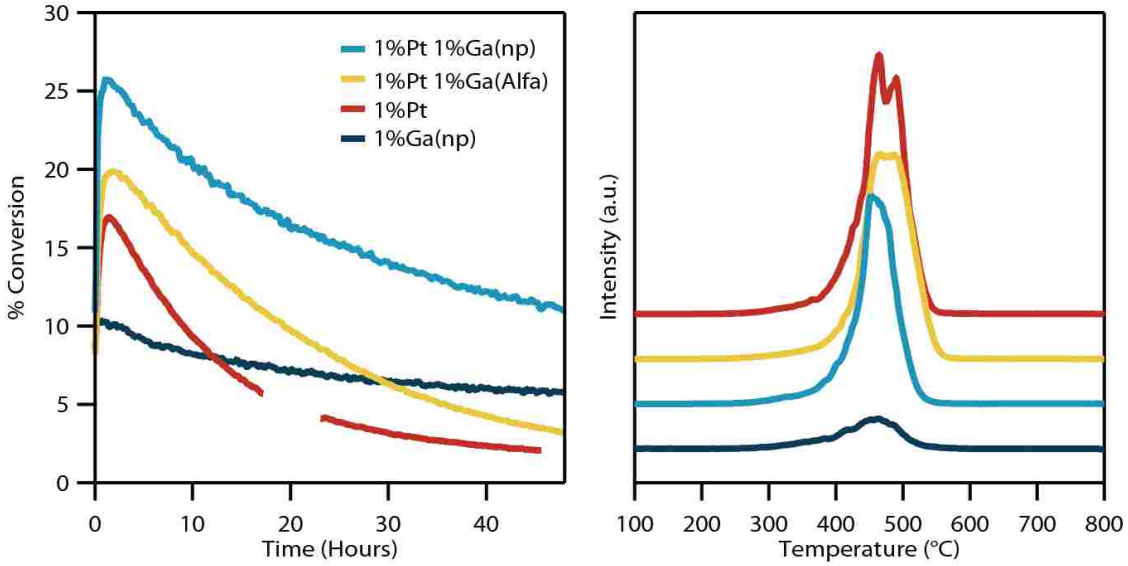

Figure 42: *(a) Conversion over time for 1%Pt-1%Ga(np)/Al_2O_3, 1%Pt-1%Ga(Alfa)/Al_2O_3, 1%Pt/Al_2O_3, and 1%Ga(np)/Al_2O_3. Platinum containing sample have the highest conversion initially however samples containing no gallium oxide or bulk gallium oxide see a significant drop in conversion to less than the conversion of 1%Ga(np)/Al_2O_3. (b) Temperature Programed Oxidation (TPO) plot showing CO_2 evolution with temperature of 48 hour aged samples. Platinum containing samples show significantly higher carbon content than the 1%Ga(np)/Al_2O_3 sample.*

Table 3: Catalytic characteristics of the various platinum and gallium oxide materials supported on Al_2O_3.

Sample	Max Conversion (%)	Conversion (48hr)	Selectivity (%)	Coke Mass[a]
Al_2O_3	0.2	0.2	100	0.1%
1%Ga(Alfa)/Al_2O_3	0.6	0.6	100	0.1%
1%Ga(np)/Al_2O_3	10.2	5.8	98.8	0.4%
1%Pt/Al_2O_3	17	2.1	97.2	2.5%
1%Pt-1%Ga(Alfa)/Al_2O_3	19.90	3.2	98.0	2.4%
1%Pt-1%Ga(np)/Al_2O_3	25.80	11	99.4	1.9%

[a] Measured after 48 hours.

4.4 Discussion

Previous studies of the dehydrogenation of alkanes to olefins over gallium oxide catalyst have suggested a strong relationship between support material and catalytic properties. Titanium oxide and aluminum oxide have been shown to have promoting effects on the

catalytic activity when compared to silicon oxide and magnesium oxide[144]. To maximize the promoting effect of the gallium-support interactions gallium oxide nanocrystals have been produced. In this work gallium oxide is formed in an ambient temperature synthesis method which produces 2.7 nm crystallites.

Our results demonstrate that the synthesis method used by Curran et al. for producing cerium oxide can be modified to produce gallium oxide nanocrystals[147]. High angle annular dark field scanning electron microscopy (Figure 39) shows that this method produces crystalline nanocrystals of about 2.7 nm, however micrographs also show amorphous gallium material that has been produced. Uncertainty in lattice spacing and angle measurements increases as crystal size decreases due to a reduction in the number of lattice planes. This high level of uncertainty in our 2.7 nm crystals along with the number and complexity of the gallium oxide polymorphs, makes crystal structure determination difficult, using transmission electron micrographs. Similarly, powder x-ray diffraction shows broad peaks in the expected positions for both *P1* and *C2/m* crystal structured gallium oxide, Figure 38. Because of the broad diffraction peaks and the number of polymorphs of gallium oxide, it is difficult to confirm one single crystal structure.

Evidence of support interactions is seen in ethane dehydrogenation experiments on TiO_2 and Al_2O_3 supports in this work and in the work of others[144,149,150]. In our experiments, gallium oxide nanoparticles supported on TiO_2 show higher initial conversion when compared to the Al_2O_3 sample however the conversion of the TiO_2 sample goes from 16% at its maximum to 3% after 48 hours, a decrease of 81%. The alumina supported catalyst

has a lower maximum conversion of 12% however it only decreases to 5.5% after 48 hours. From TPO plots we can see that the TiO_2 sample accumulates significantly more coke during the 48 hour period. This coke accumulation is the reason for the severe catalyst deactivation. The TPO oxidation experiment also shows that TiO_2 supported gallium burns off coke at a lower temperature than Al_2O_3 supported gallium. This is a likely explanation for the improved conversion seen by Nakagawa et al. when TiO_2 supported gallium oxide is used with increasing partial pressures of CO_2 as a mild oxidant[149].

Significant increases in catalytic performance have been seen in dehydrogenation catalyst after the addition of platinum[142,151,152]. Platinum aids in C-H activation along with H_2 desorption[152]. Our results show platinum addition increases initial conversion of the catalyst, however significant decreases in conversion are seen over a 48 hour period. In 1%Pt/Al_2O_3 and 1%Pt-1%Ga(Alfa)/Al_2O_3 samples coke build up significantly deactivates the catalyst leading to 88 and 85% decreases in conversion respectively. Bulk gallium oxide particles have a slight effect in reducing the deactivation but our gallium oxide nanocrystals have a larger impact due to their higher surface area and interaction with the support. The 1%Pt-1%Ga(np)/Al_2O_3 sample only sees a reduction of 57% after a 48 hour period demonstrating and the ability of gallium oxide to prevent deactivation in this system. It can be seen that the effect of nanocrystals of gallium oxide and platinum are not independent but they are complementary to each other.

Comparing the amount of coke generated during these 48 hour reaction experiments, we can see that there is little difference in the amount of coke in the 1%Pt/Al_2O_3 and 1%Pt-

1%Ga(Alfa)/Al_2O_3 samples, likely due to the reduced Ga_2O_3-Al_2O_3 interaction. However, we can see clear reduction in coke build up in the 1%Pt-1%Ga(np)/Al_2O_3 sample even when reactivity is higher, likely due to the high level of interaction due to the small crystal size of our synthesized nanocrystals.

4.5 Conclusions

The low temperature ligand mediated synthesis method described can be used to produce 2.7 nm gallium oxide nanocrystals. These gallium oxide crystals when used with an Al_2O_3 support show activity towards the ethane dehydrogenation reaction and show reduced deactivation due to coke when compared to a TiO_2 supported catalyst. Reaction with platinum and gallium oxide nanocrystals supported on alumina reached 26% and maintained 11% conversion after 48 hours (at 500°C and WHSV = 0.5 h^{-1}). Our results show the complementary effect of gallium oxide nanoparticles on alumina when utilized in platinum dehydrogenation system. This effect is due to the ability of gallium oxide on alumina to limit coke build-up. These results give insight into the support interactions in gallium oxide dehydrogenation catalysts and may lead to new developments in dehydrogenation systems.

5. Conclusion

The work presented in this dissertation describes biologically inspired methods for the production of transition metal oxide materials with catalytic properties. The natural mineralization methods are conducted in benign aqueous solution at low temperatures, this gives the materials that are produced many favorable properties. Low temperature synthesis methods allow for the synthesis of crystalline particles that are among the smallest ever produced. This is because particle sintering and growth becomes more prevalent as temperatures increase. Particularly in cerium oxide, particle size effects are strongly linked to catalytic performance due to oxygen vacancy increases in small particles particularly in the sub 5 nm.

Chapter 2 of this dissertation demonstrates how silicatein, the silica producing enzyme in sea sponges, can be used in the production of cerium oxide, zirconium oxide, and a mixed cerium-zirconium oxide. Ceria catalysts produced with enzymatic synthesis were shown to have higher CO oxidation activity, and with zirconium doped ceria enhanced reducibility and enhanced thermal stability further increases catalytic activity. These catalysts were shown to have competitive catalytic performance as compared to similar materials produced with a more conventional method. Additionally the ability to produce smaller particles allow for the fine tuning of the band gap of the material by quantum confinement for optical applications. Above all, our synthesis method has demonstrated that a biomineralized material produced in an environmentally friendly, low temperature, aqueous solution can be used as a functional catalyst.

Chapter 3 of this dissertation discusses another novel method for the synthesis of ceria based nanoparticles. This synthesis method utilizes a ligand assisted base precipitation for the formation of sub 4nm pure ceria and coper-ceria solid solutions. Lactic acid binds with the metal precursors with an intermediate strength, due to the formation of bidentate bonds, allowing for the direct formation of metal oxide. This synthesis method could easily be implemented in a small chemistry lab or scaled for industrial production and used only low cost, readily available precursors in aqueous solvent. Copper doping can be achieved up to 35% with particle size averaging 1.7nm. Catalytic performance of our synthesized particles in the CO oxidation and WGS reaction is competitive with similar materials described in literature.

Chapter 4 discusses how the low temperature ligand mediated synthesis method described can be used to produce 2.7 nm gallium oxide nanocrystals and how these crystals can be incorporated into an ethane dehydrogenation catalyst system. These gallium oxide crystals when used with an Al_2O_3 support show activity towards the ethane dehydrogenation reaction and show reduced deactivation due to coke when compared to a TiO_2 supported catalyst. Reaction with platinum and gallium oxide nanocrystals supported on alumina reached 26% and maintained 11% conversion after 48 hours (at 500°C and WHSV = 0.5 h^{-1}). Our results show the complementary effect of gallium oxide nanoparticles on alumina when utilized in platinum dehydrogenation system. This effect is due to the ability of gallium oxide on alumina to limit coke build-up. The results of this chapter give insight into the support interactions in gallium oxide dehydrogenation catalysts and may lead to new developments in dehydrogenation systems.

6. References

1. Yao, H. C.; Yao, Y. Y. Ceria in automotive exhaust catalysts: I. Oxygen storage. *Journal of Catalysis* **1984**, *86*, 254-265.

2. McIntosh, S.; Gorte, R. J. Direct hydrocarbon solid oxide fuel cells. *Chemical Reviews* **2004**, *104*, 4845-4866.

3. Celardo, I.; Pedersen, J. Z.; Traversa, E.; Ghibelli, L. Pharmacological potential of cerium oxide nanoparticles. *Nanoscale* **2011**, *3*, 1411-1420.

4. Krishnan, M.; Nalaskowski, J. W.; Cook, L. M. Chemical mechanical planarization: slurry chemistry, materials, and mechanisms. *Chemical Reviews* **2009**, *110*, 178-204.

5. Zhou, K.; Wang, X.; Sun, X.; Peng, Q.; Li, Y. Enhanced catalytic activity of ceria nanorods from well-defined reactive crystal planes. *Journal of Catalysis* **2005**, *229*, 206-212.

6. Sun, C.; Li, H.; Chen, L. Nanostructured ceria-based materials: synthesis, properties, and applications. *Energy & Environmental Science* **2012**, *5*, 8475-8505.

7. Si, R.; Flytzani-Stephanopoulos, M. Shape and Crystal-Plane Effects of Nanoscale Ceria on the Activity of Au-CeO2 Catalysts for the Water–Gas Shift Reaction. *Angewandte Chemie* **2008**, *120*, 2926-2929.

8. Newsome, D. S. The water-gas shift reaction. *Catalysis Reviews Science and Engineering* **1980**, *21*, 275-318.

9. Schumacher, N.; Boisen, A.; Dahl, S.; Gokhale, A. A.; Kandoi, S.; Grabow, L. C.; Dumesic, J. A.; Mavrikakis, M.; Chorkendorff, I. Trends in low-temperature water–gas shift reactivity on transition metals. *Journal of Catalysis* **2005**, *229*, 265-275.

10. Li, Y.; Fu, Q.; Flytzani-Stephanopoulos, M. Low-temperature water-gas shift reaction over Cu-and Ni-loaded cerium oxide catalysts. *Applied Catalysis B: Environmental* **2000**, *27*, 179-191.

11. Mamontov, E.; Egami, T.; Brezny, R.; Koranne, M.; Tyagi, S. Lattice defects and oxygen storage capacity of nanocrystalline ceria and ceria-zirconia. *The Journal of Physical Chemistry B* **2000**, *104*, 11110-11116.

12. Bunluesin, T.; Gorte, R. J.; Graham, G. W. CO oxidation for the characterization of reducibility in oxygen storage components of three-way automotive catalysts. *Applied Catalysis B: Environmental* **1997**, *14*, 105-115.

13. Wang, W.; Du, P.; Zou, S.; He, H.; Wang, R.; Jin, Z.; Shi, S.; Huang, Y.; Si, R.; Song, Q. Highly dispersed copper oxide clusters as active species in copper-ceria catalyst for preferential oxidation of carbon monoxide. *ACS Catalysis* **2015**, *5*, 2088-2099.

14. Elias, J. S.; Artrith, N.; Bugnet, M.; Giordano, L.; Botton, G. A.; Kolpak, A. M.; Shao-Horn, Y. Elucidating the nature of the active phase in copper/ceria catalysts for CO oxidation. *ACS Catalysis* **2016**, *6*, 1675-1679.

15. Gamarra, D.; Belver, C.; Fernández-García, M.; Martínez-Arias, A. Selective CO oxidation in excess H_2 over copper− ceria catalysts: identification of active entities/species. *Journal of the American Chemical Society* **2007**, *129*, 12064-12065.

16. Gamarra, D.; Munuera, G.; Hungría, A. B.; Fernández-García, M.; Conesa, J. C.; Midgley, P. A.; Wang, X. Q.; Hanson, J. C.; Rodríguez, J. A.; Martínez-Arias, A. Structure− activity relationship in nanostructured copper− ceria-based preferential CO oxidation catalysts. *Journal of Physical Chemistry C* **2007**, *111*, 11026-11038.

17. Liu, W.; Flytzani-Stephanopoulos, M. Transition metal-promoted oxidation catalysis by fluorite oxides: A study of CO oxidation over Cu-CeO_2. *The Chemical Engineering Journal and the Biochemical Engineering Journal* **1996**, *64*, 283-294.

18. Wang, X.; Rodriguez, J. A.; Hanson, J. C.; Gamarra, D.; Martnez-Arias, A.; Fernndez-Garca, M. Unusual physical and chemical properties of Cu in $Ce_{1-x}Cu_xO_2$ oxides. *Journal of Physical Chemistry B* **2005**, *109*, 19595-19603.

19. Stark, W. J.; Mädler, L.; Maciejewski, M.; Pratsinis, S. E.; Baiker, A. Flame synthesis of nanocrystalline ceria–zirconia: effect of carrier liquid. *Chemical Communications* **2003**, *5*, 588-589.

20. Escribano, V. S.; López, E. F.; Panizza, M.; Resini, C.; Amores, J. M. G.; Busca, G. Characterization of cubic ceria–zirconia powders by X-ray diffraction and vibrational and electronic spectroscopy. *Solid State Sciences* **2003**, *5*, 1369-1376.

21. Lee, J.; Choi, S. Crystallization behavior of nano-ceria powders by hydrothermal synthesis using a mixture of H_2O_2 and NH_4OH. *Materials Letters* **2004**, *58*, 390-393.

22. Migani, A.; Vayssilov, G. N.; Bromley, S. T.; Illas, F.; Neyman, K. M. Greatly facilitated oxygen vacancy formation in ceria nanocrystallites. *Chemical Communications* **2010**, *46*, 5936-5938.

23. Carrettin, S.; Concepcin, P.; Corma, A.; Lpez Nieto, J. M.; Puntes, V. F. Nanocrystalline CeO_2 increases the activity of Au for CO oxidation by two orders of magnitude. *Angewandte Chemie International Edition* **2004**, *43*, 2538-2540.

24. Okuda, M.; Suzumoto, Y.; Yamashita, I. Bioinspired synthesis of homogenous cerium oxide nanoparticles and two-or three-dimensional nanoparticle arrays using protein supramolecules. *Crystal Growth & Design* **2011**, *11*, 2540-2545.

25. Livage, J.; Henry, M.; Sanchez, C. Sol-gel chemistry of transition metal oxides. *Progress in Solid State Chemistry* **1988**, *18*, 259-341.

26. Golden, T. D.; Wang, A. Q. Anodic electrodeposition of cerium oxide thin films II. Mechanism studies. *Journal of the Electrochemical Society* **2003**, *150*, C624.

27. Murdock, D. J.; Donoghue, P. C. Evolutionary origins of animal skeletal biomineralization. *Cells Tissues Organs* **2011**, *194*, 98-102.

28. Porter, S. The rise of predators. *Geology* **2011**, *39*, 607-608.

29. Gal, A.; Weiner, S.; Addadi, L. A perspective on underlying crystal growth mechanisms in biomineralization: solution mediated growth versus nanosphere particle accretion. *CrystEngComm* **2015**, *17*, 2606-2615.

30. Scherrer, P. Bestimmung der Größe und der inneren Struktur von Kolloidteilchen mittels Röntgenstrahlen. *Nachrichten Von Der Gesellschaft Der Wissenschaften Zu Göttingen, Mathematisch-Physikalische Klasse* **1912**, *2*, 98-100.

31. McBride, J. R.; Hass, K. C.; Poindexter, B. D.; Weber, W. H. Raman and x-ray studies of $Ce_{1-x}RE_xO_{2-y}$, where RE= La, Pr, Nd, Eu, Gd, and Tb. *Journal of Applied Physics* **1994**, *76*, 2435-2441.

32. Gleiter, H. H. Gleiter, Prog. Mater. Sci. 33, 223 (1989). *Prog.Mater.Sci.* **1989**, *33*, 223.

33. Deshpande, S.; Patil, S.; Kuchibhatla, S. V.; Seal, S. Size dependency variation in lattice parameter and valency states in nanocrystalline cerium oxide. *Applied Physics Letters* **2005**, *87*, 133113.

34. Shannon, R. D. Revised effective ionic radii and systematic studies of interatomic distances in halides and chalcogenides. *Acta Crystallographica Section A: Crystal Physics, Diffraction, Theoretical and General Crystallography* **1976**, *32*, 751-767.

35. Jasinski, P.; Suzuki, T.; Anderson, H. U. Nanocrystalline undoped ceria oxygen sensor. *Sensors and Actuators B: Chemical* **2003**, *95*, 73-77.

36. Wang, X.; Rodriguez, J. A.; Hanson, J. C.; Gamarra, D.; Martínez-Arias, A.; Fernández-García, M. In situ studies of the active sites for the water gas shift reaction over Cu− CeO_2 catalysts: complex interaction between metallic copper and oxygen vacancies of ceria. *The Journal of Physical Chemistry B* **2006**, *110*, 428-434.

37. Guzman, J.; Carrettin, S.; Corma, A. Spectroscopic evidence for the supply of reactive oxygen during CO oxidation catalyzed by gold supported on nanocrystalline CeO_2. *Journal of the American Chemical Society* **2005**, *127*, 3286-3287.

38. Shindell, D. T.; Faluvegi, G.; Koch, D. M.; Schmidt, G. A.; Unger, N.; Bauer, S. E. Improved attribution of climate forcing to emissions. *Science* **2009**, *326*, 716-718.

39. Myers, P. S.; Uyehara, O. A.; Newhall, H. K. Engine exhaust emissions. In *Engine Emissions*Springer: 1973; pp 1-31.

40. Heuer, A. H.; Fink, D. J.; Laraia, V. J.; Arias, J. L.; Calvert, P. D.; Kendall, K.; Messing, G. L.; Blackwell, J.; Rieke, P. C.; Thompson, D. H. Innovative materials processing strategies: a biomimetic approach. *Science* **1992**, *255*, 1098-1105.

41. Nudelman, F.; Sommerdijk, N. A. Biomineralization as an inspiration for materials chemistry. *Angewandte Chemie International Edition* **2012**, *51*, 6582-6596.

42. Addadi, L.; Raz, S.; Weiner, S. Taking advantage of disorder: amorphous calcium carbonate and its roles in biomineralization. *Advanced Materials* **2003**, *15*, 959-970.

43. St Pierre, T. G.; Mann, S.; Webb, J.; Dickson, D.; Runham, N. W. In *In Iron oxide biomineralization in the radula teeth of the limpet Patella vulgata; Mossbauer spectroscopy and high resolution transmission electron microscopy studies;* Proc. R. Soc. Lond. B; The Royal Society: 1986; Vol. 228, pp 31-42.

44. Cha, J. N.; Shimizu, K.; Zhou, Y.; Christiansen, S. C.; Chmelka, B. F.; Stucky, G. D.; Morse, D. E. Silicatein filaments and subunits from a marine sponge direct the polymerization of silica and silicones in vitro. *Proceedings of the National Academy of Sciences* **1999**, *96*, 361-365.

45. Mann, S. *Biomineralization: principles and concepts in bioinorganic materials chemistry;* Oxford University Press on Demand: 2001; Vol. 5.

46. Spoerke, E. D.; Voigt, J. A. Influence of engineered peptides cadmium sulfide nanocrystals. *Advanced Functional Materials* **2007**, *17*, 2031-2037.

47. Rosant, C.; Avalle, B.; Larcher, D.; Dupont, L.; Friboulet, A.; Tarascon, J. Biosynthesis of Co 3 O 4 electrode materials by peptide and phage engineering: comprehension and future. *Energy & Environmental Science* **2012**, *5*, 9936-9943.

48. Dunleavy, R.; Lu, L.; Kiely, C. J.; McIntosh, S.; Berger, B. W. Single-enzyme biomineralization of cadmium sulfide nanocrystals with controlled optical properties. *Proceedings of the National Academy of Sciences* **2016**, *113*, 5275-5280.

49. Shimizu, K.; Cha, J.; Stucky, G. D.; Morse, D. E. Silicatein α: cathepsin L-like protein in sponge biosilica. *Proceedings of the National Academy of Sciences* **1998**, *95*, 6234-6238.

50. Brutchey, R. L.; Morse, D. E. Silicatein and the translation of its molecular mechanism of biosilicification into low temperature nanomaterial synthesis. *Chemical Reviews* **2008**, *108*, 4915-4934.

51. Andre, R.; Tahir, M. N.; Natalio, F.; Tremel, W. Bioinspired synthesis of multifunctional inorganic and bio-organic hybrid materials. *The FEBS Journal* **2012**, *279*, 1737-1749.

52. Sumerel, J. L.; Yang, W.; Kisailus, D.; Weaver, J. C.; Choi, J. H.; Morse, D. E. Biocatalytically templated synthesis of titanium dioxide. *Chemistry of Materials* **2003**, *15*, 4804-4809.

53. Kisailus, D.; Choi, J. H.; Weaver, J. C.; Yang, W.; Morse, D. E. Enzymatic synthesis and nanostructural control of gallium oxide at low temperature. *Advanced Materials* **2005**, *17*, 314-318.

54. André, R.; Tahir, M. N.; Schröder, H. C. C.; Müller, W. E.; Tremel, W. Enzymatic synthesis and surface deposition of tin dioxide using silicatein-α. *Chemistry of Materials* **2011**, *23*, 5358-5365.

55. Brutchey, R. L.; Yoo, E. S.; Morse, D. E. Biocatalytic synthesis of a nanostructured and crystalline bimetallic perovskite-like barium oxofluorotitanate at low temperature. *Journal of the American Chemical Society* **2006**, *128*, 10288-10294.

56. André, R.; Tahir, M. N.; Link, T.; Jochum, F. D.; Kolb, U.; Theato, P.; Berger, R.; Wiens, M.; Schröder, H.; Müller, W. E. Chemical Mimicry: Hierarchical 1D TiO2@ ZrO2 Core− Shell Structures Reminiscent of Sponge Spicules by the Synergistic Effect of Silicatein-α and Silintaphin-1. *Langmuir* **2011**, *27*, 5464-5471.

57. Tahir, M. N.; Théato, P.; Müller, W. E.; Schröder, H. C.; Borejko, A.; Faiß, S.; Janshoff, A.; Huth, J.; Tremel, W. Formation of layered titania and zirconia catalysed by surface-bound silicatein. *Chemical Communications* **2005**, 5533-5535.

58. Tahir, M. N.; Eberhardt, M.; Therese, H. A.; Kolb, U.; Theato, P.; Müller, W. E.; Schröder, H.; Tremel, W. From Single Molecules to Nanoscopically Structured Functional Materials: Au Nanocrystal Growth on TiO2 Nanowires Controlled by Surface-Bound Silicatein. *Angewandte Chemie International Edition* **2006**, *45*, 4803-4809.

59. Bawazer, L. A.; Izumi, M.; Kolodin, D.; Neilson, J. R.; Schwenzer, B.; Morse, D. E. Evolutionary selection of enzymatically synthesized semiconductors from biomimetic mineralization vesicles. *Proceedings of the National Academy of Sciences* **2012**, *109*, E1714.

60. Spangler, L. C.; Lu, L.; Kiely, C. J.; Berger, B. W.; McIntosh, S. Biomineralization of PbS and PbS–CdS core–shell nanocrystals and their application in quantum dot sensitized solar cells. *Journal of Materials Chemistry A* **2016**, *4*, 6107-6115.

61. Bharde, A.; Rautaray, D.; Bansal, V.; Ahmad, A.; Sarkar, I.; Yusuf, S. M.; Sanyal, M.; Sastry, M. Extracellular biosynthesis of magnetite using fungi. *Small* **2006**, *2*, 135-141.

62. Bansal, V.; Poddar, P.; Ahmad, A.; Sastry, M. Room-temperature biosynthesis of ferroelectric barium titanate nanoparticles. *Journal of the American Chemical Society* **2006**, *128*, 11958-11963.

63. Li, Q.; Liu, D.; Jia, Z.; Csetenyi, L.; Gadd, G. M. Fungal biomineralization of manganese as a novel source of electrochemical materials. *Current Biology* **2016**, *26*, 950-955.

64. Miot, J.; Recham, N.; Larcher, D.; Guyot, F.; Brest, J.; Tarascon, J. Biomineralized α-Fe 2 O 3: texture and electrochemical reaction with Li. *Energy & Environmental Science* **2014**, *7*, 451-460.

65. Larson, A. C.; Von Dreele, R. B. General Structure Analysis System (GSAS). *Los Alamos National Laboratory Report LAUR 86-748* **2000**, 86-748.

66. Yu, T.; Lim, B.; Xia, Y. Aqueous-phase synthesis of single-crystal ceria nanosheets. *Angewandte Chemie International Edition* **2010**, *49*, 4484-4487.

67. Depner, S. W.; Kort, K. R.; Jaye, C.; Fischer, D. A.; Banerjee, S. Nonhydrolytic Synthesis and Electronic Structure of Ligand-Capped CeO2− δ and CeOCl Nanocrystals. *The Journal of Physical Chemistry C* **2009**, *113*, 14126-14134.

68. Yao, M. H.; Baird, R. J.; Kunz, F. W.; Hoost, T. E. An XRD and TEM investigation of the structure of alumina-supported ceria–zirconia. *Journal of Catalysis* **1997**, *166*, 67-74.

69. Hori, C. E.; Permana, H.; Ng, K. S.; Brenner, A.; More, K.; Rahmoeller, K. M.; Belton, D. Thermal stability of oxygen storage properties in a mixed CeO2-ZrO2 system. *Applied Catalysis B: Environmental* **1998**, *16*, 105-117.

70. Zhang, H. T.; Wu, G.; Chen, X. H. Thermal stability and photoluminescence of Zr1− xCexO2 (0≤ x≤ 1) nanoparticles synthesized in a non-aqueous process. *Materials Chemistry and Physics* **2007**, *101*, 415-422.

71. Duwez, P.; Odell, F. Phase relationships in the system zirconia—ceria. *Journal of the American Ceramic Society* **1950**, *33*, 274-283.

72. Hirano, M.; Miwa, T.; Inagaki, M. Low-Temperature Direct Synthesis of Nanoparticles of Fluorite-Type Ceria–Zirconia Solid Solutions by "Forced Cohydrolysis" at 100° C. *Journal of Solid State Chemistry* **2001**, *158*, 112-117.

73. Armirotti, A.; Damonte, G.; Pozzolini, M.; Mussino, F.; Cerrano, C.; Salis, A.; Benatti, U.; Giovine, M. Primary structure and post-translational modifications of silicatein beta from the marine sponge Petrosia ficiformis (Poiret, 1789). *Journal of Proteome Research* **2009**, *8*, 3995-4004.

74. Guillou, N.; Auffredic, J. P.; Louër, M.; Louër, D. The Crystal Structure of Hydronium Cerium (III) Nitrate Hydrate, Ce (NO3) 5 (H3O) 2· H2O. *Journal of Solid State Chemistry* **1993**, *106*, 295-300.

75. Demars, T. J.; Bera, M. K.; Seifert, S.; Antonio, M. R.; Ellis, R. J. Revisiting the solution structure of ceric ammonium nitrate. *Angewandte Chemie* **2015**, *127*, 7644-7648.

76. Zhou, Y.; Shimizu, K.; Cha, J. N.; Stucky, G. D.; Morse, D. E. Efficient catalysis of polysiloxane synthesis by silicatein α requires specific hydroxy and imidazole functionalities. *Angewandte Chemie International Edition* **1999**, *38*, 779-782.

77. Wang, Z. L.; Feng, X. Polyhedral shapes of CeO2 nanoparticles. *The Journal of Physical Chemistry B* **2003**, *107*, 13563-13566.

78. Reddy, B. M.; Bharali, P.; Thrimurthulu, G.; Saikia, P.; Katta, L.; Park, S. Catalytic efficiency of ceria–zirconia and ceria–hafnia nanocomposite oxides for soot oxidation. *Catalysis Letters* **2008**, *123*, 327-333.

79. Katta, L.; Sudarsanam, P.; Thrimurthulu, G.; Reddy, B. M. Doped nanosized ceria solid solutions for low temperature soot oxidation: Zirconium versus lanthanum promoters. *Applied Catalysis B: Environmental* **2010**, *101*, 101-108.

80. Luo, M.; Yan, Z.; Jin, L.; He, M. Raman Spectroscopic Study on the Structure in the Surface and the Bulk Shell of Ce x Pr1-x O2-δ Mixed Oxides. *The Journal of Physical Chemistry B* **2006**, *110*, 13068-13071.

81. Burroughs, P.; Hamnett, A.; Orchard, A. F.; Thornton, G. Satellite structure in the X-ray photoelectron spectra of some binary and mixed oxides of lanthanum and cerium. *Journal of the Chemical Society, Dalton Transactions* **1976**, 1686-1698.

82. Patsalas, P.; Logothetidis, S.; Sygellou, L.; Kennou, S. Structure-dependent electronic properties of nanocrystalline cerium oxide films. *Physical Review B* **2003**, *68*, 035104.

83. Yang, Z.; Wei, Y.; Fu, Z.; Lu, Z.; Hermansson, K. Facilitated vacancy formation at Zr-doped ceria (1 1 1) surfaces. *Surface Science* **2008**, *602*, 1199-1206.

84. Yang, Z.; Woo, T. K.; Hermansson, K. Effects of Zr doping on stoichiometric and reduced ceria: A first-principles study. *The Journal of Chemical Physics* **2006**, *124*, 224704.

85. Zhang, F.; Wang, P.; Koberstein, J.; Khalid, S.; Chan, S. Cerium oxidation state in ceria nanoparticles studied with X-ray photoelectron spectroscopy and absorption near edge spectroscopy. *Surface Science* **2004**, *563*, 74-82.

86. Tsunekawa, S.; Ishikawa, K.; Li, Z.; Kawazoe, Y.; Kasuya, A. Origin of anomalous lattice expansion in oxide nanoparticles. *Physical Review Letters* **2000**, *85*, 3440.

87. Zhang, C.; Grass, M. E.; McDaniel, A. H.; DeCaluwe, S. C.; El Gabaly, F.; Liu, Z.; McCarty, K. F.; Farrow, R. L.; Linne, M. A.; Hussain, Z. Measuring fundamental properties in operating solid oxide electrochemical cells by using in situ X-ray photoelectron spectroscopy. *Nature Materials* **2010**, *9*, 944.

88. Tsunekawa, S.; Fukuda, T.; Kasuya, A. Blue shift in ultraviolet absorption spectra of monodisperse CeO 2− x nanoparticles. *Journal of Applied Physics* **2000**, *87*, 1318-1321.

89. Nahory, R. E.; Pollack, M. A.; Johnston Jr, W. D.; Barns, R. L. Band gap versus composition and demonstration of Vegard's law for In1− x Ga x As y P1− y lattice matched to InP. *Applied Physics Letters* **1978**, *33*, 659-661.

90. French, R. H.; Glass, S. J.; Ohuchi, F. S.; Xu, Y.; Ching, W. Y. Experimental and theoretical determination of the electronic structure and optical properties of three phases of ZrO 2. *Physical Review B* **1994**, *49*, 5133.

91. Castleton, C.; Kullgren, J.; Hermansson, K. Tuning LDA U for electron localization and structure at oxygen vacancies in ceria. *The Journal of Chemical Physics* **2007**, *127*, 244704.

92. Nolan, M.; Parker, S. C.; Watson, G. W. The electronic structure of oxygen vacancy defects at the low index surfaces of ceria. *Surface Science* **2005**, *595*, 223-232.

93. Kwon, H. J.; Cha, M.; Kim, D.; Kim, D. K.; Soh, M.; Shin, K.; Hyeon, T.; Mook-Jung, I. Mitochondria-targeting ceria nanoparticles as antioxidants for Alzheimer's disease. *ACS Nano* **2016**, *10*, 2860-2870.

94. Coutinho, C. A.; Mudhivarthi, S. R.; Kumar, A.; Gupta, V. K. Novel ceria–polymer microcomposites for chemical mechanical polishing. *Applied Surface Science* **2008**, *255*, 3090-3096.

95. Studier, F. W. Protein production by auto-induction in high-density shaking cultures. *Protein Expression and Purification* **2005**, *41*, 207-234.

96. Porath, J. Immobilized metal ion affinity chromatography. *Protein Expression and Purification* **1992**, *3*, 263-281.

97. Patil, S.; Sandberg, A.; Heckert, E.; Self, W.; Seal, S. Protein adsorption and cellular uptake of cerium oxide nanoparticles as a function of zeta potential. *Biomaterials* **2007**, *28*, 4600-4607.

98. Toby, B. H. EXPGUI, a graphical user interface for GSAS. *Journal of Applied Crystallography* **2001**, *34*, 210-213.

99. Mullins, D. R.; Overbury, S. H.; Huntley, D. R. Electron spectroscopy of single crystal and polycrystalline cerium oxide surfaces. *Surface Science* **1998**, *409*, 307-319.

100. Cordeiro, M. A.; Weng, W.; Stroppa, D. G.; Kiely, C. J.; Leite, E. R. High resolution electron microscopy study of nanocubes and polyhedral nanocrystals of cerium (IV) oxide. *Chemistry of Materials* **2013**, *25*, 2028-2034.

101. Cliff, G.; Lorimer, G. The quantitative analysis of thin specimens. *Journal of Microscopy* **1975**, *103*, 203-207.

102. Tauc, J.; Grigorovici, R.; Vancu, A. Optical properties and electronic structure of amorphous germanium. *Physica Status Solidi (B)* **1966**, *15*, 627-637.

103. Polshettiwar, V.; Varma, R. S. Green chemistry by nano-catalysis. *Green Chemistry* **2010**, *12*, 743-754.

104. Centi, G.; Ciambelli, P.; Perathoner, S.; Russo, P. Environmental catalysis: trends and outlook. *Catalysis Today* **2002**, *75*, 3-15.

105. Cargnello, M.; Doan-Nguyen, V. V.; Gordon, T. R.; Diaz, R. E.; Stach, E. A.; Gorte, R. J.; Fornasiero, P.; Murray, C. B. Control of metal nanocrystal size reveals metal-support interface role for ceria catalysts. *Science* **2013**, *341*, 771-773.

106. Scire, S.; Minico, S.; Crisafulli, C.; Satriano, C.; Pistone, A. Catalytic combustion of volatile organic compounds on gold/cerium oxide catalysts. *Applied Catalysis B: Environmental* **2003**, *40*, 43-49.

107. Golunski, S.; Rajaram, R.; Hodge, N.; Hutchings, G. J.; Kiely, C. J. Low-temperature redox activity in co-precipitated catalysts: a comparison between gold and platinum-group metals. *Catalysis Today* **2002**, *72*, 107-113.

108. Trovarelli, A. Catalytic properties of ceria and CeO2-containing materials. *Catalysis Reviews* **1996**, *38*, 439-520.

109. Liu, W.; Flytzani-Stephanopoulos, M. Total oxidation of carbon-monoxide and methane over transition metal fluorite oxide composite catalysts: II. Catalyst characterization and reaction-kinetics. *Journal of Catalysis* **1995**, *153*, 317-332.

110. Yakowitz, H. Methods of quantitative X-ray analysis used in electron probe microanalysis and scanning electron microscopy. In *Practical Scanning Electron Microscopy*Springer: U.S.A., 1975; pp 327-372.

111. Laachir, A.; Perrichon, V.; Badri, A.; Lamotte, J.; Catherine, E.; Lavalley, J. C.; El Fallah, J.; Hilaire, L.; Le Normand, F.; Qumr, E. Reduction of CeO_2 by hydrogen. Magnetic susceptibility and Fourier-transform infrared, ultraviolet and X-ray photoelectron spectroscopy measurements. *Journal of the Chemical Society, Faraday Transactions* **1991**, *87*, 1601-1609.

112. Romeo, M.; Bak, K.; El Fallah, J.; Le Normand, F.; Hilaire, L. XPS study of the reduction of cerium dioxide. *Surface and Interface Analysis* **1993**, *20*, 508-512.

113. Larachi, F.; Pierre, J.; Adnot, A.; Bernis, A. Ce 3d XPS study of composite $Ce_xMn_{1-x}O_{2-y}$ wet oxidation catalysts. *Applied Surface Science* **2002**, *195*, 236-250.

114. Martell, A. E.; Sillen, L. G. *Stability Constants Supplement No.1 ;* The Chemical Society: London, 1971; .

115. Hidmi, L.; Edwards, M. Role of temperature and pH in $Cu(OH)_2$ solubility. *Environmental Science & Technology* **1999**, *33*, 2607-2610.

116. Reed, S. Characteristic fluorescence corrections in electron-probe microanalysis. *British Journal of Applied Physics* **1965**, *16*, 913.

117. Shan, W.; Shen, W.; Li, C. Structural characteristics and redox behaviors of Ce_{1-x} Cu_x O_y solid solutions. *Chemistry of Materials* **2003**, *15*, 4761-4767.

118. Hočevar, S.; Krašovec, U. O.; Orel, B.; Arico, A. S.; Kim, H. CWO of phenol on two differently prepared $CuO–CeO_2$ catalysts. *Applied Catalysis B: Environmental* **2000**, *28*, 113-125.

119. Jobbgy, M.; Marino, F.; Schnbrod, B.; Baronetti, G.; Laborde, M. Synthesis of copper-promoted CeO_2 catalysts. *Chemistry of Materials* **2006**, *18*, 1945-1950.

120. Pemartin-Biernath, K.; Vela-Gonzlez, A. V.; Moreno-Trejo, M. B.; Leyva-Porras, C.; Castaeda-Reyna, I. E.; Jurez-Ramrez, I.; Solans, C.; Snchez-Domnguez, M. Synthesis of mixed Cu/Ce oxide nanoparticles by the oil-in-water microemulsion reaction method. *Materials* **2016**, *9*, 480.

121. Andreeva, D.; Ivanov, I.; Ilieva, L.; Abrashev, M. V.; Zanella, R.; Sobczak, J. W.; Lisowski, W.; Kantcheva, M.; Avdeev, G.; Petrov, K. Gold catalysts supported on ceria doped by rare earth metals for water gas shift reaction: Influence of the preparation method. *Applied Catalysis A: General* **2009**, *357*, 159-169.

122. Yue, L.; Zhang, X. Structural characterization and photocatalytic behaviors of doped CeO_2 nanoparticles. *Journal of Alloys and Compounds* **2009**, *475*, 702-705.

123. Aranda, A.; Ayln, E.; Solsona, B.; Murillo, R.; Mastral, A. M.; Sellick, D. R.; Agouram, S.; Garca, T.; Taylor, S. H. High activity mesoporous copper doped cerium oxide catalysts for the total oxidation of polyaromatic hydrocarbon pollutants. *Chemical Communications* **2012**, *48*, 4704-4706.

124. Jadhav, L. D.; Chourashiya, M. G.; Jamale, A. P.; Chavan, A. U.; Patil, S. P. Synthesis and characterization of nano-crystalline $Ce_{1-x}Gd_xO_{2-x/2}$ (x= 0–0.30) solid solutions. *Journal of Alloys and Compounds* **2010**, *506*, 739-744.

125. Gouadec, G.; Colomban, P. Raman spectroscopy of nanomaterials: how spectra relate to disorder, particle size and mechanical properties. *Progress in Crystal Growth and Characterization of Materials* **2007**, *53*, 1-56.

126. Poulston, S.; Parlett, P. M.; Stone, P.; Bowker, M. Surface oxidation and reduction of CuO and Cu_2O studied using XPS and XAES. *Surface and Interface Analysis* **1996**, *24*, 811-820.

127. Monte, M.; Munuera, G.; Costa, D.; Conesa, J. C.; Martnez-Arias, A. Near-ambient XPS characterization of interfacial copper species in ceria-supported copper catalysts. *Physical Chemistry Chemical Physics* **2015**, *17*, 29995-30004.

128. Holzwarth, U.; Gibson, N. The Scherrer equation versus the 'Debye-Scherrer equation'. *Nature Nanotechnology* **2011**, *6*, 534.

129. Scire, S.; Crisafulli, C.; Riccobene, P. M.; Patan, G.; Pistone, A. Selective oxidation of CO in H_2-rich stream over Au/CeO_2 and Cu/CeO_2 catalysts: an insight on the effect of preparation method and catalyst pretreatment. *Applied Catalysis A: General* **2012**, *417*, 66-75.

130. Freund, H.; Meijer, G.; Scheffler, M.; Schlögl, R.; Wolf, M. CO oxidation as a prototypical reaction for heterogeneous processes. *Angewandte Chemie International Edition* **2011**, *50*, 10064-10094.

131. Royer, S.; Duprez, D. Catalytic oxidation of carbon monoxide over transition metal oxides. *ChemCatChem* **2011**, *3*, 24-65.

132. Saw, E. T.; Oemar, U.; Tan, X. R.; Du, Y.; Borgna, A.; Hidajat, K.; Kawi, S. Bimetallic Ni–Cu catalyst supported on CeO_2 for high-temperature water–gas shift

reaction: methane suppression via enhanced CO adsorption. *Journal of Catalysis* **2014**, *314*, 32-46.

133. Wang, F.; Büchel, R.; Savitsky, A.; Zalibera, M.; Widmann, D.; Pratsinis, S. E.; Lubitz, W.; Schüth, F. In situ EPR study of the redox properties of $CuO–CeO_2$ catalysts for preferential CO oxidation (PROX). *ACS Catalysis* **2016**, *6*, 3520-3530.

134. Cavani, F.; Ballarini, N.; Cericola, A. Oxidative dehydrogenation of ethane and propane: How far from commercial implementation? *Catalysis Today* **2007**, *127*, 113-131.

135. Cavani, F.; Trifiro, F. The oxidative dehydrogenation of ethane and propane as an alternative way for the production of light olefins. *Catalysis Today* **1995**, *24*, 307-313.

136. Kung, H. H. Oxidative dehydrogenation of light (C2 to C4) alkanes. In *Advances in Catalysis*Elsevier: 1994; Vol. 40, pp 1-38.

137. Vajda, S.; Pellin, M. J.; Greeley, J. P.; Marshall, C. L.; Curtiss, L. A.; Ballentine, G. A.; Elam, J. W.; Catillon-Mucherie, S.; Redfern, P. C.; Mehmood, F. Subnanometre platinum clusters as highly active and selective catalysts for the oxidative dehydrogenation of propane. *Nature Materials* **2009**, *8*, 213.

138. Sattler, J. J.; Ruiz-Martinez, J.; Santillan-Jimenez, E.; Weckhuysen, B. M. Catalytic dehydrogenation of light alkanes on metals and metal oxides. *Chemical Reviews* **2014**, *114*, 10613-10653.

139. Zheng, B.; Hua, W.; Yue, Y.; Gao, Z. Dehydrogenation of propane to propene over different polymorphs of gallium oxide. *Journal of Catalysis* **2005**, *232*, 143-151.

140. Meriaudeau, P.; Naccache, C. Dehydrogenation and dehydrocyclization catalytic properties of gallium oxide. *Journal of Molecular Catalysis* **1989**, *50*, L10.

141. Gnep, N. S.; Doyemet, J. Y.; Seco, A. M.; Ribeiro, F. R.; Guisnet, M. Conversion of light alkanes to aromatic hydrocarbons: II. Role of gallium species in propane transformation on GaZSM5 catalysts. *Applied Catalysis* **1988**, *43*, 155-166.

142. Siddiqi, G.; Sun, P.; Galvita, V.; Bell, A. T. Catalyst performance of novel Pt/Mg (Ga)(Al) O catalysts for alkane dehydrogenation. *Journal of Catalysis* **2010**, *274*, 200-206.

143. Sattler, J. J.; Gonzalez-Jimenez, I. D.; Luo, L.; Stears, B. A.; Malek, A.; Barton, D. G.; Kilos, B. A.; Kaminsky, M. P.; Verhoeven, T. W.; Koers, E. J. Platinum-Promoted Ga/Al2O3 as Highly Active, Selective, and Stable Catalyst for the Dehydrogenation of Propane. *Angewandte Chemie International Edition* **2014**, *53*, 9251-9256.

144. Xu, B.; Zheng, B.; Hua, W.; Yue, Y.; Gao, Z. Support effect in dehydrogenation of propane in the presence of CO_2 over supported gallium oxide catalysts. *Journal of Catalysis* **2006**, *239*, 470-477.

145. Michorczyk, P.; Kuśtrowski, P.; Kolak, A.; Zimowska, M. Ordered mesoporous Ga_2O_3 and Ga_2O_3–Al_2O_3 prepared by nanocasting as effective catalysts for propane dehydrogenation in the presence of CO_2. *Catalysis Communications* **2013**, *35*, 95-100.

146. Talati, A.; Haghighi, M.; Rahmani, F. Impregnation vs. coprecipitation dispersion of Cr over TiO 2 and ZrO 2 used as active and stable nanocatalysts in oxidative dehydrogenation of ethane to ethylene by carbon dioxide. *RSC Advances* **2016**, *6*, 44195-44204.

147. Curran, C. D.; Lu, L.; Kiely, C. J.; McIntosh, S. Ambient temperature aqueous synthesis of ultrasmall copper doped ceria nanocrystals for the water gas shift and carbon monoxide oxidation reactions. *Journal of Materials Chemistry A* **2018**, *6*, 244-255.

148. Playford, H. Y.; Hannon, A. C.; Barney, E. R.; Walton, R. I. Structures of uncharacterised polymorphs of gallium oxide from total neutron diffraction. *Chemistry-A European Journal* **2013**, *19*, 2803-2813.

149. Nakagawa, K.; Kajita, C.; Okumura, K.; Ikenaga, N.; Nishitani-Gamo, M.; Ando, T.; Kobayashi, T.; Suzuki, T. Role of carbon dioxide in the dehydrogenation of ethane over gallium-loaded catalysts. *Journal of Catalysis* **2001**, *203*, 87-93.

150. Shao, C.; Lang, W.; Yan, X.; Guo, Y. Catalytic performance of gallium oxide based-catalysts for the propane dehydrogenation reaction: effects of support and loading amount. *RSC Advances* **2017**, *7*, 4710-4723.

151. Galvita, V.; Siddiqi, G.; Sun, P.; Bell, A. T. Ethane dehydrogenation on Pt/Mg (Al) O and PtSn/Mg (Al) O catalysts. *Journal of Catalysis* **2010**, *271*, 209-219.

152. Liu, G.; Zeng, L.; Zhao, Z.; Tian, H.; Wu, T.; Gong, J. Platinum-modified ZnO/Al_2O_3 for propane dehydrogenation: minimized platinum usage and improved catalytic stability. *ACS Catalysis* **2016**, *6*, 2158-2162.

7. Vita

Christopher Curran

www.linkedin.com/in/cdcurran90

CHEMICAL ENGINEER

Offering experience in materials synthesis, and characterization of nanoscale inorganic materials for use in catalysts, electrodes and other high surface area applications. Key competencies include:

- Materials Characterization
- Nanoparticle Synthesis
- Catalyst Design and Testing
- Wet Chemistry
- Biomineralization
- Electron Microscopy

EDUCATION

Lehigh University, Bethlehem, PA — May 2018
Ph.D., Chemical Engineering, GPA: 3.4
Advisors: Dr. Steven McIntosh, Dr. Christopher Kiely, and Dr. Bryan Berger

Drexel University, Philadelphia, PA — 2008-2013
B.S., Chemical Engineering, GPA: 3.3

TECHNICAL SKILLS

- Applications: Electron Microscopy (SEM, TEM, STEM), X-Ray Diffraction (XRD), Heterogeneous catalysis, Fiber Electrospinning, UV Spectroscopy (UV-Vis), FTIR Spectroscopy, BET Surface Area, X-ray Photoelectron Spectroscopy (XPS), Gas Chromatography (GC), Gel Electrophoresis, Protein expression, Plasmid miniprep, E-coli transformation
- Instruments: Hitachi 4300SE SEM, PANAlytical X-ray diffractometer, Zetasizer Nano ZS, Witec Raman spectrometer, Shimadzu UV spectrometer, Shimadzu FTIR spectrophotometer, TA differential scanning calorimeter, SRI 8610C GC, VTI vapor sorption analyzer, shear and rotational rheometers
- Software: MATLAB, Aspen, HYSYS, Maple, PANAlytical HighScore, CasaXPS, Gamry, Shimadzu UVprobe and IRsolutions, EDAX, electronic notebook software, Microsoft Office Suite

RESEARCH EXPERIENCE — 2011-Present

Transition Metal Oxide Nanoparticle Fabrication Projects
Lehigh University

- Worked in a multidisciplinary research group advised by **Dr. Steven McIntosh, Dr. Christopher Kiely**, and **Dr. Bryan Berger**
- Designed chemical and biological synthesis methods for the formation of solid solution transition metal oxides at low temperatures in aqueous solution
- Produced low cost, sub 2nm, catalyst particles in an ambient temperature aqueous environments for a more efficient green catalyst for oxidation reactions
- Characterized and tested catalytic performance of the materials for use in CO oxidation and low temperature water gas shift reactions.

MgOx/Carbon Anode Electrospinning Project
Drexel University

- Worked under the supervision of **Dr. Vibha Kalra** in developing nanofiber materials for lithium-ion batteries
- Performed fabrication, characterization and testing of high surface area fiber anode materials.

SELECTED PUBLICATIONS

- **Curran, C. D**.; Lu, L.; Kiely, C. J.; McIntosh, S. Ambient temperature aqueous synthesis of ultrasmall copper doped ceria nanocrystals for the water gas shift and carbon monoxide oxidation reactions. *Journal of Materials Chemistry A* **2018***, 6*, 244-255.
- **Curran, C. D**.; Lu, L.; Jia, Y.; Kiely, C. J.; Berger, B. W.; McIntosh, S. Direct Single-Enzyme Biomineralization of Catalytically Active Ceria and Ceria–Zirconia Nanocrystals. *ACS Nano* **2017***, 11*, 3337-3346.
- Lu, L.; **Curran, C**.; Kiely, C. J.; Berger, B. W.; Mcintosh, S. Morphology and Composition of Biomineralized Ceria and Ceria-Zirconia Nanocrystals. *Microscopy and Microanalysis* **2016***, 22*, 250.
- Hu, A.; **Curran, C**.; Tran, C.; Kapllani, A.; Kalra, V. Fabrication of transition metal oxide-carbon nanofibers with novel hierarchical architectures. *Journal of Nanoscience and Nanotechnology* **2014***, 14*, 5501-5507.

LEADERSHIP + PRESENTATIONS

- **Green & Sustainable Chemistry Conference** at G&SE meeting, Berlin, Germany May 2018
  Topic: Scalable ambient temperature aqueous synthesis of ultrasmall copper doped ceria nanocrystals for carbon monoxide oxidation and WGS reactions
- **Kenneth A. Earhart Award** Sep 2017
- **ACS Conference Presentation** at ACS spring meeting, San Francisco, CA Apr 2017
  Topic: Biomineralization and bioinspired synthesis of ceria and transition metal-ceria solid solution nanocrystals
- **Seminar Presentation** at Lehigh University, Bethlehem, PA Nov 2016
  Topic: Biomineralization and bioinspired synthesis of transition metal substituted ceria nanocrystals
- **Graduate Student Senate** Chemical Engineering Representative 2013-2015
- **Health Research Hub Safety Representative** 2014-Present